Simulations of Flow Induced Ordering in Viscoelastic Fluids

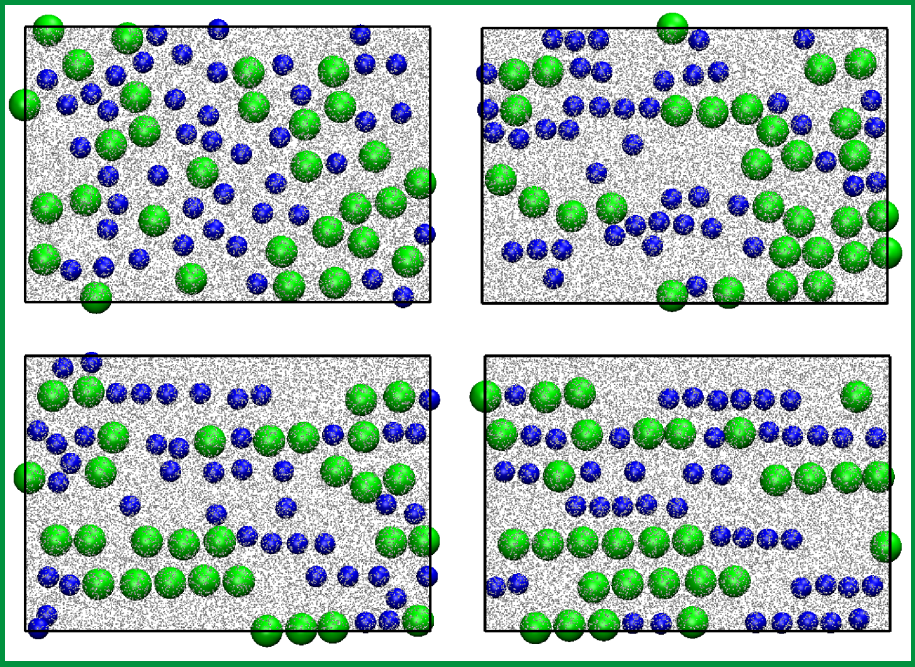

Igor Santos de Oliveira

SIMULATIONS OF FLOW INDUCED ORDERING IN VISCOELASTIC FLUIDS

IGOR SAULO SANTOS DE OLIVEIRA

Promotion committee:

Prof. dr. G. van der Steenhoven	University of Twente (Chairman)
Prof. dr. G. van der Steenhoven	University of Twente (Secretary)
Prof. dr. W. J. Briels	University of Twente (Supervisor)
Dr. W. K. den Otter	University of Twente (Ass. Supervisor)
Prof. dr. B. Geurts	University of Twente
Prof. dr. F. Mugele	University of Twente
Prof. dr. J. Vermant	Katholieke University Leuven, Belgium
Prof. dr. D. Vlassopoulos	University of Crete, Greece
Prof. dr. J. K. G. Dhont	Forschungszentrum Jülich, Germany

Santos de Oliveira, I.S.
Simulations of flow induced ordering in viscoelatic fluids
Ph.D. Thesis, University of Twente, Enschede

ISBN: 978-90-365-3479-6

DOI: 10.3990/1.9789036534796
Online version: http://dx.doi.org/10.3990/1.9789036534796

Typeset in LaTeX by the author

Printed by: Gildeprint Drukkerijen - www.gildeprint.nl

SIMULATIONS OF FLOW INDUCED ORDERING IN VISCOELASTIC FLUIDS

DISSERTATION

to obtain
the degree of doctor at the University of Twente,
on the authority of the rector magnificus,
prof. dr. H. Brinksma,
on account of the decision of the graduation committee,
to be publicly defended
on Friday, 7 December 2012 at 16:45

by

Igor Saulo Santos de Oliveira

born on 5 January 1983
in Monte Alegre de Minas, Brazil

This dissertation has been approved by:

Prof. dr. W. J. Briels (promotor)

and

Dr. W. K. den Otter (assistant promotor)

Contents

1 Introduction

1.1 Self-assembly of nanoparticles

Self-assembly describes the processes in which a disordered system of nanoparticles or other discrete components form an organized structure or pattern as a consequence of local interactions among the components themselves and/or indirectly, through their environment [41]. The process of self-assembly occurs spontaneously once certain conditions are set. Thus, the free energy of final state of the system is lower than the initial state. Only some materials are capable of self-assembling, they must possess specific characteristics (shape, charge, etc.) in order to be viable. Gaining control of the way that particles self-assemble can help in the process of bottom-up nanofabrication. This process can be used to fabricate nanostructured materials, since arranging particles at small scales is technologically very difficult. Therefore, one easier way to create nanodevices is to manipulate the nanoparticles properties in order for them to self assemble into a desired configuration. In this way, it is possible to generate species of the same material which exhibit different properties depending on their spatial location. This is very important in nanotechnology applications, and can also change the material characteristics at the macroscopic level.

The self-assembly of particles can be static or dynamic, the former case refers to systems that evolves to a global or local thermodynamic equilibrium, the latter describes self-assembly in nonequilibrium systems. In dynamic self-assembly the mode and extension of organization can be controlled, depending on the amount of energy delivered to the system. These dynamic structures rely on a constant energy supply for survival, and collapse when the flow of energy ceases. Although these systems have been studied intensively for several decades [35,40,121] they are still poorly understood, mostly because of the lack of general variational principles

governing their behavior. To induce self-assembly the particles can be designed in order to maximize their interactions with external directing fields (magnetic, electric, flow) or using directing surfaces (confined geometries, interfaces).

Templates, defined as surface-modified substrates containing active sites which can induce nanoparticle deposition, are used to self-assemble nanoparticles into complex aggregates with well-controlled sizes, shapes, and internal structures [124]. The interface between liquid-liquid systems can also be explored to create templates for nanoparticle assembly [10], with the lower energy in the interfacial region attracting particles and facilitating their organization. Electric and magnetic fields induced assembly occurs due to polarization of the particles, which can lead to ordered phases from dipole-dipole interactions [55]. In addition viscous flows can be used to direct the assembly of a disordered suspension of particles [119] (see Section 1.3).

1.2 The rheology of suspensions

Rheology can be defined as the science that studies the deformation and flow of matter. It is the study of the manner in which materials respond to applied stress or strain. The first use of the word rheology is credited to Eugene C. Bingham, in 1920 [98], which comes from the Greek words *rheo* (flow) and *logy* (study of). All materials have at some degree rheological properties, and the area is important in many fields of study and industrial areas of activity, including plastic processing, polymers and composites, paints and inks, bioengineering, food, cosmetics, pharmaceutics and pressure sensitive adhesives. Therefore, rheology is a very attractive field of research, with applications in a wide range of activities. In particular, many industrial processes are consisted of particles dispersed in rheologically complex fluids, with such systems refered to as *suspensions*.

In this thesis we will focus on suspensions of colloids. Colloids are particles with size varying from few nanometers to a few microns. They have a large variety of shapes and chemical compositions. In general, colloids are particles too large to be described in terms of their detailed atomic structure, but they are small enough to be subject to thermal fluctuations. Colloidal suspensions are found in many substances used in our daily life, ranging from food products, paint, cosmetics to blood [66]. For quiescent suspensions, a wide range of

colloidal organizations can be encountered, depending on the material characteristics. Their equilibrium phase behavior can be predicted by application of statistical thermodynamics theory [99].

In the case of suspensions subjected to flow, different particle rearrangement may occur, while in the absence of flow no ordering or different structures develop [119]. Flow-induced ordering can be affected by the strength of the applied shear rate, or shear strain, by the particle volume fraction, particle interaction potentials, and polydispersity. In highly dense systems, the volume fraction can be large enough to crystallize. However, structures can also be formed in low concentration suspensions.

Dispersions of colloids will behave differently depending on whether the suspending media is a Newtonian or non-Newtonian liquid. Non-Newtonian fluids present complex rheological behavior as their viscosity or flow behavior changes under stress. Applying a force to such fluids can cause them to get thicker and act as a "solid-like" fluid (shear-thickening fluids), in other cases it results in the opposite behavior and they become "more fluid" (shear-thinning fluids). In particular, viscoelastic fluids exhibit shear-thinning, memory effects and first and second normal stress differences, resulting in an increase of the rheological complexity of the sheared system. Examples of these materials are polymeric or a concentrated surfactant matrix. Viscoelastic stresses anisotropies induced by flow application can be used to induce direct self-assembly of particles dispersed in the media. One example of structures formed in shear-thinning viscoelastic fluids is 1-dimensional string-like chains of spherical particles (see section 1.3.2).

The study of direct self-assembly of particles in complex fluids is a relatively new area of research, and still poorly understood. Since this behavior can be useful in many industrial applications, it is imperative to predict and control the process of structure formation. It is also important from a scientific perspective, to understand the physics behind the ordering phenomenon in non-Newtonian fluids.

In this thesis, we investigate flow-induced alignment of colloids dispersed in shear-thinning viscoelastic fluids by means of coarse-grained computer simulations. The project is part of the European research programme Nanodirect [83], whose objective is to develop a toolbox for directed self-assembly, obtaining formulations with desired properties for either processing or final function of nanoparticle based materials.

1.3 Flow-induced structures in viscoelastic non-Newtonian fluids

Particles dispersed in complex fluids under flow in viscoelastic fluids can lead to different forms of self-organization. The resulting configuration of the system depends on the rheological properties of the liquid and the nature of the suspending particles, as their shapes, sizes and concentration. In this thesis we will focus on spherical colloids at low volume fraction concentration, dispersed in semi-dilute shear-thinning viscoelastic fluids. The particles dispersed in those fluids have been reported to align in the flow direction, forming chains of particles [82, 92]. This is opposite to observations of particles in Newtonian fluids, where the same particles disperse rather than chaining. Viscoelasticity seems to be a necessary condition to observe alignment. However, it is not sufficient to guarantee alignment. An overview of some experimental observations of spherical particles aligning in viscoelastic fluids, under different kinds of flow, is now presented.

1.3.1 Sedimenting particles

The difference in the behavior of particles dispersed in Newtonian and non-Newtonian fluids can be exemplified by observing their sedimentation. The flow-induced interactions in sedimenting particles suspension is determined by the pair interaction between neighboring spheres, which depends on the normal stresses at points of stagnation on the spheres. The interactions between sedimenting spheres can be described as *drafting*, *kissing* and *tumbling* in Newtonian fluids. For a non-Newtonian fluid the mechanism changes to *drafting*, *kissing* and *chaining* [57]. The effect of the different interactions are exemplified with experiments illustrated in Fig. 1.1. Two touching spheres launched side-by-side in a Newtonian fluid will be pushed apart, until it reaches an equilibrium distance, from this point they will fall together without further lateral migration. In a non-Newtonian fluid, two particles initially located side-by-side and separated by a small distance, where they can still interact with each other, will attract and then turn and chain. If the sedimenting particles are close to a wall, the wall-particle interaction will also be different depending on the fluid. In a Newtonian fluid the particle launched close to a wall will move away from the wall to an equilibrium distance where the lateral motion is ceased. On the other hand, in a viscoelastic liquid the particle will

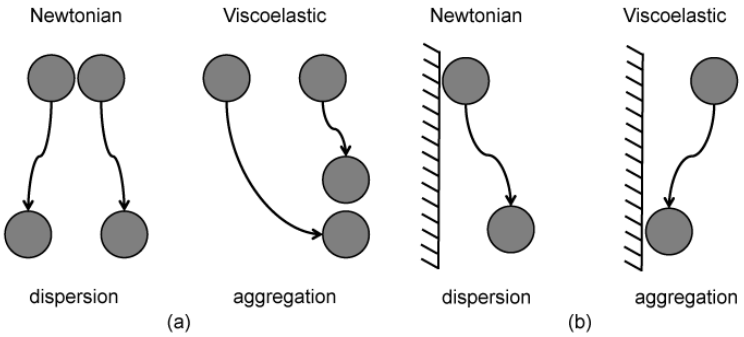

Figure 1.1: Particle sedimenting in a Newtonian and a viscoelastic fluid. (a) Behavior of the particles in the bulk, and (b) close to walls (adapted from [57]).

be attracted by the wall, if its initial location is in the range where wall-sphere interaction is sufficiently large.

1.3.2 Shear flow

Chains of small spherical particles can be created and aligned in the direction of the motion in shear flows. The first reported study of flow induced structures in viscoelastic suspensions of spherical colloids was in 1977 by Michele *et al*. It was observed that for semi-dilute suspensions of spherical particles in a highly viscoelastic media the particles align in planar and elongational flows. In effect they lined up forming long string-like structures oriented in the flow direction. The absence of such structures in Newtonian fluids was also confirmed. In 1978, Giesekus [38] showed that in bidisperse suspension the particles segregate and form separate strings according to their size (see Fig. 1.2).

Many further experiments have been carried out in order to study the conditions necessary to observe chaining of particles. For example, Petit and Noetinger [96] observed alignment and aggregation for oscillatory flow. Lyon *et al.* [72] verified alignment and segregation with monodisperse and bidisperse particle size distributions, for both steady and oscillatory flows, confirming earlier experiments on similar materials. The effect of the suspending fluid on flow-induced alignment of small spherical particles was also investigated by Scirocco *et al.* [103] and Wom and Kim [122]. Both works verified that the alignment was not gov-

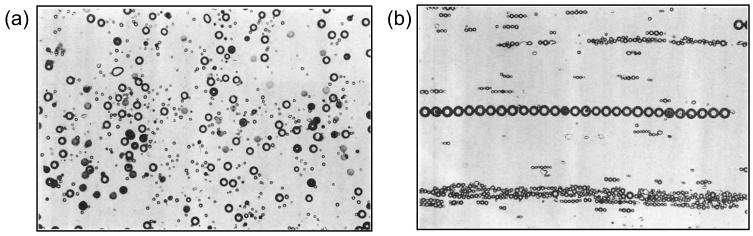

Figure 1.2: Alignment of a size bidisperse suspension in a viscoelastic fluid. (a) Initial configuration and (b) after shear flow equilibration, the flow is applied along the horizontal direction (adapted from [38]).

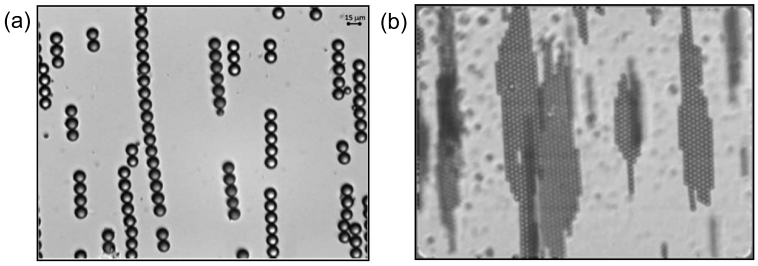

Figure 1.3: Spherical particles dispersed in a wormlike micellar solution. (a) String-like structures formed in the vertical flow direction at a shear rate of 3 s^{-1}. (b) 2D crystal created when the system was sheared at 30 s^{-1} (adapted from [92]).

erned only by the Weissenberg number. Previously Giesekus [38] proposed a critical value for the Weissenberg number above which it becomes possible to observe chains of colloids. More recently, Pasquino *et al.* [92] investigated the flow behavior of particle suspensions in a wormlike micellar viscoelastic solution. They observed in the bulk the formation of string-like structures at low shear rate, and at high shear rate 2D planar crystal structures were formed, as shown in Fig. 1.3. In addition, Pasquino *et al.* [93] verified that in a rather weak shear-thinning and mildly viscoelastic HPC solution, spherical particles migrate toward the walls and alignment was observed close to or at the walls. However, no alignment was observed in the bulk. This indicates that wall effects together with particles migration can help to promote chaining of particles in the system.

Evidently, a number of experiments have been employed to study particle migration and

chaining. However a greater understanding of the emergence or lack of particle structures can be gained through the use of computer simulations, which provides information that may be inaccessible in experiments.

1.4 Computer simulation of nanoparticles

Computer simulations have become a very important tool in the study of scientific problems. Simulations can validate experiments but also predict properties and help to elucidate problems in many fields. The use of computers to solve questions raised by science started after the Second World War due to advances in computation during the war. With the increase of computer power and development of new algorithms, larger and more complex systems can be simulated. In this work we will focus on the simulation of polymeric systems, which are large enough to ignore quantum effects and can be treated using classical approaches. The most used techniques to simulate systems at the molecular level are Molecular Dynamics, Monte Carlo and Brownian Dynamics simulations.

The Molecular Dynamics (MD) method assumes that the movement of the molecules obey Newton's law of motion. The first MD approach was proposed in 1959 by Alder and Wainwright [2]. Given the initial positions and velocities of all particles and their intermolecular interactions potential, the trajectory can be followed by integrating Newton's equation over a small time step. MD simulations are limited to short time-scales, because it demands very small integration time steps in order to keep the system in equilibrium, making its use to simulate long polymer chains or colloids very inefficient for studying these systems under flow. Monte Carlo (MC) simulations are used to obtain thermodynamic properties of a box filled with interacting particles. At each step the particles are displaced by a random small distance, changing the potential energy. This new configuration is accepted if the energy is lower than the previous configuration, otherwise it is accepted or rejected according to the Boltzmann probability. This algorithm is known as the Metropolis method [81], and can be used to compute static properties of large systems. However the algorithm lacks time-dependent informations.

If large time and length-scales are required, as in the simulation of polymer solutions, it is necessary to turn to more coarse-grained models where molecular details are ignored. One

way to simulate a collection of large molecules is to describe the Brownian motion of macromolecules or colloidal particles due to random collisions with the surrounding molecules. This approach is known as Brownian Dynamics (BD) method. The technique takes advantage of the fact that there is a large separation in time scales between the rapid motion of solvent molecules and the slower motion of polymers or colloids. This allows the replacement of explicit solvent particles by stochastic forces which represent the collisions with large particles. In this way, the evolution of the particles in time can be described by a Langevin equation:

$$\frac{d\mathbf{p}_i}{dt} = -\xi_i \mathbf{v}_i + \mathbf{F}_i^c + \mathbf{F}_i^R, \tag{1.1}$$

where $\mathbf{p}_i$ is the momentum of particle i. The first term in the right hand side represents a viscous force acting on the particle, which is proportional to the particle's velocity $\mathbf{v}_i$, and ξ_i is the friction coefficient representing the strength of viscous dissipation. $\mathbf{F}_i^c$ is the conservative force acting on particle i and $\mathbf{F}_i^R$ is the random force caused by the ignored degrees of freedom, which characterizes the Brownian motion in the system. This term has zero mean and variance equal to

$$\langle \mathbf{F}_i^R(t)\mathbf{F}_i^R(0)\rangle = 2kT\xi_i\delta(t), \tag{1.2}$$

where $\delta(t)$ represents a delta function.

The use of the propagator to displace the particles in time takes in consideration that at the Smoluchowski time scale [13], which delimits the region where Brownian motion is important, the momentum $\mathbf{p}_i$ averages to zero. Assuming that, Eq. (1.1) can be rewritten as

$$\frac{d\mathbf{r}_i}{dt} = \frac{1}{\xi_i}\left(\mathbf{F}_i^c + \mathbf{F}_i^R\right), \tag{1.3}$$

where $\mathbf{r}_i$ is the position of particle i. Therefore, knowing the intermolecular interactions, applying random forces to system and defining the friction between particles, it is possible to simulate the dynamics of large particles. Brownian Dynamics simulations are very useful to describe the behavior of polymers under flow.

Techniques using coarse-graining simulations and the fact that a suspended particle undergoes stochastic collisions with the solvent, resulting in Brownian motion, are known as mesoscopic methods. They are used specially to describe complex flows phenomena. Examples of coarse grained approaches are Dissipative Particle Dynamics (DPD) [31, 48, 65],

Multiparticle Collision Dynamics (MPCD) [39, 73, 74], or Lattice Boltzmann (LB) methods [30, 110, 123].

1.5 A polymer chain as a single particle: the RaPiD method

The examples of coarse-graining models cited in the previous section can be used to speed up the simulations and reach time and length scales much longer than for a system with a detailed description of structure. However, in some situations depending on the quantities that are required to become accessible over the simulation time, a even more severe coarse-graining approach is necessary. This fact can be exemplified with a simulation to obtain rheological properties of a polymer melt. Firstly, in order to obtain a melted system it is necessary to have many polymer chains in a reservoir. It is also necessary to observe the system for a long time in order to quantify its response for an applied shear stress. Therefore, at the same time a large number of particles and long simulation runs are required. To fulfill these requirements, our group has developed a coarse-grained method where each polymer chain in the system is represented only by its center of mass position [14, 117]; namely the Responsive Particle Dynamics (RaPiD) method, which is a mesoscopic method based on Brownian Dynamics simulation. The level of coarse-graining is depicted in Fig. 1.4 for a typical simulation system used in this work. The result is a box containing many point particles. If the interactions between the particles are known, the RaPiD method allows the simulation of the system dynamics in time.

Despite the simplification of representing a long polymer chain by a single particle, the main features of this kind of molecule are still recovered in the RaPiD method by the addition of transient forces between particles. The dynamics of long polymer chains in polymer melts and concentrated solutions are slowed down due to entanglements between them. The fact that chains can not cross each other leads to extra complications in the displacement of the chains that are not captured by simple interaction potentials between the particles represented in Fig. 1.4. The effect of entanglements is included in the RaPiD model by adding a set of variables accounting for the number of entanglements between particles, which depend on their separation distance. In this way, every time the particle moves to a new position its

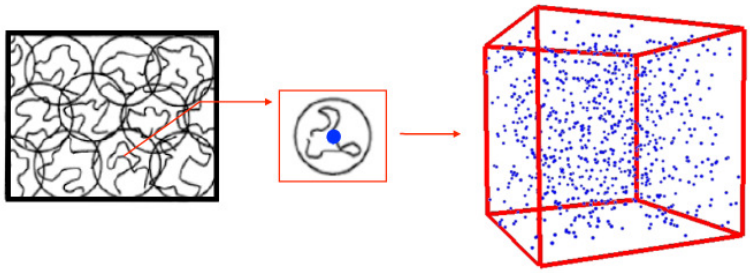

Figure 1.4: Coarse-graining used in the RaPiD method. Each polymer chain showed in the first box is represented by its center of mass position, the blue particle in the middle. Then, many of these punctual particles are added to the simulation box.

number of entanglements with neighboring particles is changed and the system takes some time to reach a configuration with a given equilibrium entanglements number. This method generates memory effects in the system, since at every new configuration it "remembers" earlier stages until the equilibrium is reached.

The RaPiD approach will be discussed in details throughout this work, but a schematic idea on how the method works is depicted in Fig. 1.5. In Fig. 1.5 (a) two particles i and j have been separated by an initial distance r_{ij} for a long time, therefore the number of entanglements is constant (c), and the entanglement force is zero (d). Then at the dashed line ($t_{perturbation}$) the particles are moved to a new separation distance. Since the distance between them is increased, the conservative force F_{cons} decreases (Fig. 1.5 (b)). Figure 1.5 (c) shows the number of entanglements n_{ij} between the particles, which has some value before the perturbation and after the particles displacement, n_{ij} slowly decreases and reaches a new equilibrium value $n_0(r_{ij})$. This perturbation on n_{ij} creates an entanglement force F_{ent}, and it goes again to zero when n_{ij} reaches the new equilibrium value. These transient entanglement forces create the effect of elasticity between particles, which is very important in order to simulate the rheology of complex fluids.

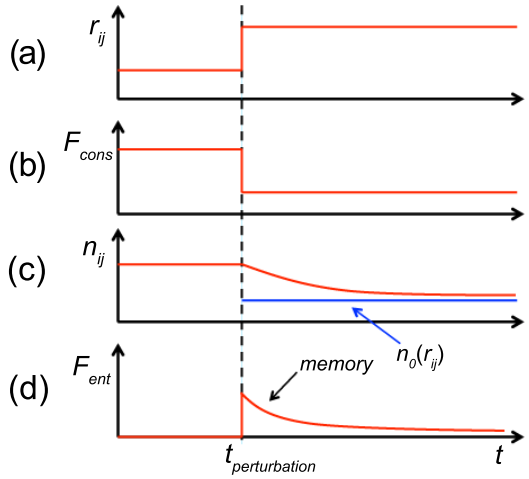

Figure 1.5: Representation of the forces acting in the system when particles in equilibrium are displaced. In (a) the particles are moved to a new separation distance r_{ij} at $t_{pertubation}$, changing the conservative force F_{cons} in (b). A new equilibrium number of entanglements $n_0(r_{ij})$ is obtained to the new position in (c), creating an entanglement force F_{ent} during this process, represented in (d).

1.6 Thesis outline

This thesis describes the use of coarse grained simulations to investigate the flow behavior of spherical colloids dispersed in shear-thinning viscoelastic fluids. The aim is to first simulate the flow-induced alignment of the colloids, using the RaPiD method. The informations obtained from the simulations will help towards understanding the physical mechanisms responsible for this phenomenon. In addition to alignment, size segregation and wall effects are also investigated. The thesis is organized as follows.

In *Chapter 2*, two distinct shear-thinning fluids in the semi-dilute regime are simulated. A free energy equation describing the equilibrium distribution of the particles is developed according to the Flory-Huggins theory. We then show that this potential in addition to transient forces, as demanded in the RaPiD approach, are sufficient to reproduce experimental equilibrium rheological properties of the two model fluids. Applying a shear flow to the systems, the experimental shear-viscosity curves of both fluids are also satisfactorily repro-

duced. From this point, colloids are added to the liquids and their dynamics under shear are investigated.

In *Chapter 3* results from further investigations on colloids dispersed in shear-thinning fluids are presented. These investigations serve to capture and describe the colloids and fluid particles dynamics during the simulations, and to comprehend the conditions and process that drive the colloids to aligned configurations. Analyzing the flow-induced effective colloidal interactions, we investigate the causes of attraction between colloids and relate it to the distribution of liquid particles around the colloids. By systematically varying the parameters used to model the simulated fluids, a method to determine the critical shear rate necessary to observe alignment in the system, depending on the given input parameters, is acquired.

Experiments with monolayer suspensions of colloids bidispersed in size show that when the colloids are observed to align in the sheared system, they will also segregate by size. We then used the simulations carried out in *Chapter 2*, where alignment was observed in the bulk of one of the model fluids used, and extended it to include colloids with two different sizes in *Chapter 4*.

In *Chapter 5* wall effects are investigated. Experimental observations show that colloids dispersed in non-Newtonian fluids migrate towards the system walls, when shear flow is applied. Using the polymer solution simulated in *Chapter 2*, we investigate confinement effects in the distribution of dispersed colloids. The migration process is analyzed by changing shear rate, confinement and colloids size.

The influence of each RaPiD parameter in the description of the linear rheology for complex fluids is investigated in *Chapter 6*. By analyzing stress autocorrelation functions from simulations with many combinations of simulation parameters, and also by tuning the parameters to model a particular shear-thinning viscoelastic fluid, a procedure to parameterize complex fluids with RaPiD simulations is presented.

At the end of this thesis, the results are summarized in both English and Dutch.

2 Alignment of particles in sheared viscoelastic fluids

We investigate the shear-induced structure formation of colloidal particles dissolved in non-Newtonian fluids by means of computer simulations. The two visco-elastic fluids investigated are a semi-dilute polymer solution and a worm-like micellar solution. Both shear-thinning fluids contain long flexible chains whose entanglements appear and disappear continually as a result of Brownian motion and the applied shear flow. To reach sufficiently large time and length scales in three-dimensional simulations with up to 96 spherical colloids, we employ the Responsive Particle Dynamics (RaPiD) simulation method of modeling each chain as a single soft Brownian particle with slowly evolving inter-particle degrees of freedom accounting for the entanglements. Parameters in the model are chosen such that the simulated rheological properties of the fluids, i.e. the storage and loss moduli and the shear viscosities, are in reasonable agreement with experimental values. Spherical colloids dispersed in both quiescent fluids mix homogeneously. Under shear flow, however, the colloids in the micellar solution align to form strings in the flow direction, whereas the colloids in the polymer solution remain randomly distributed. These observations agree with recent experimental studies of colloids in the bulk of these two liquids.

2.1 Introduction

The response of a Newtonian liquid to shear deformation is to develop a stress proportional to the applied shear rate. Non-Newtonian fluids, in contrast, display a variety of more complex stress versus rate-of-strain relationships. For example, they can have elastic properties, have long-lived memories of earlier states, or have an apparent viscosity that depends on how fast you shear them. Such fluids have many practical uses, e.g., as industrial lubricants, as drilling and fracturing fluids that improve oil recovery from oil wells, and as thickeners in the paint and food industry [66]. Non-Newtonian fluids are also important in biology: a well-known non-Newtonian fluid is blood. In this paper we present simulations of shear-thinning liquids, i.e. fluids whose apparent viscosities decrease with increasing shear rate, and study the ordering of dispersed solid particles in these fluids under shear.

Colloidal particles in a sheared visco-elastic fluid are frequently observed to spontaneously form colloidal chains along the flow direction, depending on the fluid's flow characteristics, applied shear rate and boundary conditions, while this behavior is not observed in simple Newtonian fluids. This poorly understood phenomenon was already reported in 1977 by Michele *et al.* [82] and confirmed a decade ago by Lyon *et al.* [72]. In these studies it was suggested that colloidal alignment appears when the Weissenberg number, defined as the ratio of first normal stress difference to shear stress, is larger than 10. Subsequent work by Scirocco *et al.* [103] and Won and Kim [122] showed that this critical Weissenberg number is not universal. These studies also established that viscoelasticity is not a sufficient condition for structure formation, since alignment is not observed in viscoelastic Boger fluids [103, 122]. Instead, these authors suggested that shear-thinning is a necessary condition for shear-induced alignment of spherical particles. The recent work of Pasquino *et al.* [92] on dilute suspensions of hard spheres in a wormlike micellar solution showed the formation of string-like structures at low shear rates and 2D crystals at high shear rates. For a review on flow-induced ordering in complex fluids we refer the reader to Malkin *et al.* [75]. The Vermant group [93] has recently shown that alignment typically occurs at the walls of the rheometer, following colloidal migration from the bulk towards these walls. Worm-like micellar solutions are exceptional by producing alignment in the bulk. Here, our focus will be on (dis)ordering of colloids in bulk viscoelastic fluids.

There is much practical interest in gaining control over the arrangement of particles em-

bedded in fluids. For example, Manski *et al.* [76] suggested that controlled structuring is very useful in food engineering. It is therefore important to gain more insight into the still poorly understood process of colloidal structuring under flow. Here, we show how advances in computer simulation methods offer new possibilities to obtain such insights. The problem of simulating colloids dispersed in viscoelastic fluids has been considered before by a number of groups, using lattice methods and Stokesian approaches to calculate flow fields subject to the boundary conditions posed by the colloids. Feng *et al.* [34], Binous and Phillips [9], Harlen [43], Yu *et al.* [125], and Ardekani *et al.* [4] simulated one and two spheres sedimenting through a viscoelastic fluid. Hwang *et al.* [54] studied kissing and tumbling of two colloids in shear flow and observed strong shear-induced elongational flows between six colloids. Patankar and Hu [94] simulated the migration of a colloid towards the centerline of a channel in a pressure-driven flow. D'Avino *et al.* [20–22] analyzed the rotation of a particle in a sheared viscoelastic liquid, and the shear-induced migration of a particle towards a wall. Flow-induced aggregation of a dozen colloids in a viscoelastic solution was simulated by Yu *et al.* [125] for sedimenting particles and by Phillips and Talini [97] and Hwang and Hulsen [53] for suspensions exposed to a shear flow. We note that these studies have in common that the three-dimensional calculations have been limited to one and two colloidal particles in a viscoelastic fluid, while simulations with up to a dozen colloids were all restricted to two dimensions.

In this chapter, we show that the particle-based off-lattice Responsive Particle Dynamics (RaPiD) method [14, 117] efficiently simulates various visco-elastic fluids, is easily applied to fluids containing many colloids, and thereby makes possible the computational study in three dimensions of colloidal ordering under shear flow. To study the effect of the viscoelastic fluid on the alignment in the bulk, we study three dimensional dispersions of up to 96 spherical colloids in two distinct shear-thinning viscoelastic solutions. One fluid models a solution of polyisobutylene (PIB) dissolved in pristane, with polymers of molecular weight $M_w = 1.2 \cdot 10^3$ kg/mol. The second fluid models a worm-like micellar solution of cetylpyridiniumchloride (CPyCl) and sodiumsalicylate (NaSal) in salt water, at concentrations of 100 mM and 60 mM, respectively. In Section 2.2 we describe how these fluids are simulated using the Responsive Particle Dynamics (RaPiD) method. In Section 2.3 we show that the RaPiD model is able to reproduce the experimental bulk rheological properties of

both fluids [107] reasonably well. Spherical particles are immersed in these fluids in Section 2.4, and the dispersions are next subjected to shear flow to study the resulting ordering, or lack of ordering, of the colloids. The main conclusions are summarized in Section 2.5.

2.2 Simulation method

2.2.1 Background

To reach the large time and length scales required in simulations of colloidal ordering, we will coarse-grain entire polymer chains and worm-like micelles to single particles. Each polymer and micelle is represented by just the position of its center-of-mass. This is not to say that all the removed coordinates are irrelevant for the rheology of the system. On the one hand, the eliminated coordinates provide the free energy function Φ_C, the so-called potential of mean force, which governs the equilibrium distribution of the N_p centers of mass. In thermodynamic equilibrium the probability distribution $P_{\text{eq}}(r)$ of the center-of-mass positions r is given by

$$P_{\text{eq}}(r) \propto \exp\left[-\beta\Phi_C(r)\right], \tag{2.1}$$

where $\beta = 1/kT$ is the inverse of the thermal energy, with Boltzmann's constant k and temperature T. On the other hand, the removed coordinates give rise to friction and random forces in the equations of motion for the retained coordinates [25, 80]. In most coarse-grain representations of soft matter systems, these frictions and random forces necessarily have 'memory' of the configurations the system has gone through in the recent, and sometimes even the distant past [14]. For example, when describing polymeric systems on the level of their centers of mass, as we do here, the friction and random forces must effectively represent all important effects caused by entanglements; a simple Brownian dynamics propagator with realistic mean forces and Markovian random displacements will not reproduce representative paths of the retained coordinates. To circumvent the introduction of memory effects in the friction forces and stochastic displacements, we employ the Responsive Particle Dynamics (RaPiD) method [14, 117].

The idea behind the RaPiD method is to introduce a relatively small set of additional dynamic variables which keep track, in a coarse-grained manner, of the thermodynamic state

of the eliminated coordinates. Deviations of these additional variables from their equilibrium values, with the latter being determined by the configuration r of the retained coordinates, give rise to additional forces acting on the retained coordinates, on top of the thermodynamic forces derived from the potential of mean force. In the RaPiD method these additional non-equilibrium forces are specifically designed with the propensity to resist deformation of the configuration r, by driving the system back to its earlier state, while at the same time these forces slowly fade away as the additional variables relax toward their new equilibrium values for the new configuration. This particular combination of characteristics, i.e. the transient resistance to deformation, endows the simulated fluid with a viscoelastic behavior. In the current study of semi-dilute polymer and worm-like micellar solutions at nearly 15 times the critical overlap concentration, the dominant physical mechanism giving rise to viscoelastic behavior is the entanglement of the chains; the additional transient forces will therefore also be referred to as entanglement forces. The versatility of the RaPiD method is illustrated by successful applications to fluids as diverse as solutions of polymeric core-shell colloids [115], highly entangled polymer melts [63], telechelic polymer networks [109], solutions of star polymers [90], and glue [88], and its ability to simulate flow phenomena ranging from shear thinning [117], shear banding [115] and shear fracture [108] to microscopic phase separation and lamellar re-orientation under shear [64].

2.2.2 Conservative forces

The configurational free energy Φ_C of a semi-dilute solution of polymeric or worm-like micellar chains is conveniently described by the Flory-Huggins (FH) theory [36, 51]. We adapt the FH model here, following Kindt and Briels [63], to calculate the local free energy subject to the given center of mass positions of the chains; this free energy takes into account all possible configurations of the monomers in the chains and of the solvent. It will be assumed that this local free energy can be expressed as a function of the local number density of polymers. During the simulation, the local number density around a specific polymer i is calculated as

$$\rho_i = \sum_{j=1}^{N_p} \omega(r_{ij}), \tag{2.2}$$

where N_p is the number of chains (polymers or worms) in the system and $\omega(r)$ is a suitably normalized weight function. There is no rigorous way to define this weight function, but

some demands should be satisfied. The weight as a function of the distance to the chain's center will be a monotonously decreasing function. The weight function must have a non-zero derivative at the origin, for otherwise the repulsive forces at very short distances do not prevent the formation of clusters. To avoid discontinuities in the force at the cut-off radius r_c, the weight function and its first derivative should go to zero smoothly. We use simple linear and quadratic expressions to satisfy these demands,

$$\omega(r_{ij}) = \begin{cases} c(r_c - r_s)(r_c + r_s - 2r_{ij}) & : \quad r_{ij} \leq r_s \\ c(r_{ij} - r_c)^2 & : \; r_s < r_{ij} \leq r_c \\ 0 & : \; r_c < r_{ij}, \end{cases} \tag{2.3}$$

where r_s denotes the distance where the weight function switches from linear to quadratic, and c is a normalization constant chosen such that $\int \omega(r_{ij}) \mathrm{d}\mathbf{r} = 1$. Because the range of chain-chain interactions is of the order of the chain radius of gyration R_g, we choose $r_c = 2.5R_g$ and $r_s = R_g$. We note that there is no conservation law associated with the local densities ρ_i, i.e. $\langle \rho_i \rangle \neq \rho$ in general, where $\rho = N_p/V$ is the box-averaged number density. Nevertheless, ρ_i provides a reasonable measure for the local polymer number density at the position of polymer i.

The local polymer volume fraction ϕ_i entering the Flory-Huggins free energy expression may now be defined as

$$\phi_i = \frac{\rho_i}{\rho_{\max}}, \tag{2.4}$$

where $\rho_{\max}$ defines the maximum local polymer density, i.e. the density of a solvent-free polymer melt, and therefore $\phi_i \leq 1$. Using the procedure described in Appendix 2.5, we can approximate the total free energy of the system, for a given configuration r, as a sum of particle contributions

$$\Phi_C = \sum_{i=1}^{N_p} a^p(\phi_i), \tag{2.5}$$

where the free energy per chain, as a function of the local chain density, reads as

$$a^p(\phi_i) = pkT \left\{ \frac{1-\phi_i}{\phi_i} \ln(1-\phi_i) - \chi \phi_i \right\}. \tag{2.6}$$

Here p is the number of Kuhn segments in the chain and χ is the usual Flory-Huggins parameter as defined in Eq. (A.5). The resulting thermodynamic forces acting on the particles

are readily derived by differentiating Eq. (2.5)), as is shown in Appendix 2.5. We note that the denominator to the fraction in Eq. (2.6) will never be zero, by virtue of the self-term in Eq. (2.2); besides this, the limit of $a^p(\phi_i)$ when ϕ_i approaches zero is constant.

2.2.3 Transient forces

We now turn our attention to the transient forces, which were already qualitatively introduced at the start of this section. The motion of a chain in a polymer solution (or in a worm-like micellar solution) is slowed down predominantly by entanglements with neighboring chains. The corresponding transient forces are approximately included in the RaPiD method by introducing an additional variable n_{ij} for every close pair of chains i and j. This additional variable will be referred to as the number of entanglements that exist between this pair of chains, but we note that any type of chain intermixing that slows down the dynamics is included. The entanglement force between particles i and j will be assumed linear in the deviation of the entanglement number from the equilibrium number of entanglements $n_0(r_{ij})$ for the given distance between the two particle. The 'entanglement potential' behind the entanglement force is then given by

$$\Phi_t(r,n) = \frac{1}{2}\alpha \sum_{i,j} (n_{ij} - n_0(r_{ij}))^2, \tag{2.7}$$

where α determines the variance of the fluctuations in n_{ij} and the sum runs over all neighboring particle pairs. The equilibrium entanglement number $n_0(r_{ij})$ depends on the probability of having monomers of the two chains in close proximity, i.e. n_0 is proportional to the overlap of two chains. For Gaussian chains, the distribution of monomers around the center of mass of a chain is approximately a Gaussian distribution [26] and the overlap is again an approximately Gaussian function of the separation between the centers of mass [1]. However, to avoid zero forces at short distances, we choose to represent $n_0(r_{ij})$ not by a Gaussian but by a good fitting quadratic function that, furthermore, smoothly vanishes at the cut-off radius:

$$n_0(r_{ij}) = \begin{cases} \left(\dfrac{r_{ij}}{r_c} - 1\right)^2 & : \; r_{ij} \leq r_c \\ \\ 0 & : \; r_{ij} > r_c. \end{cases} \tag{2.8}$$

Because n_{ij} and $n_0(r)$ always appear in combination with α in the entanglement force and potential, we are free to choose a suitable normalisation for n_0, and hence n_{ij}, while retaining α as a fit parameter of the model. We have chosen for $n_0 = 1$ at $r = 0$, and consequently $n_0(r)$ may loosely be interpreted as the *fraction* of maximum overlap.

Given the conservative and entanglement potentials, the equilibrium probability density Ψ to encounter a certain configuration r in combination with a set of entanglement numbers n reads as

$$\Psi(r,n) \propto \exp\{-\beta\left[\Phi_C(r) + \Phi_t(r,n)\right]\}. \tag{2.9}$$

One readily shows that integration over n, exploiting the quadratic structure of Φ_t, recovers the equilibrium probability density of Eq. (2.1). We therefore conclude that the entanglement forces alter the dynamical properties of a fluid but not its thermodynamical properties. This property will be used below to show that variations in the dynamical properties alone suffice to generate markedly different alignment behavior.

2.2.4 Equations of motion

Having defined the potential, the displacement of particle i over a simulation time step dt on the Smoluchowski time scale is given by [14, 117]

$$\mathbf{r}_i = -\frac{1}{\xi_i}\left(\nabla_i\Phi_C + \nabla_i\Phi_t\right)dt + \nabla_i\left(\frac{kT}{\xi_i}\right)dt + \boldsymbol{\Theta}_i\sqrt{\frac{2kT\,dt}{\xi_i}}. \tag{2.10}$$

The first term on the right hand side is the contribution of conservative and entanglement forces, with the particle-dependent friction parameter ξ_i to be discussed below. The middle term corrects for a spurious drift that would otherwise have resulted in a finite time step algorithm from the non-constancy of the friction coefficient. The last term describes Brownian displacements of the particles, where the components of the time-dependent Markovian random vector $\boldsymbol{\Theta}_i$ have unit variance and zero mean, the three Cartesian components are independent and the set of vectors is devoid of inter-particle correlations. Since the friction experienced by a chain is mainly due to entanglements, we assume that the friction coefficient of particle i is proportional to the actual number of entanglements of particle i with its

neighbors,

$$\xi_i = \xi_0 + \xi_e \sum_{j \neq i} \sqrt{n_{ij} n_0(r_{ij})}, \tag{2.11}$$

with ξ_e the friction per entanglement and where ξ_0 is the background friction by the solvent. By taking the geometric average of n_{ij} with the equilibrium number of entanglements $n_0(r_{ij})$, we ensure that the entanglement friction between particles smoothly ceases at the cut-off distance r_c.

The equation of motion for the entanglement number n_{ij}, again on the Smoluchowski time scale, is given by [14, 117]

$$dn_{ij} = \frac{1}{\tau}\left(n_0(r_{ij}) - n_{ij}\right) dt + \Theta_{ij} \sqrt{\frac{2kT\,dt}{\alpha\tau}}. \tag{2.12}$$

In the last term on the right hand side, Θ_{ij} is a time-dependent random Markovian scalar with zero mean, unit average, and without correlation across particle pairs. For interpretation convenience, the friction coefficient slowing down the entanglement dynamics has been expressed here as $\alpha\tau$, where τ denotes the characteristic relaxation time. We expect the collective entanglements between two chains in close proximity to be of a more severely interwoven nature than those between two distant weakly entwined chains, and therefore the former will take longer to relax than the latter. To take this effect into account, we let the relaxation time depend on the distance between the particles,

$$\tau_{ij} = \tau_0 \exp\left(-\frac{r_{ij}}{\lambda}\right), \tag{2.13}$$

where τ_0 is a time constant and λ denotes the decay length of the relaxation time.

All simulations are performed in rectangular boxes of fixed dimensions, using periodic boundary conditions [3]. In a large number of simulations a shear flow is applied along the x-direction, with a velocity gradient $\dot{\gamma}$ in the y-direction, by using Lees-Edwards sliding boundary conditions [3] in combination with a slightly modified equation of motion. Every time step, the instantaneous flow field in the x-direction is determined for a set of planes at equally spaced heights along the y axis, by attributing the displacements of each particle to its two surrounding planes by a lever-rule. This noisy flow field is then smoothed by averaging over the flow field history, at every height, using an exponentially decaying weight function with a decay time $\tau_{\text{flow}} = 10^{-3}$ s, to obtain the fluid velocity function $V(y)$. By rederiving

the equations of motion, with particle i now experiencing a friction relative to the flow field at height y_i, the displacement in Eq. (2.10) acquires the additional term $+V(y_i)\hat{\mathbf{e}}_x dt$. This approach has been applied successfully in earlier RaPiD simulations, see e.g. [86, 109, 116], and proved sufficiently flexible to permit shear banding and shear fracture. We emphasize the absence of walls in these simulations, which consequently faithfully reproduce bulk shear flow.

2.3 Two shear-thinning fluids

2.3.1 Model parameters

The above described RaPiD method was applied to simulate two distinct shear-thinning viscoelastic fluids. As the first fluid, we studied a polymer solution of a high molecular weight polyisobutylene (PIB, $M_w = 1.2 \cdot 10^3$ kg/mol) dissolved in pristane; this mixture, and behavior of colloids dispersed in this fluid, were the subject of recent experiments by Snijkers *et al.* [107]. These experimental data guided the parametrization of the simulation model, as summarized in Table 2.1. The table is divided in the 'set parameters', listing experimentally known quantities, and the 'simulation parameters', the fitting parameters established to reproduce the experimental rheology of the fluid. In particular, we tuned α, ξ_e, τ_0 and λ for agreement with the experimental zero shear viscosity η_0 and the storage and loss moduli $G'(\omega)$ and $G''(\omega)$, which will be discussed in Section 2.3.3.

As the second fluid, we studied a worm-like micellar solution modeled after an experimental mixture of 100 mM cetylpyridiniumchloride (CPyCl) and 60 Mm sodiumsalicylate (NaSal) in salt water. To parameterize the fluid, we took the polymer solution as reference and adjusted only the parameters related to the entanglement forces. That is, we combined the 'set parameters' of the polymer solution with the new values for α, ξ_e, τ_0 and λ listed at the bottom of Table 2.1. Since the two fluids are microscopically very different, it may come at first sight as a surprise that the potential of mean force Φ_C of the polymer solution has been used to represent a worm-like micellar solution. It should be realized, however, that both polymers and worm-like micelles form long and flexible chains, which reduces the effective interaction between their centers of mass of the chains to a very soft repulsive potential. Therefore, the conservative interactions between polymers and micellar worms are quite

Set parameters	
Temperature	$T = 300\,\mathrm{K}$
Radius of gyration	$R_g = 40\,\mathrm{nm}$
Density	$\rho_p = 3.5\,\mathrm{pol}/R_g^3$
Average volume fraction	$\phi = 0.11 \rightarrow \rho_{\max}/\overline{\rho} = 9$
Flory-Huggins parameter	$\chi = 0.5$
Number of monomers	$p = 2700\,\mathrm{mon./polymer}$
Solvent viscosity	$\eta_s = 5 \cdot 10^{-3}\,\mathrm{Pa\,s}$
Solvent friction	$\xi_0 = 2.45 \cdot 10^{-9}\,\mathrm{kg/s}$
Polymer solution simulation parameters	
Cut-off range	$r_c = 2.5 R_g$
Density critical radius	$r_s = 1.0 R_g$
Entanglement number deviation	$\alpha = 10 kT$
Entanglement friction	$\xi_e = 5 \cdot 10^{-9}\,\mathrm{kg/s}$
Max. entanglement relax. time	$\tau_0 = 250\,\mathrm{s}$
Decay length of ent. relax. time	$\lambda = 0.2 R_g$
Wormlike micellar solution simulation parameters	
Cut-off range	$r_c = 2.5 R_g$
Density critical radius	$r_s = 1.0 R_g$
Entanglement number deviation	$\alpha = 0.1 kT$
Entanglement friction	$\xi_e = 7 \cdot 10^{-7}\,\mathrm{kg/s}$
Max. entanglement relax. time	$\tau_0 = 200\,\mathrm{s}$
Decay length of ent. relax. time	$\lambda = \infty$

Table 2.1: The simulation parameters of the polymer solution and the worm-like micellar solution.

similar, and both are relatively unimportant to the flow behavior, which will be dominated by entanglements. Moreover, we are mainly interested in the rheological effects of each fluid, and a clearer comparison will be possible if the equilibrium structures of the two fluids are assumed to be the same.

The transient force parameters of the worm-like solution, like those of the polymer solution discussed before, were tuned such that good agreement is obtained with the experimental zero-shear viscosity η_0 and the storage and loss moduli $G'(\omega)$ and $G''(\omega)$, which will be discussed in Section 2.3.3. The resulting changes, compared to the polymer solution, are a much smaller entanglement strength α and a much larger entanglement friction ξ_e. Also, the entanglement relaxation time τ is now truly constant, i.e. $\tau = \tau_0$ for $\lambda \to \infty$, in agreement with the observation that a well-entangled wormlike micellar solution effectively has a single relaxation time [18, 29, 32, 120].

2.3.2 Structural properties

The simulations with quiescent fluids were carried out for cubic boxes containing 804 particles in a volume $V = 230R_g^3$. To analyze the structural properties of the system, we calculated the radial distribution function $g(r)$ and the structure factors $S(k)$. Looking at Fig. 2.1, we observe the absence of any clear structure in the system, and only a small correlation hole occurs below distances of the order of R_g. The non-zero $g(r)$ for small distances indicates that the particles can approach each other very closely, which reflects the ability of long flexible chains to coalesce their centers of mass without generating any overlap at the monomeric scale. The structure factors $S(k)$, shown in the inset to Fig. 2.1, confirm the absence of structure in the polymer center of mass distribution. These structural results are in agreement with atomistic Monte Carlo simulations of long linear polymers, e.g. polyethylene [79].

Since we used the same conservative potential for both polymer and worm-like micelles solutions, their equilibrium results should be the same. Our results confirmed that they are very similar indeed, and thereby support the comment below Eq. (2.9) that the transient forces do not perturb the equilibrium structure of the systems.

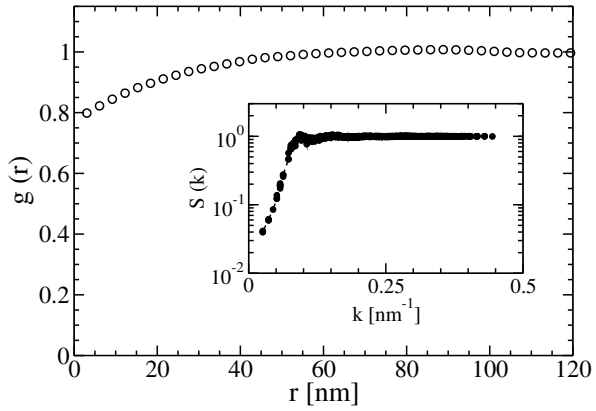

Figure 2.1: Radial distribution function (main plot) and structure factor (inset) for the polymer solution of the centers of mass of polymer chains. The nearly structure-less distribution, with a slight correlation hole below $R_g = 40\,nm$ is typical for the center of mass distribution of long flexible chains. The solution of worm-like micelles yielded identical curves, as it is based in the same conservative interactions.

2.3.3 Dynamic properties

The linear rheology of the model fluids was obtained from equilibrium simulations by computing the autocorrelation of the shear stress. The relevant component of the shear stress tensor is given by

$$S_{xy}(t) = -\frac{1}{V}\sum_{i,j}(r_{i,x} - r_{j,x})F_{ij,y}, \tag{2.14}$$

with $F_{ij,y}$ denoting the y-component of the force on particle i due to conservative and entanglement interactions with particle j. The autocorrelation of the shear stress yields the shear relaxation modulus,

$$G(t) = \frac{V}{kT}\langle S_{xy}(t)S_{xy}(0)\rangle. \tag{2.15}$$

Integration of $G(t)$ from $t = 0$ to ∞ results in the zero-shear viscosity η_0, while the real and imaginary parts of its Fourier transform yield the storage modulus G' and loss modulus G'',

$$G'(\omega) = \omega\int_0^\infty \sin(\omega t)G(t)\mathrm{d}t, \tag{2.16}$$

$$G''(\omega) = \omega\int_0^\infty \cos(\omega t)G(t)\mathrm{d}t, \tag{2.17}$$

respectively.

The shear-thinning behavior of both fluids was analyzed by applying shear flow. From the steady-state shear stresses over a wide range of shear rates, the apparent viscosity was calculated as

$$\eta(\dot{\gamma}) = \frac{S_{xy}(\dot{\gamma})}{\dot{\gamma}}. \tag{2.18}$$

The simulation results are discussed next.

The integral of $G(t)$ of the polymer solution yielded a zero-shear viscosity $\eta_0 = 70\,\mathrm{Pa\,s}$, in close agreement with the experimental value of 75 Pa s [107]. Figure 2.2 shows that the storage and loss moduli agree qualitatively with their experimental counterparts, and match the experimental cross-over angular frequency of 20 rad/s. We did not tune the parameters of the model any further to get better agreement with experiments since our goal in this chapter is to provide a proof of principles only. Moreover the experimental system was polydisperse, asking for much more elaborate simulations. The shear viscosity extracted from simulations under shear, see Fig. 2.3, is fairly constant for low shear rates up to $1\,\mathrm{s}^{-1}$, as is the experimental shear viscosity. At high shear rates the viscosity shows a steady decline – the main characteristic of a shear-thinning fluid – with the viscosity of the model fluid decaying slightly steeper than that of the real fluid. We did not observe shear-banding in the applied range of shear rates.

Equilibrium simulations of the worm-like micellar solution yielded a zero-shear viscosity of 28 Pa s, in excellent agreement with the experimental value of 28 Pa s [107]. The storage and loss moduli, plotted in Fig. 2.4, closely follow their experimental counterparts. The rheological behavior of this system is well captured by a Maxwell model as was also reported by [29, 66], while the polymer solution shows the hallmarks of a fluid with a distribution of relaxation times. Simulations of sheared solutions yielded the shear viscosity curve of Fig. 2.5. The plateau at low shear rates and the rate of decline at high shear rates are in quantitative agreement with experimental data, though the onset of shear-thinning occurs at a slightly lower shear rate in the simulations. Despite a shear-thinning exponent of nearly -1, we did not observe shear-banding for the shear rates used here.

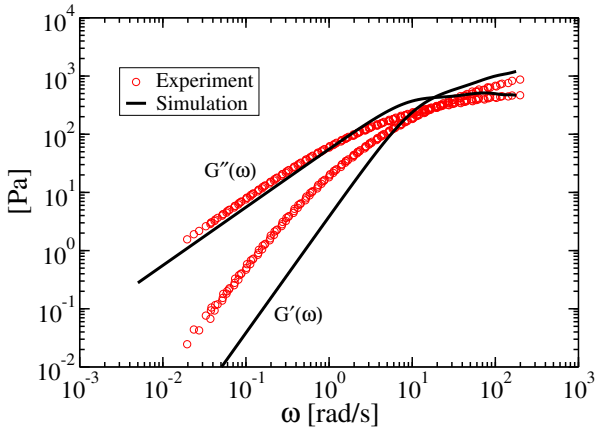

Figure 2.2: Storage modulus $G'(\omega)$ and loss modulus $G''(\omega)$ of the polymer solution over a range of frequencies. The black solid lines are simulation results, obtained as Fourier transforms of $G(t)$, and the red circles denote experimental results by Snijkers et al. [107].

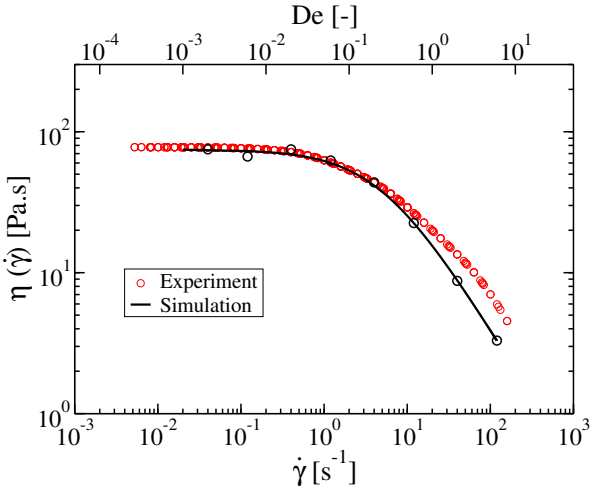

Figure 2.3: The apparent shear viscosity of the polymer solution as a function of applied shear rate, and Deborah number ($De = \dot{\gamma}\tau_{\text{cross}}$), showing in black our simulation results and in red the experimental results by Snijkers et al. [107].

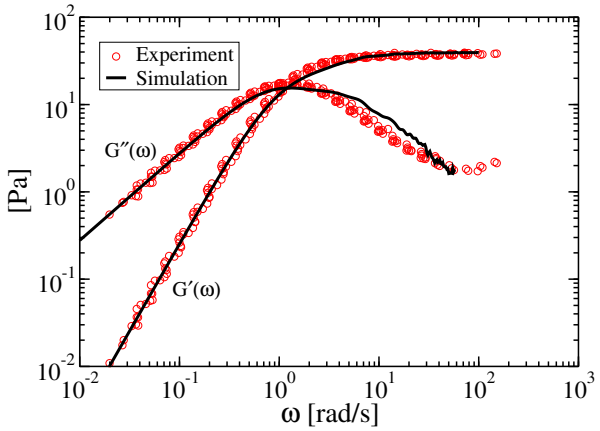

Figure 2.4: Storage modulus $G'(\omega)$ and loss modulus $G''(\omega)$ of the worm-like micellar solution, with the black solid lines showing simulation results and the red circles denoting experimental results by Snijkers et al. [107].

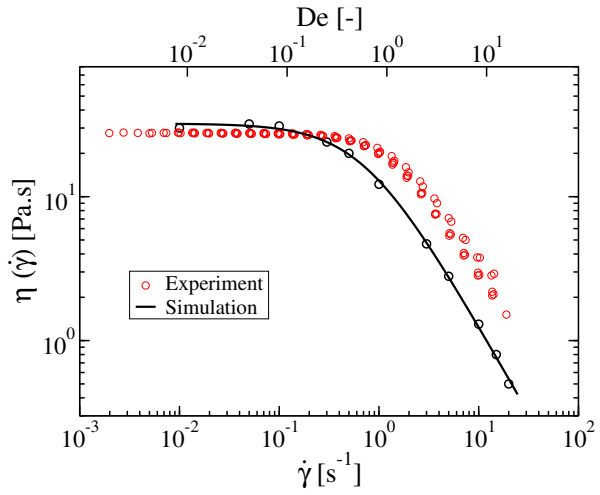

Figure 2.5: Shear viscosity curve and Deborah number for the worm-like micellar solution, showing simulation results (black) and experimental results (red) by Snijkers et al. [107].

2.4 Colloidal dispersions

2.4.1 Spherical colloids

The visco-elastic fluids of the preceeding section were used to suspend spherical colloids, with colloidal radii equal to the radius of gyration of the polymer and micellar chains, $R_{\mathrm{col}} = R_g = 40\,\mathrm{nm}$. These colloids are much smaller than the colloids used in the recent experiments with dispersions in the same fluids by Pasquino *et al.* [92], since the experimental radius would have led to prohibitively large simulation boxes. Because of the smaller size, Brownian displacements play a more important role in the simulations than in the experiments. At a typical shear rate of 15 s^{-1}, corresponding to Deborah numbers of $De = \dot{\gamma}\tau_{\mathrm{cross}} = 0.8$ and 12 for the polymer and micellar solutions respectively, the Peclet numbers are $Pe = 6\pi R_{\mathrm{col}}^3 \dot{\gamma}\eta(\dot{\gamma})/kT = 86$ and 3 respectively. While the stronger thermal fluctuations may affect the relaxation process of the sheared colloidal fluids, we do not expect the Brownian motion to significantly alter the steady state. From the below descriptions of the simulations, it indeed emerges that the smaller colloidal size is of little consequence to the shear-alignment of the colloids.

The colloid-colloid and colloid-polymer interaction potentials are plotted in Fig. 2.6 against their respective distances. For colloid-colloid interactions we choose a relatively hard potential, scaling as D_S^{-8} with the surface-to-surface distance $D_S = r - 2R_{\mathrm{col}}$ between a pair of colloids. The coloid-polymer interaction is based on previous work by Bolhuis and Louis [11], who inverted structural information from simulated sphere-polymer distribution functions. The exponential form of the potential allows the center of mass of a polymer or micellar chain to occasionally approach the center of the colloid to within less than R_{col}. This softness represents the ability of long flexible chains to enlace a colloidal particle and thereby to locate its center of mass inside the colloid.

The motions of the colloids are described by a regular Brownian dynamics expression. The displacement of colloid i over a simulation time step dt is therefore similar in nature to equation 2.10. Since the colloids can not entangle with the solvent chains, they are not subjected to entanglement forces and their friction coefficient is fixed at $\xi_i = \xi_c = 7 \cdot 10^{-7}$ kg/s. Under shear flow, the friction again acts relative to the prevailing flow field at the position of the colloid's center, resulting in the above discussed displacement contribution $+V(y_i)\hat{\mathbf{e}}_x dt$.

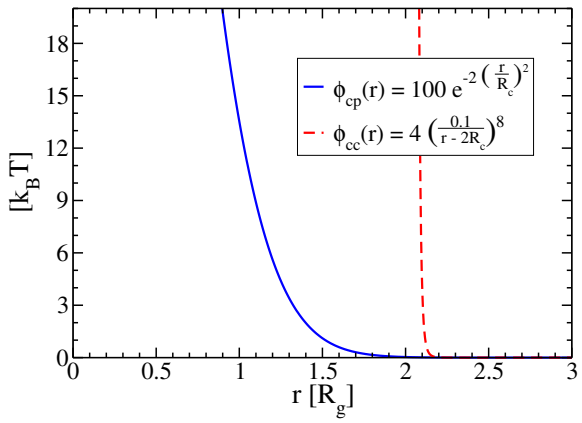

Figure 2.6: The coloid-coloid (red) and colloid-polymer (blue) interaction potentials.

2.4.2 Preparation of colloidal dispersions

The colloid-polymer potential described in Fig. 2.6 does not allow any conclusion about the volumes occupied by the colloids and excluded to the polymers. We therefore do not know how many polymers should be removed with every colloid dispersed in the liquid. In order to calculate this number, we first ran a simulation with polymers all over the box and the colloids restricted to a central region measuring about one-third of the total box volume. The colloids were kept in this dispersion of volume V_{disp} by means of two semi-permeable walls, as depicted in Fig. 2.7, that were impermeable to the colloids but permeable to the polymers. The lateral box dimensions were gradually adjusted by a barostat-like algorithm, at fixed positions of the semi-permeable walls, to allow the polymer density in the two outer regions to equilibrate to the experimental polymer density ρ_{exp}. As a result, the polymer chemical potential throughout the entire box became equal to its experimental value. The resulting number of polymers in the dispersion is by definition equal to

$$N_p^{\text{disp}} = \rho_{\text{exp}} \left(V_{\text{disp}} - N_{\text{col}} v_{\text{app}} \right), \tag{2.19}$$

where N_c is the number of colloids and v_{app} is the apparent volume occupied by one colloid. From the simulation we found $v_{\text{app}} \approx -0.2 R_g^3$. This volume value is rather different from the poorly defined volume of approximately $\frac{4}{3}\pi R_g^3$ of a colloid with soft interaction potentials; the small negative value even implies that the dispersion contains slightly more polymers

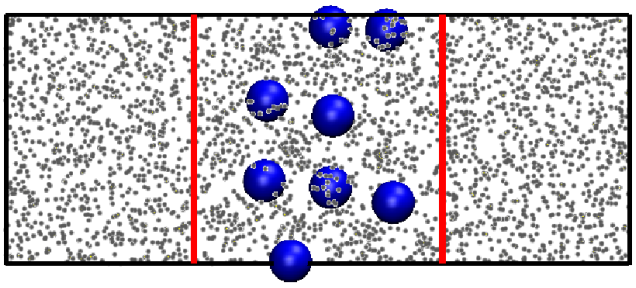

Figure 2.7: Illustration of the simulation box used to find the equilibrium chain density in the system with colloids. The polymers (gray dots) can pass through the walls (red lines), while the colloids (blue spheres) are restrained to the region between the walls. The lateral dimension of the regions external to the walls is continuously adjusted by a density-based rescaling routine in order to achieve the desired bulk polymer density in the outer regions.

than an equal volume of polymer fluid at the same chemical potential. The low apparent volume indicates that osmotic pressure of the polymer bath pushes the polymers against the colloids and thereby increases their overall density. The radial distribution function of polymers relative to colloids shows a peak at a distance of $1.6\,\mathrm{R}_g$, indicating that the polymers are condensing against the colloids. Since the polymer-colloid interaction is purely repulsive, this condensation emerges as a consequence of the inter-polymer Flory-Huggins free energy. We inserted the value for v_{app} into Eq. (2.19) to calculate the appropriate number of polymers for the various colloidal suspensions of the following sections. This procedure enabled us to find the correct density in the colloid-polymer system. Since the apparent volume of the colloid is a thermodynamic property of the interaction potentials, the aforementioned value obtained for the polymer solution also applies to colloids dispersed in worm-like micellar solutions. For completeness, we note that the colloidal ordering discussed below does not prove sensitive to the polymer density at the prevailing conditions, as very similar results were obtained upon equating v_{app} to $\frac{4}{3}\pi R_g^3$.

An important observation from the non-sheared simulations is that the colloids remain homogeneously distributed throughout the suspending fluid. The colloid-colloid radial distribution function (not shown) shows a first peak just beyond the colloidal diameter of $2\,\mathrm{R}_g$, as is usual with hard sphere systems at intermediate or high densities.

2.4.3 Colloids in sheared micellar solutions

The behavior of colloids under shear was first simulated for the solution of worm-like micelles, since this fluid is known from experiments to induce colloidal alignment in the bulk [92]. In this and all subsequent simulations, the colloids were immersed in a rectangular simulation box measuring $24 \times 16 \times 12R_g^3$. To facilitate the formation of colloidal strings, in the expectation that they would occur, the 30 colloids of the initial box were placed in a plane spanned by the shear velocity and the velocity-gradient, i.e. the xy-plane, taking care to prevent any significant overlap while randomly placing the colloids. The procedure outlined in the previous section was used to calculate the number of fluid particles filling the remaining unoccupied volume of the box. A strong shear flow of $\dot{\gamma} = 15\,\mathrm{s}^{-1}$, well beyond the transition to shear-thinning in Fig. 2.5, was imposed on the system. In order to reduce the usual complicating start-up effects at the onset of shear flow, the simulation was started at $t = 0$ with the expected steady state linear fluid velocity $V(y) = \dot{\gamma} y \hat{\mathbf{e}}_x$, and then left to evolve freely. Snapshots from the simulation at various times are shown in Fig. 2.8. The first frame shows the initial box, with the colloids distributed randomly in the xy-plane. The second and third frames, taken at 0.1 s and 2 s, respectively, clearly show a gradually increasing degree of ordering. In the last snapshot, taken after 4 s, the particles have converged to form strings along five parallel lines in the flow direction; this set of five lines survived for the next 16 seconds, at which point the simulation was terminated. Watching movies of this and similar systems revealed that the colloidal strings are anything but stationary. Besides the obvious convective motion along the shear direction, the strings repeatedly lose one or two colloids from their tails, which subsequently are caught by and become the head of the next string moving along the same flow line. The microscopy image in figure 2a of ref. [92] suggests similar behavior under experimental conditions, as the photographed strings of colloids resemble trains running along the same track. The order of the colloids along the flow line typically stays the same, though we have seen occasions where a colloid briefly left a string and was overtaken by (part of) the string before returning to the flow line. The five lines also performed erratic Brownian motions, thus changing their vertical spacing and gradually drifting away from the initial $z = 0$ plane.

To quantify the degree of colloidal alignment, the area covered by the colloids in a projection onto the yz-plane was computed as a function of time. Figure 2.9 shows how this covered

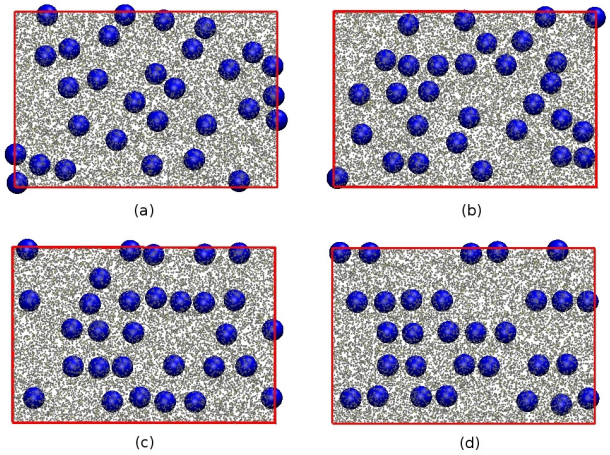

Figure 2.8: Snapshots of 30 colloids (blue spheres, volume fraction $\varphi = \frac{4}{3}\pi N_{\mathrm{col}} R_{\mathrm{col}}^3 / V_{\mathrm{box}} = 3\%$*), initially distributed over the xy plane, with the shear flow along the horizontal x-direction and the velocity-gradient along the vertical y-direction. The pictures show projections on the xy-plane at (a)* $t = 0\,s$*, (b)* $t = 0.1\,s$*, (c)* $t = 2\,s$ *and (d)* $t = 4\,s$ *after the onset of a* $\dot{\gamma} = 15\,s^{-1}$ *shear in a 3D worm-like micellar solution (gray dots). Side views of this system after 0 and 20 s are included in Fig. 2.9.*

area initially decreased rapidly, reached a plateau after around 3 s, and remained essentially constant from this time onward. The inset displays snapshots at the beginning and end of the simulation, which clearly show that the system evolved from a disordered to an ordered configuration. Note that one colloid, near the bottom of the second snapshot, has escaped from the *xy* plane to wander around on its own.

One may object that the above ordering could be a consequence of our starting with all colloids confined to a single plane. We therefore also performed simulations on a system containing 80 colloids which were initially placed randomly throughout the entire box, again taking care to avoid overlap when generating the configuration. Figure 2.10 shows the evolution, at a shear rate of $\dot{\gamma} = 15\,\mathrm{s}^{-1}$, of the *yz* area occupied by the colloids as a function of time. The high initial coverage of nearly 80% rapidly decreases over the course of about 7 seconds to a stable level of just under 50%. This decrease is also evident from the snapshots, shown as insets to the figure, of the initial and final configuration of the 22 s long simulation.

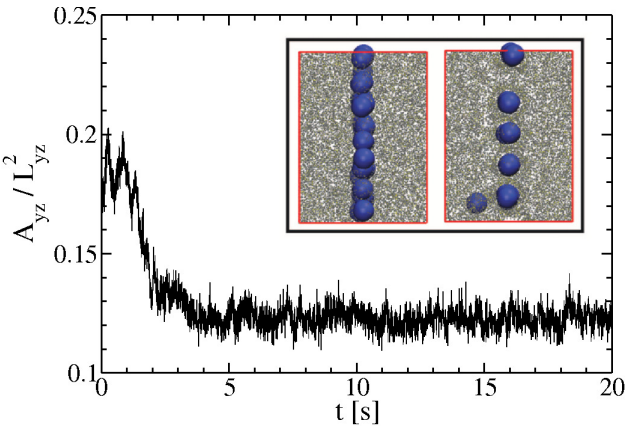

Figure 2.9: The fraction of the yz-plane covered by colloids, as a function of time, in a wormlike micellar solution sheared at $\dot{\gamma} = 15\,s^{-1}$. The 30 colloids were initially randomly distributed over the xy-plane, as shown in the left inset. At the end of the 20 s run, the colloids were arranged into five lines, as is clearly visible in the right inset. Note how one colloid near the bottom of the box has escaped the xy-plane. Four snapshots showing front views of the aligning process are shown in Fig. 2.8.

Interestingly, the final configuration suggests that the strings of colloids adopt an hexagonal ordering in the *yz*-plane.

A second method to quantify the alignment of the colloids is to count the number of colloidal strings and their lengths. For particles i and j to qualify as neighboring members of the same colloidal string, the difference vector $\mathbf{r}_{ij}$ between their centers had to be limited (i) in the flow direction to $|r_{ij,x}| \leq 3R_g$, and (ii) in the perpendicular direction by $r_{ij,y}^2 + dr_{ij,z}^2 \leq (0.5R_g)^2$. A simple algorithm then grouped all neighbor-linked colloids together to identify all strings of at least two colloids. The inset in Fig. 2.11 shows that, under shear, the 80 randomly distributed colloids grouped into a steadily growing number of strings, which after about 4 seconds reached a steady value at about 18 strings. Of course, the precise number of colloidal strings varies with the definition of neighbors, but the overall result clearly confirms the shear-alignment implied by the reduction of the projected *yz*-area. Figure 2.11 also shows the distribution of colloids over the various string lengths, at several intervals during the simulation. The approximate 70 colloids in 'strings' of one colloid over the first second of the

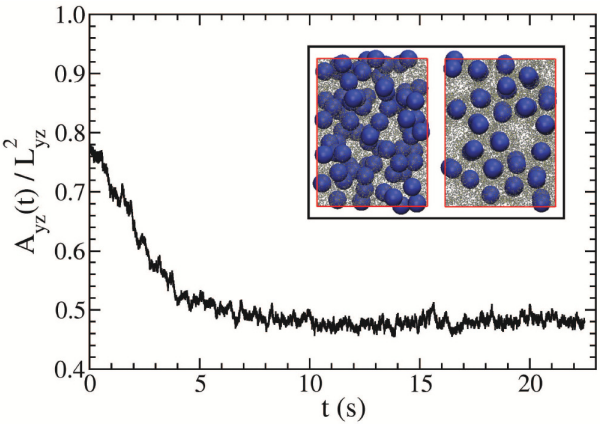

Figure 2.10: Fractional area of the yz plane occupied by 80 colloids, $\varphi = 7\%$, as an initially dispersion in a worm-like micellar solution gradually orders under a simple shear flow of $\dot{\gamma} = 15\,s^{-1}$. The inset displays snapshots in the yz-plane of the initial (left) and final (right) configurations.

simulation confirms that the colloids are initially randomly distributed. At the intermediate times from 2 to 3 seconds and from 4 to 5 seconds, the number of free colloids decreases as ever more and longer strings are being formed. The average number of free colloids at the end of the simulation, from 19 to 20 seconds, has reduced by 5 more colloids, but the most notable change is the growth of the long chains.

The dominant center-to-center distance between colloids in these strings, as derived from the first peak in the in-line distance distribution (not shown), lies at about $2.4\,R_g$. Hence, the colloids hardly touch each other, as their interaction energy is virtually zero at this separation, while at the same time the space between consecutive colloids is too narrow to accommodate fluid particles, as was confirmed by examining movies of the system. The latter suggests that depletion interactions may be contributing to the stability of shear-induced colloidal strings, though we recall that our earlier observations showed that the depletion interactions at zero shear are too weak to induce alignment. Combining the average spacing with the box dimensions, we note that the longest possible chain is expected to contain 10 colloids, well beyond the longest string observed in our simulations.

The evolutions of the shear stresses S_{xy} in the pure fluid and the suspension are plotted

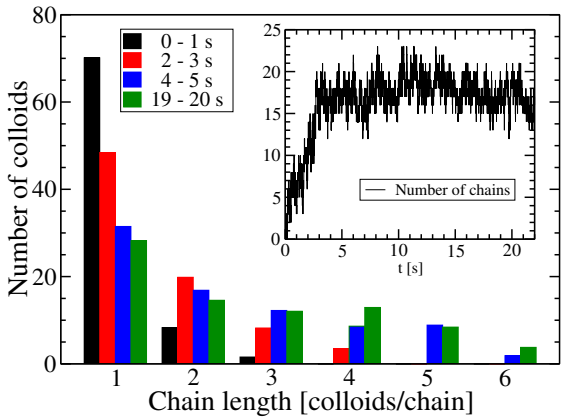

Figure 2.11: Histogram of the number of colloids in chains of given lengths, averaged over four intervals of one second, for initially homogeneous suspension of 80 colloids, in a worm-like micellar solution sheared at $\dot{\gamma} = 15\ s^{-1}$. The sum area of all bars at any given time equals the total number of colloids in the system. The inset shows the number of colloidal string as a function of time. See the main text for the operational definition of a string. Only strings of two or more colloids are counted.

in Fig. 2.12. Since the simulations were started with the expected linear steady state velocity profile, the shear stress in the pure fluid almost immediately reaches its steady state value. The shear stress of the colloidal suspension initially decays fast, but after approximately 5 seconds only a very slow decrease remains which appears to converge to a steady level. This transition time roughly coincides with the time it takes for the randomly distributed colloids to aggregate into strings, as follows by a comparison of Figs 2.10 and 2.12, which in combination with the absence of start-up effects in the pure fluid suggests that colloidal alignment reduces the shear stress. The alignment proceeds faster than under experimental conditions because we have stepped over the slow evolution from a quiescent fluid to a steady sheared state, because the colloidal concentration is higher by about one order of magnitude, and possibly also benefits from the enhanced Brownian motions of the smaller colloids. Since the rate of energy dissipation by the sheared fluid is given by $P = S_{xy}\dot{\gamma}L_z$, the decreasing shear stress may be re-interpreted as an evolution of the colloidal suspension towards a steady state requiring minimum power dissipation. Interestingly, we observed similar relaxations to steady

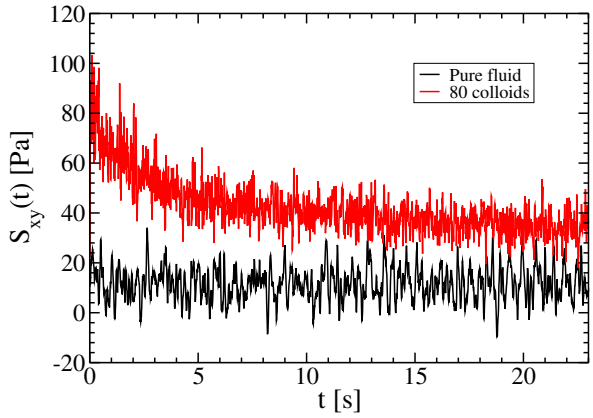

Figure 2.12: The shear stress S_{xy} against time for a worm-like micellar solution containing 80 initially randomly distributed colloids (red), at a constant shear rate of $\dot{\gamma} = 15\,s^{-1}$, and for the pure fluid (black). The former has a higher viscosity because of the suspended colloids, as well as due to the higher micellar concentration, dictated by the constant chemical potential (see Section 2.4.2).

states of minimum dissipation in several system that we studied recently, including shear-banding of a viscoelastic fluid in RaPiD simulations [115, 116] and segregation of granules in a rotating drum [5], which tentatively suggests that a reduction of the dissipation rate may act as a driving mechanism inducing ordering in driven systems. For an extensive discussion on possible generic physical laws governing non-equilibrium steady states, and the evolution toward these states, we refer the reader to the review of Martyushev and Seleznev [77] and the book by Öttinger [85].

In our simulations, a sufficiently high shear rate proved crucial to the shear-induced alignment of colloidal particles, as we did not observe any spontaneous alignment at shear rates below $3\,\mathrm{s}^{-1}$. At these low shear rates, it is conceivable that the time scale of string formation exceeds the simulation time scale of about 20 s. We therefore investigated the stability of pre-assembled chains of colloids at these low shear rates. Figure 2.13 shows the projected area A_{yz} against time for simulation boxes prepared with 12 strings of 8 colloids each, at an inter-colloid spacing of $2.4\,R_g$. The area increases approximately linearly in time for shear rates of $1\,\mathrm{s}^{-1}$ and below, including a non-sheared system, and thereby indicates that the colloids

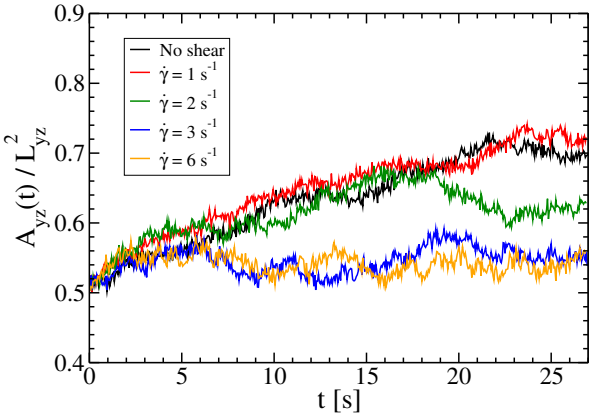

Figure 2.13: Projected area A_{xy} occupied by 96 colloids, $\varphi = 9\%$, in worm-like micellar solutions at various shear rates. All simulations started from a perfectly aligned configuration with 12 strings of 8 colloids each.

gradually disordered at these low shear rates. At $\dot{\gamma} = 2\,\mathrm{s}^{-1}$ the area initially increased but then decreased again to settle at a somewhat 'undecided' level. For $\dot{\gamma} \geq 3\,\mathrm{s}^{-1}$ the projected area fluctuated around a constant value, slightly higher than the area of the perfectly aligned initial system, indicating that the alignment is stable at these high shear rates. These observations are in agreement with experimental observations of a critical shear rate of about $1\,\mathrm{s}^{-1}$ for large colloidal particles dispersed in the bulk worm-like micellar solution modeled here [92]. In all simulations of the micellar fluid, with and without colloids, the velocity profile $V(y)$ of the flowing fluid was virtually linear, indicating that colloidal alignment does not require shear banding. This observation is also in agreement with experiments [92], which indicate that shear-banding can promote alignment but is not a prerequisite.

2.4.4 Colloids in sheared polymer solutions

The preceding study on colloids in a worm-like micellar solution was repeated for colloids dispersed in the polymer solution. Following the same procedures, we first placed 30 colloids randomly in the *xy*-plane and applied a shear flow of $\dot{\gamma} = 15\,\mathrm{s}^{-1}$ in the *x*-direction. This time, however, the colloids remained homogeneously distributed. We increased the shear rate stepwise in a set of simulations, but even at the highest shear rate of $\dot{\gamma} = 200\,\mathrm{s}^{-1}$ the

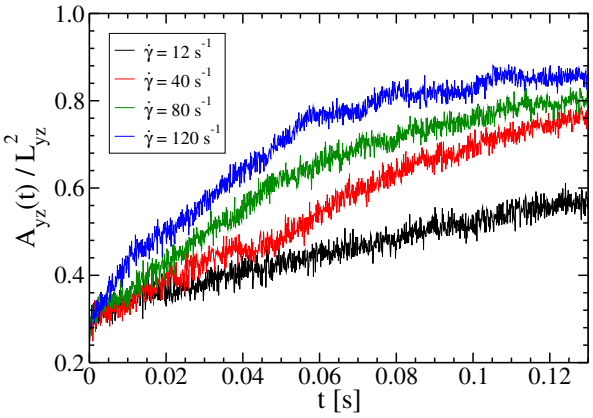

Figure 2.14: The occupied projection area in the yz-plane by 96 colloids, initially forming 12 flow-aligned strings, dispersed in polymer solutions under at various shear rates.

colloids still did not align. Next, we distributed 80 colloids randomly throughout the entire box and ran simulations over the same range of shear rates. Again, the particles remained randomly distributed at all applied shear rates up to $\dot{\gamma} = 200\,\mathrm{s}^{-1}$.

To rule out low diffusivity as a possible cause for the absence of colloidal chains in the polymer solution, we also performed simulations on initial configurations of 96 colloids forming 12 straight lines along the flow direction. The projected area covered by these colloids gradually increased, see Fig. 2.14, indicating that the colloids were diffusing away from their initial ordered state to a disordered state. In fact, the misalignment proceeded quicker at higher shear rates, probably because the particles were moving faster with the flow. From this we learn that, even though the polymer solution behaves as a shear thinning viscoelastic fluid with a thinning-exponent of nearly -1, no ordering of particles is to be expected. This observation agrees with the experimental observation that colloids in this polymeric fluid do not align in the bulk (but migrate to the rheometer walls and align there) [93, 118], and confirms that bulk alignment is limited to a subset of shear-thinning fluids. In contrast to the wormlike-suspension, the shear stress and hence the power dissipation in the polymeric suspension reach their steady state values already after 0.05 seconds.

2.5 Conclusions

We have performed coarse-grained simulations of colloidal particles dispersed in two viscoelastic fluids with rheological behaviors typical of semi-dilute solutions containing polymers and worm-like micelles, respectively, at a volume fraction of 11% or nearly 15 times the critical overlap concentration. Each polymeric or micellar chain was represented by a single particle in Responsive Particle Dynamics (RaPiD), enabling simulations covering large length and time scales; in this study, a standard desktop processor sufficed to simulate fluid volumes of $0.3\,\mu\mathrm{m}^3$ for 20 s. In order to recover the rheological behavior of the fluids, the particles were endowed with configuration and time-dependent memory effects which qualitatively describe the entanglement effects responsible for the dynamics of the real chains. This study shows that the markedly different rheological behaviors of two shear-thinning fluids are well reproduced quantitatively by RaPiD simulations, through the adjustment of a few simulation parameters. For convenience we here endowed both fluids with identical thermodynamic properties, to specifically concentrate on the impact of fluid rheology on the ordering of suspended colloids in sheared bulk suspensions. The simulations showed that the colloids formed strings along the shear direction in the worm-like micellar solution, provided the shear rate exceeded $2\,\mathrm{s}^{-1}$, while the colloids in the polymeric solution remained homogeneously dispersed throughout the bulk at all shear rates. These results are in good agreement with recent experimental studies in the group of Vermant on colloids dispersed in the two fluids modeled here, reporting alignment in the bulk worm-like solution beyond $1\,\mathrm{s}^{-1}$ and disorder in the bulk of the polymeric solution [92, 93, 118].

The simulations indicate that the shear-aligned colloids are nearly touching, leaving insufficient space for worm-like micelles to reside between consecutive colloids. While this suggests that depletion interactions are involved in the colloidal alignment, we note that depletion interactions were not capable of inducing aggregation at low and vanishing shear rates, nor can these thermodynamic attraction forces explain the marked difference in colloidal aggregation between micellar and polymeric solutions (since the simulated fluids share thermodynamic behavior). These results are supported by experiments, with the colloids nearly touching under shear in the micellar solution but randomly dispersed at low shear rates in both solutions [92, 118]. Hence, we are led to speculate that the depletion forces are secondary to a still unidentified flow-induced driving force, which in the bulk micellar

solution is sufficiently strong to overcome Brownian motion but in the bulk polymer solution is weak or absent. An interesting observation in this respect is the decreasing power dissipation by the dispersion concomitant with increasing colloidal alignment, which might place this ordering phenomenon within the wider – yet still incompletely understood – context of dissipative non-equilibrium steady states [77, 85].

An important difference between the simulation approach advocated here and the approaches taken by most authors studying colloids in viscoelastic fluids [24, 53, 97, 125] is that we do not employ a numerical Navier-Stokes solver to explicitly calculate the flow field throughout the entire simulation box. The RaPiD approach drastically reduces the computational burden, thereby enabling RaPiD to simulate larger systems with more colloids and in full three-dimensional space.

We express the hope that additional studies with the RaPiD method, by systematically exploring the effects of the fluid parameters, will help elucidate the intriguing mechanism behind shear-induced alignment in the bulk, as well as at the walls.

Appendix A: Flory-Huggins free energy for a system of chains with fixed central segment

In this appendix we present the potential of mean force that we have used in our simulations. Out of all degrees of freedom in our system we only keep track of the central monomer of each polymer. The potential of mean force therefore is the free energy of all polymers for given position of their central monomers. We will calculate this free energy using a Landau-de Gennes type of description of inhomogeneous systems.

Consider a very large box of volume V containing N_s solvent molecules and N_p polymers each consisting of p Kuhn lengths. According to the incompressible Flory-Huggins model the total free energy A may be calculated according to

$$A = -kT \ln Q_{N_s,N_p}, \tag{A.1}$$

$$\begin{aligned} Q_{N_s,N_p} &= \left(\frac{q_s^{int}}{\Lambda_s^3}\right)^{N_s} \left(\frac{q_p^{int}}{\Lambda_p^3}\right)^{pN_p} \left(\frac{z-1}{M}\right)^{N_p(p-1)} \\ &\times \frac{M!}{N_s!N_p!} \exp(-\beta U) \Delta^{N_s+pN_p}, \end{aligned} \tag{A.2}$$

where $M = V/\Delta$ is the number of cubes of size Δ into which the total volume has been divided and z is the coordination number of the lattice that has been used. Furthermore, q_s^{int} and q_p^{int} are single particle partition functions accounting for internal degrees of freedom in each lattice cell, and Λ_s and Λ_p are the corresponding thermal de Broglie wavelengths. Finally, U is the average interaction energy

$$U = \frac{1}{2} z \left\{ \frac{N_s^2}{M}(-\varepsilon_{ss}) + 2p\frac{N_s N_p}{M}(-\varepsilon_{sp}) + p^2\frac{N_p^2}{M}(-\varepsilon_{pp}) \right\}, \tag{A.3}$$

where ε_{ij} are interaction energies between neighboring cubes of species i and j. On average the central segments of the polymers will be homogeneously distributed throughout the box. Thermal fluctuations around this homogeneous distribution must be sampled correctly by our simulations. In order to achieve this we must calculate the relative probabilities, i.e. the relative free energies of such fluctuations. First notice that if we reshuffle the central segments in order to generate a fluctuation, the number of solvent molecules and the number of polymers do not change. We may therefore eliminate all contributions to the free energies which are linear in the number of solvent molecules or the number of polymers from further considerations. We are then left with

$$A' = kTN_p \ln\left(\frac{N_p}{M}\right) + kTN_s \ln\left(\frac{N_s}{M}\right) - \frac{p^2 N_p^2}{M}\chi. \tag{A.4}$$

$$\chi = \frac{1}{2}\beta z(\varepsilon_{ss} + \varepsilon_{pp} - 2\varepsilon_{sp}), \tag{A.5}$$

where χ is the Flory-Huggins parameter. Next we notice that the simulated degrees of freedom take care of

$$A^{sim} = -kT \ln\left(\frac{V^{N_p}}{N_p!}\right). \tag{A.6}$$

The free energy of the eliminated degrees of freedom may therefore be taken to be $A' - A^{sim}$, which on neglecting the terms proportional to N_p leads to

$$A'' = kTpN_p \left\{ \frac{1-\phi}{\phi}\ln(1-\phi) - \chi\phi \right\}, \tag{A.7}$$

where we have introduced the volume fraction

$$\phi = p\frac{N_p}{M}. \tag{A.8}$$

In order to discriminate the various inhomogeneous distributions of the central segments from one another, we have introduced local densities $\phi_i(r)$ around each particle i. We now assume that the corresponding (relative) free energies may be approximated as

$$\Phi_C(r) = kTp\sum_{i=1}^{N_p}\left\{\frac{1-\phi_i(r)}{\phi_i(r)}\ln(1-\phi_i(r))-\chi\phi_i(r)\right\} \tag{A.9}$$

$$= \sum_{i=1}^{N_p} kTa^p(\phi_i(r)), \tag{A.10}$$

where the second line serves to define $a^p(\phi_i(r))$.

The force acting on each particle can now be expressed in terms of the local volume fraction as

$$\mathbf{F}_i = -\nabla_i A[\rho] = -\nabla_i \sum_{j=1}^{N} a^p(\phi_j) = -\sum_{j=1}^{N} \frac{da^p(\phi_j)}{d\phi_j}\frac{\partial\phi_j}{\partial\rho_j}\frac{\partial\rho_j}{\partial\mathbf{r}_i}, \tag{A.11}$$

which results in a quasi-pairwise interaction (quasi because the local density does depend on the location of other particles):

$$\mathbf{F}_i = -\frac{1}{\rho_{max}}\sum_{j=i}^{N}\left(\frac{da^p(\phi_j)}{d\phi_j}+\frac{da^p(\phi_i)}{d\phi_i}\right)\frac{\partial}{\partial\mathbf{r}_i}\omega(r_{ij}) \tag{A.12}$$

3 The origin of flow-induced alignment of spherical colloids in shear-thinning viscoelastic fluids

We have studied the poorly understood process of flow-induced structure formation by colloids suspended in shear-thinning fluids. These viscoelastic fluids contain long flexible chains whose entanglements appear and disappear continuously as a result of Brownian motion and the applied shear flow. Responsive Particle Dynamics (RaPiD) simulates each chain as a single smooth Brownian particle, with slowly evolving inter-particle degrees of freedom accounting for the entanglements. The colloids mixed homogenously in all simulated quiescent dispersions, and they remain dispersed under slow shear flow. Beyond a critical shear rate, which varies depending on the fluid, the colloids aggregate and form flow-aligned strings in the bulk of the fluid. In this chapter we explore the physical origins of this hitherto unexplained ordering phenomena, both by systematically varying the parameters of the simulated fluids and by analyzing the flow-induced effective colloidal interactions. We also present an expression for the critical shear rate of the studied fluids.

3.1 Introduction

Suspensions of colloids in non-Newtonian fluids find many technological applications mainly because of their complex flow behavior affecting in various ways the distribution of the suspended particles. Directed assembly of colloids in flowing fluids has attracted much attention because it can be very useful in practical applications, e.g. it is widely used in industrial

processes, for biological materials and for nanocomposites fabrication, as well as for giving rise to undesired segregation effects [40, 119]. In this chapter, we study the behavior of spherical colloids immersed in shear-thinning viscoelastic fluids, i.e., fluids which have the characteristic of decreasing viscosity with increasing rate of shear.

It is known that spheres in dilute or semidilute viscoelastic polymer solutions form strings in the presence of flow, usually oriented in the flow direction [72,82,92,103,122]. As soon as the flow is ceased or the shear rate drops below a critical value, the colloids again disperse to distribute homogeneously over the fluid's volume. This ordering phenomenon is still poorly understood, though it has already been found that alignment does not take place in Newtonian fluids nor in viscoelastic fluids with constant viscosity. Therefore, shear thinning and viscoelasticity both seem to be necessary conditions to observe string formation.

The problem of simulating colloids dispersed in viscoelastic fluids has been considered before by a number of groups, using continuum methods combined with various constitutive equations to calculate flow fields subject to the boundary conditions posed by the colloids. Feng *et al.* [34], Binous and Phillips [9], Harlen [43], Yu *et al.* [125], and Ardekani *et al.* [4] numerically studied one or two spheres sedimenting through a viscoelastic fluid, and D'Avino *et al.* [20–22] analyzed the rotation of a particle in a sheared viscoelastic liquid and the shear-induced migration of a particle toward a wall. Flow-induced aggregation of a dozen colloids in a viscoelastic solution was simulated in two dimensions by Yu *et al.* [125] for sedimenting particles and by Phillips and Talini [97] and Hwang and Hulsen [53] for suspensions exposed to a shear flow. Thus far no three-dimensional continuum simulations have been done with more than two particles.

In order to have access to three-dimensional suspensions containing dozens of colloids we recently [102] made use of a particle based model to simulate large amounts of visco-elastic polymer solutions. This model, based on the Responsive Particle Dynamics (RaPiD) method [14, 117], allows simulations of thousands of polymers in solutions or in the melt. In order to achieve this goal each polymer is represented by its center of mass only. Memory effects are introduced into the model by dressing the particles with a few structural properties (see Section 3.2). An additional advantage of a particle based model over continuum models is that it automatically allows for gradients of polymer concentrations and fluctuations thereof.

The results from computer simulations with the RaPiD model presented in Chapter 2

showed that shear-alignment happens in a fluid with the flow characteristics of a particular wormlike micellar solution, as it was first observed by experiments [92]. Moreover, a second shear-thinning fluid, modelling a particular polymer solution, did not present alignment in the range of shear rates tested, also in agreement with experiments. In the present chapter we carry out further investigations on the alignment process of colloids in shear-thinning viscoelastic fluids. In an attempt to find regularities that might relate flow-alignment to the fluid and flow properties, we have systematically varied the fluid's simulation parameters and the shear rate. The shear-thinning fluids and their colloidal dispersions are described in Section 3.3.1 and Section 3.3.2, respectively. In Section 3.4 we investigate how the colloid-colloid interactions and the particle distribution around the colloids are modified under different shear rates and simulation input parameters, for a more in-depth understanding of the ordering process.

3.2 Method

The molecules responsible for the rheological properties of shear-thinning viscoelastic fluids typically used in experiments on shear alignment of colloids are dissolved long polymeric chains. In order to reach the large time and length scales involved in colloidal alignment, we will coarse-grain these chains to be represented by the positions r of their centers of mass. Since the proper equilibrium distribution of these N_p centers of mass is determined by all coordinates in the system, the influences of the eliminated chain and solvent coordinates must be accounted for by means of an effective potential of mean force between the simulated particles. It is well known that fluctuations in the distribution of the centers of mass evolve very slowly as a result of complicated entangling and disentangling of the chains. This effect is included in the RaPiD model by extending the set of relevant variables with the 'entanglement numbers' n and modifying the potential energy of the system into

$$\Phi(r,n) = \sum_{i=1}^{N_p} a^p(\phi_i) + \frac{1}{2}\alpha \sum_{i,j}^{N_p} (n_{ij} - n_0(r_{ij}))^2, \tag{3.1}$$

as will be discussed next.

The first sum on the right-hand side describes the potential of mean force, which governs the system's equilibrium thermodynamics. The configurational free energy of a system

consisting of long flexible chains in a solvent is well described by the Flory-Huggins (FH) theory [36, 51]. We adapt the FH model to calculate the free energy for each chain in a given local configuration of centers of mass [102]. The total free energy is then a sum over the free energies per particle a^p, given by

$$a^p(\phi_i) = pkT\left[\frac{1-\phi_i}{\phi_i}\ln(1-\phi_i) - \chi\phi_i\right], \tag{3.2}$$

where p is the number of Kuhn segments in the chain, χ is the Flory-Huggins parameter, k is Boltzmann's constant, T is the temperature, and where the local chain volume fraction ϕ_i around particle i is computed as

$$\phi_i = \frac{1}{\rho_{max}}\sum_{j=1}^{N_p}\omega(r_{ij}). \tag{3.3}$$

The weight function $\omega(r)$ is a normalized function that describes how the contributions to the local density change as a function of the distance between the particles. This weight function should satisfy several conditions: it needs to be a decreasing function that goes to zero at the cutoff radius, its derivative cannot be zero at the origin in order to avoid the absence of repulsive forces at short distances – which would induce the formation of clusters – and it must smoothly decay to zero near the cut-off distance r_c in order to prevent discontinuities in the force – which would result in spurious density correlations – at the cutoff. As depicted in Fig. 3.1, these conditions are obeyed by a linear profile $\omega(r)$ smoothly changing into a quadratically decaying $\omega(r)$ at the switch radius r_s (see Table 3.1). Lastly, ρ_{max} in Eq. (3.3) defines the maximum local density the system is allowed to reach, i.e. the density in the absence of solvent between the polymeric chains, and thereby renders $\phi_i \leq 1$.

The second sum on the right-hand side of Eq. (3.1) gives rise to transient forces on the particles in the system. In fully atomistic simulations, the internal structure of the polymeric chains will be found to be correlated with the recent displacements of their centers of mass, in a way that on average tends to drive the system back to it's previous state. As a result, the instantaneous forces on the centers of mass will usually be different from the averaged forces measured if these centers had been fixed to their instantaneous positions for a very long time; the latter forces constitute the potential of mean force, as described by the first sum in Eq. (3.1). The differences between the actual and the average forces are the 'transient forces' referred to above. They are transient in the sense that they will gradually fade away – decaying from restoring forces to thermal noise – in case all centers of mass are suddenly kept fixed

Simulation parameter	**Symbol**	**Value**
Temperature	T	300 K
Radius of gyration	R_g	40 nm
Density	ρ_p	3.5 particles/R_g^3
Average volume fraction	ϕ	$0.11 \rightarrow \rho_p \approx \rho_{\max}/9$
Flory-Huggins parameter	χ	0.5
Number of monomers	p	2700 mon./polymer
Solvent friction	ξ_s	$2.45 \cdot 10^{-9}$ kg/s
Cut-off radius	r_c	$2.5R_g$
Switch radius	r_s	$1.0R_g$
Entanglement cut-off radius	r_e	$2.55R_g$
Entanglement relaxation time	τ	200 s
Model fluid 1 (MF1)		
Entanglement strength	α	$0.1kT$
Entanglement friction	ξ_e	$7 \cdot 10^{-7}$ kg/s
Model fluid 2 (MF2)		
Entanglement strength	α	$10kT$
Entanglement friction	ξ_e	$5 \cdot 10^{-9}$ kg/s

Table 3.1: The simulation parameters of the model fluids.

at their respective positions. In the RaPiD model the effect of transient forces is introduced by adding to the potential a quadratic contribution $\frac{1}{2}\alpha(n_{ij} - n_0(r_{ij}))^2$ with every pair of particles, see Eq. (3.1). Here n_{ij} is a dynamical variable, called the 'number of entanglements' between particles i and j, and $n_0(r_{ij})$ is the equilibrium number of entanglements between two particles, defined as decaying quadratically with the distance r_{ij} between the two particles, as illustrated in Fig. 3.1. Thus, the transient potential represents deviations of the actual free energy for a given configuration of the centers of mass from its average value at that particular configuration, due to deviations of the entanglement numbers from their equilibrium values. In the RaPiD simulations, the entanglement number n_{ij} is initiated as soon as particles i and j approach each other to within the entanglement cut-off radius r_e, with $r_e > r_c$, by drawing a random value from the normalised distribution $P(n_{ij}) \propto \exp\{-\frac{1}{2}\alpha n_{ij}^2/kT\}$. The

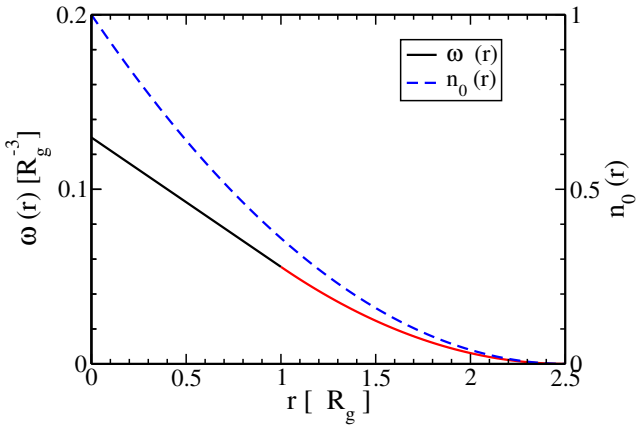

Figure 3.1: The local density weight function $\omega(r)$ decays linearly (black line, left axis) at pair distances upto the switching distance r_s, followed by quadratic decay (red line, left axis) to zero at the cut-off radius r_c. The volume integral of the weight function equals unity. The equilibrium entanglement function $n_0(r)$ decays purely quadratically (blue dashed line, right axis) from unity at $r = 0$ to zero at the cut-off.

entanglement numbers are updated during a simulation step dt according to the Brownian equation of motion [14, 117]

$$\begin{aligned} dn_{ij} &= -\frac{1}{\xi_t}\frac{\partial}{\partial n_{ij}}\Phi(r,n)dt + \sqrt{\frac{2kTdt}{\xi_t}}\Theta_{ij}(t) \\ &= -\frac{1}{\tau}(n_0(r_{ij}) - n_{ij})dt + \sqrt{\frac{2kTdt}{\xi_t}}\Theta_{ij}(t) \end{aligned} \tag{3.4}$$

where the random changes in the last term are generated by the time-dependent Markovian scalar Θ_{ij} with zero mean, unit variance and without correlation across particle pairs, and where ξ_t behaves as an 'entanglement friction' coefficient, related by $\xi_t = \alpha\tau$ to the entanglement relaxation time τ. For computational efficiency, the transient forces between i and j are turned off when their separation exceeds r_e. An important characteristic of the transient forces is that at equilibrium they average to zero in such a way that the thermodynamical properties of the system are still only governed by the conservative potential [117].

The position of particle i is updated during the simulation with the Brownian dynamics

propagator [14, 117]

$$d\mathbf{r}_i = -\frac{1}{\xi_i}\nabla_i\Phi(r,n)dt + \nabla_i\left(\frac{kT}{\xi_i}\right)dt + V(y_i)\hat{\mathbf{e}}_x dt + \sqrt{\frac{2kT\,dt}{\xi_i}}\boldsymbol{\Theta}_i(t). \tag{3.5}$$

The first term on the right-hand side gives the contribution of the potential forces to the particle's displacement, with ξ_i the particle's friction coefficient. The last term describes Brownian motion of the particles, where $\boldsymbol{\Theta}_i$ is a time-dependent Markovian random vector with unit variance, zero mean and devoid of correlations across particles. Note that these random forces and frictions represent influences of the eliminated degrees of freedom that are not accounted for by the transient forces. The friction coefficient ξ_i is assumed to be proportional to the number of entanglements of particle i with its neighbors, and is expressed as

$$\xi_i = \xi_s + \xi_e \sum_{j\neq i} \sqrt{|n_{ij}|n_0(r_{ij})}, \tag{3.6}$$

where ξ_s is the solvent friction and ξ_e defines the friction per entanglement. Since ξ_i is not constant, the second term on the right-hand side of Eq. (3.5) has been added to correct for the so-called spurious drift [84]. The third term in Eq. (3.5) describes motion along the flow with the local streaming velocity $V(y_i)$, where the shear flow is applied along the $\hat{\mathbf{e}}_x$-axis with an overall velocity gradient $\dot{\gamma}$ in the y-direction imposed by Lees-Edwards sliding boundary conditions [3]. Details on the calculation of the instantaneous velocity profile $V(y)$ are described in the references [86, 102, 109, 116]. Of course, $V(y) = 0$ for quiescent systems.

The RaPiD method as described here, or with slight modifications in the potential, has already been used in many applications where the inclusion of transient forces proved important for a successful description of the system properties [63, 64, 88, 90, 108, 109, 115]. In Chapter 2 we performed simulations of spherical colloids dispersed in viscoelastic fluids in order to investigate whether we could reproduce the experimentally observed colloidal alignment, or the absence thereof, when these suspensions are subjected to shear flow [102]. In these simulations we used the RaPiD model to represent two specific viscoelastic fluids and tuned the parameters to obtain reasonable agreement with the experimentally determined rheological properties. After adding the colloids to the fluids, we found no alignment in the quiescent state. On shearing the systems, however, we observed the alignment of colloids in one fluid but not in the other, in excellent agreement with the experimental observations [92].

In the former fluid, stopping the shear flow caused the aligned colloids to gradually disperse throughout the liquid to recover a homogeneous solution.

3.3 Colloidal alignment

In this chapter we set forth to investigate the origin and causes of the observed behavior. In order to do so we first generate a substantial amount of information on possible chaining in a large variety of visco-elastic solvents. The latter are obtained by changing some of the parameters in the RaPiD simulation model. The range of the parameters is chosen such as to include two particular liquids that were studied in our previous work [102]. We stress that these liquids were tuned to have linear and non-linear rheological properties equal to two liquids that were used experimentally.

3.3.1 Visco-elastic solvents

Since the colloids do not aggregate in quiescent fluids, it is evident that the phenomenon can not be driven by thermodynamic properties alone. In order to focus on the influence of the flow conditions, we decided to concentrate on fluids with identical thermodynamic properties but with different dynamical behavior. The differences between the fluids investigated in this paper then depend on just a few parameters of the RaPiD model. In order to reduce the differences even further, we decided to set the characteristic entanglement time τ [see text below Eq. (3.4)] equal to infinity in all cases. This leaves us with a model in which the number of entanglements between each pair of RaPiD particles, after initiation, remains constant till the pair splits up at $r_{ij} = r_e$. Since a value of infinity precludes the use of the fluctuation dissipation theorem to control the temperature, we in practice employed a very large value of 200 s for τ. We note that the particle friction coefficients calculated by Eq. (3.6) are dominated by the entanglement-related friction term, $\langle \xi_i \rangle \gg \xi_s$, due of the large number of pair contacts in the current simulations. Therefore, the fluids that we investigate differ only in the values taken by the RaPiD parameters α and ξ_e. The remaining parameters of the model fluids are listed in table 3.1.

All simulations in this section were carried out in cubic boxes containing 1201 coarse-grained particles in a volume $V = 343R_g^3$, with R_g the radius of gyration of the polymeric

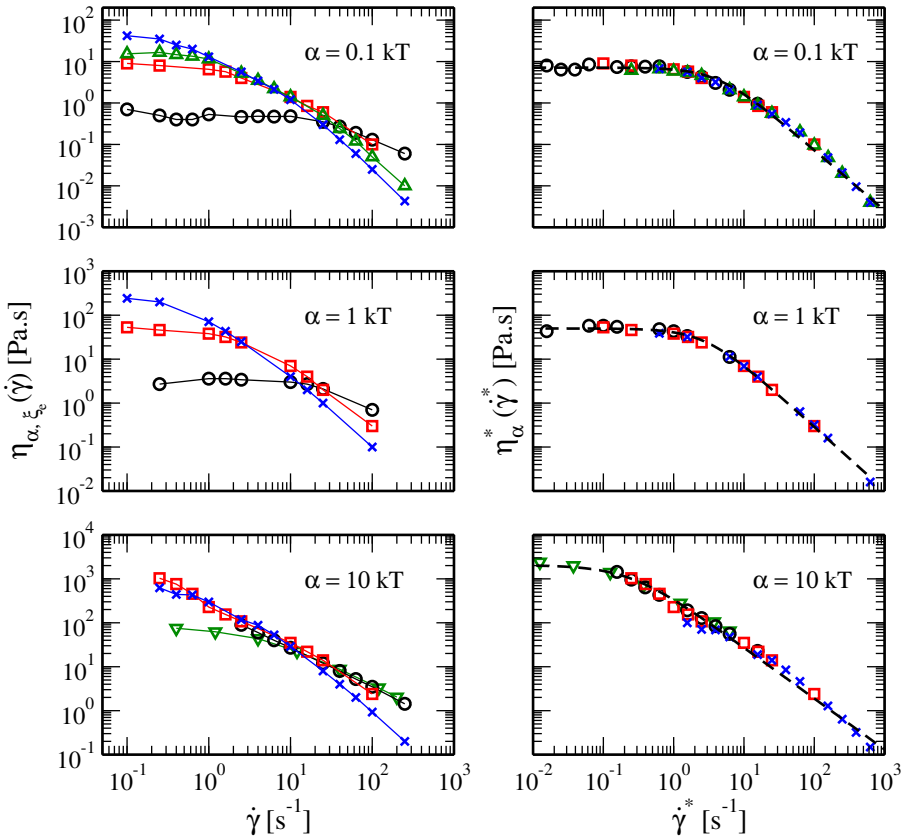

Figure 3.2: Shear viscosity curves for three values of α, at friction coefficients ξ_e of 10^{-8} kg/s ($\circ$), 1.6×10^{-7} kg/s ($\square$, later on used as the reference friction ξ_0) and 10^{-6} kg/s ($\times$). The combinations $\alpha = 0.1kT$ with $\xi_e = 7\cdot10^{-7}$ kg/s ($\triangle$) and $\alpha = 10kT$ with $\xi_e = 5\cdot10^{-9}$ kg/s ($\triangledown$) are referred to as model fluids 1 (MF1) and 2 (MF2), respectively. In the left column are shown the viscosities η_{α,ξ_e} obtained from simulations over a wide range of shear rates $\dot{\gamma}$. The same data are plotted in the right column, rescaled as $\eta^*_\alpha = (\xi_0/\xi_e)\eta_{\alpha,\xi_e}$ versus $\dot{\gamma}^* = (\xi_0/\xi_e)\dot{\gamma}$, where the black dashed lines are fits with Eq. (3.11).

chains. Shear viscosities were calculated according to

$$\eta_{\alpha,\xi_e}(\dot\gamma) = \frac{S^{xy}_{\alpha,\xi_e}(\dot\gamma)}{\dot\gamma}, \tag{3.7}$$

where $S^{xy}_{\alpha,\xi_e}(\dot\gamma)$ is the steady-state xy-component of the shear stress tensor at shear rate $\dot\gamma$ for a given combination of α and ξ_e. In the left column of Fig. 3.2 we plot flow curves for a range of entanglement frictions and three values of α. In the range of shear rates analyzed, the overall value of the shear viscosity increases with increasing ξ_e, and the point where the liquid starts to shear-thin shifts to lower shear rates.

By assuming that $n_{ij} = n_0(r_{ij})$ at all times, i.e., in the limit of vanishing transient forces, one readily infers from Eq. (3.5) that all simulations sharing a common value for the product of shear rate and friction coefficient, $\dot\gamma\xi_e$, will sample the same sequence of configurations when started with the same initial configuration. In physical terms, because the dynamics is slowed down proportionally to ξ_e, the shear rate must be slowed down by the same factor in order to run through the same sequence of configurations – albeit at a different pace – as with some reference friction ξ_0. Consequently, the shear stresses in both cases must be identical,

$$S^{xy}_{\alpha,\xi_e}(\dot\gamma\xi_0/\xi_e) = S^{xy}_{\alpha,\xi_0}(\dot\gamma). \tag{3.8}$$

Using Eq. (3.7) we then find

$$\frac{\xi_0}{\xi_e}\eta_{\alpha,\xi_e}(\dot\gamma\xi_0/\xi_e) = \eta_{\alpha,\xi_0}(\dot\gamma). \tag{3.9}$$

In the right column of Fig. 3.2 we have therefore plotted the scaled viscosity $\eta^*_\alpha = (\xi_0/\xi_e)\eta_{\alpha,\xi_e}$ as a function of the scaled shear rate $\dot\gamma^* = (\xi_0/\xi_e)\dot\gamma$, based on the reference value $\xi_0 = 1.6\times10^{-7}$ kg/s. Even though transient forces do play a role in these cases, we obtain good agreement with the above scaling law for all three values of α.

Having obtained these scaled curves, we observe that they can be made to coincide by multiplying all viscosities by $(\alpha_0/\alpha)^{2/3}$, with α_0 being some reference value for α. This is demonstrated in Fig. 3.3, where $\eta^* = (\alpha_0/\alpha)^{2/3}\eta^*_\alpha$ is plotted versus $\dot\gamma^*$, using $\alpha_0 = 1kT$. The scaling is seen to work well for all three values of α, although at low shear rates a clear deviation occurs for $\alpha = 10kT$. To be definite, we mention that these considerations together lead to the master curve

$$\eta_{\alpha,\xi_e}(\dot\gamma) = \left(\frac{\alpha}{\alpha_0}\right)^{2/3}\frac{\xi_e}{\xi_0}\eta^*(\dot\gamma\xi_e/\xi_0), \tag{3.10}$$

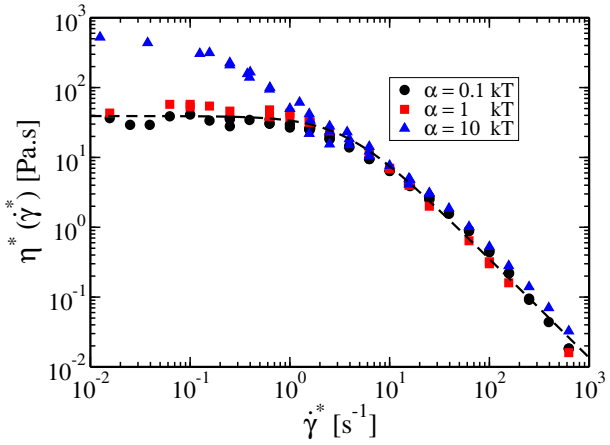

Figure 3.3: Shear viscosity curves plotted after applying Eq. (3.10) to the simulation data showed on the left side of Fig. 3.2. The viscosity for each α includes all the points plotted in Fig. 3.2 at various ξ_e. The dashed line is plotted by using Eq. (3.11).

where the function η^* may be fitted with the Cross model [19],

$$\eta^*(x) = \frac{\eta_0}{1+(\tau_s x)^{\varepsilon}}. \tag{3.11}$$

The collective simulation data are well fitted with $\eta_0 = 36\,\mathrm{Pa\,s}$, $\tau_s = 0.25\,\mathrm{s}$ and $\varepsilon = 1.4$, as illustrated in Fig. 3.2 (right column) and Fig. 3.3.

3.3.2 Critical shear rates

Having obtained a general expression for the shear viscosity for a wide range of values of α and ξ_e, we now investigate the effect of these parameters on the alignment of colloids. The colloids obey a Brownian equation of motion, akin to Eq. (3.5), with explicit interactions due to the polymeric chains, and a constant friction coefficient ξ_c accounting for the friction and random interactions with the flowing solvent. The interactions between the colloids and the fluid particles, ϕ_{cp}, and between the colloids themselves, ϕ_{cc}, are purely repulsive and are given by

$$\phi_{cp}(r) = 100\, e^{-2(r+R_{col}-R_g)^2}, \tag{3.12}$$

$$\phi_{cc}(r) = 4\left(\frac{0.1}{r-2R_{col}}\right)^8, \tag{3.13}$$

where r is the center of mass separation and $R_{col} = R_g = 40\,\mathrm{nm}$ is the radius of the colloids. The colloid-colloid potential ϕ_{cc} is represented by a relatively hard potential, acting at short distances to prevent colloids from overlapping, but soft enough to allow sufficiently large time-steps. The considerably softer exponential form of the colloid-particle potential ϕ_{cp} allows the center of mass of a RaPiD particle to approach colloids to distances smaller than R_{col}, representing the situation where the polymer particle is enlacing the colloid. This form of the potential has been suggested by inverting structure information from sphere-polymer simulations [11].

In order to test for colloidal alignment, the stability of an initially flow-aligned chain of 8 colloids was monitored for a range of fluid parameters and shear rates. The colloidal strings were surrounded by 3892 RaPiD particles, in rectangular boxes with dimensions $20R_g \times 8R_g \times 7R_g$. Periodic boundary conditions effectively turn the row of colloids into an infinitely long string; the intercolloidal spacing of $0.5R_g$, corresponding to a distance of $2.5R_g$ between the centers of two trailing colloids, is comparable to the gap between colloids in strings of finite length, as studied in our preceding simulations [102]. Figure 3.4 shows the simulation results as markers superimposed on the flow curves calculated using Eq. (3.11) in combination with Eq. (3.10). To emphasize a remarkable result of these simulations, the vertical positions of the markers do not represent measured viscosities, as in Fig. 3.2, but the nominal viscosities from Eq. (3.11) and Eq. (3.10). Circles refer to simulations during which the preconstructed chains remained stable, while crosses refer to those where this was not the case. The results suggest that with each friction coefficient ξ_e, but independent of α, a critical viscosity η_c exists below which chains are stable and above which chains are unstable. The critical viscosity, in the range of values studied, is roughly proportional to the friction coefficient,

$$\eta_c = \bar{\eta}\,\frac{\xi_e}{\xi_0}, \tag{3.14}$$

with $\bar{\eta} = 1.4\,\mathrm{Pa\,s}$. Using Eqs. (3.10) and (3.11), we then calculate the corresponding critical shear rate to be

$$\dot{\gamma}_c = \frac{\xi_0}{\xi_e}\frac{1}{\tau_s}\left\{\left(\frac{\alpha}{\alpha_0}\right)^{2/3}\frac{\eta_0}{\bar{\eta}} - 1\right\}^{1/1.4}. \tag{3.15}$$

In all cases studied here, the second term between the curly brackets may be ignored, which yields that $\dot{\gamma}_c$ is inversely proportional with ξ_e and scales approximately with $\alpha^{1/2}$.

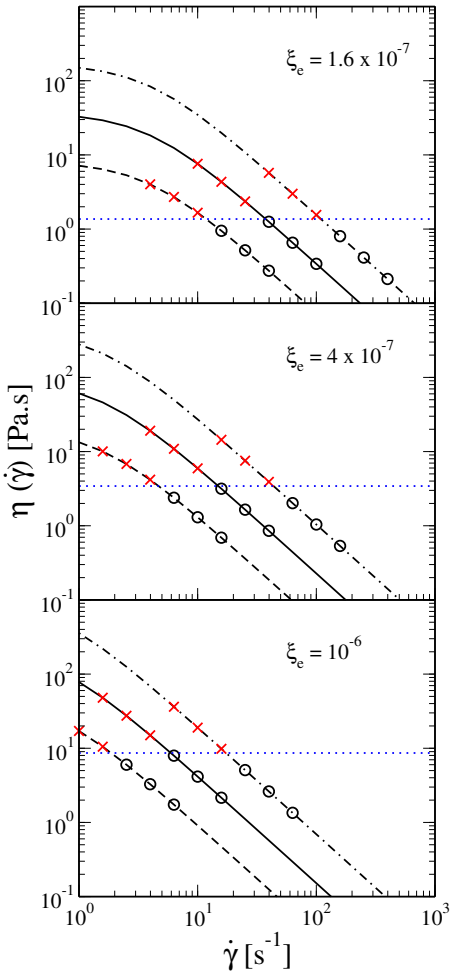

Figure 3.4: Viscosity curves at three different entanglement friction parameters ξ_e [kg/s]. In each subplot, the dashed line represent the viscosity for $\alpha = 0.1kT$, the central solid line corresponds to $\alpha = 1kT$ and the dash-dotted line is obtained with $\alpha = 10kT$. The markers, which for clarity are positioned on the theoretical curves, indicate the behavior of dissolved colloids in these nine fluids at the indicated shear rates. Black circles (○) represent conditions in which initially flow-aligned chains of 8 colloids remained intact during simulations of 20 s, and red crosses (×) denote chains that disintegrated during the simulations. The blue dotted lines highlight the friction-dependent critical viscosity η_c.

Let us now briefly go back to the simulations in our preceding work [102]. There we considered fluids which roughly mimick two viscoelastic fluids used previously to study chaining of colloids under shear. In agreement with experiments [92], we found chaining in one of the fluids and no chaining in the other. With our new results we may now estimate the critical shear rates for chain formation in both fluids. For the wormlike micellar fluid we find $\dot{\gamma}_c \approx 3\,\mathrm{s}^{-1}$, in good agreement with the value reported in our previous work. For the polymer solution we find $\dot{\gamma}_c \approx 4 \cdot 10^3\,\mathrm{s}^{-1}$, which is beyond the shear rates tested by us and also beyond those tested experimentally. In this context, it is imperative to notice that many shear-thinning fluids are known to exhibit Newtonian behavior at extreme shear rates, both low and high. Therefore, it could well be the case that in practice it proves impossible to reach the estimated critical viscosity η_c of this polymer solution.

3.4 Forces and density distributions

Since randomly distributed colloids spontaneously line up in chains during extensive shearing, but distribute homogeneously under zero and low shear, there likely exist effective colloid-colloid attractions that depend substantially on the applied shear flow. In this section we will investigate the forces acting on two spheres that move with the fluid, but do so at a constant distance from each other. Besides keeping constant the distance between the colloids, we also kept the orientation of the connecting vector parallel to the flow direction. This was done by displacing both colloids at every time step by

$$d\mathbf{R} = \frac{1}{2\xi_c}(\mathbf{F}_1 + \mathbf{F}_2)dt + V(y)\hat{\mathbf{e}}_x dt. \tag{3.16}$$

This displacement is simply the center of mass motion for two colloids experiencing fluid forces $\mathbf{F}_1$ and $\mathbf{F}_2$, respectively, since the additional distance constraint introduces an internal force which from classical mechanics is known not to alter the center of mass motion. Simulations without the orientation constraint show that the pair tends to stay aligned with the flow; for clarity of the ensuing results, we have therefore here disallowed rotations of the connecting vector. Finally, y is the common value of the coordinates of both colloids along the gradient direction, $V(y)$ is the average flow velocity at this height, and $\hat{\mathbf{e}}_x$ is the unit vector along the flow direction.

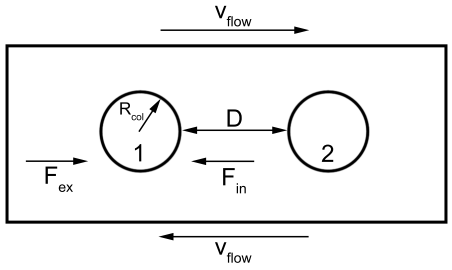

Figure 3.5: Sketch of the simulation box used to compute the effective force between two fixed colloids of radius R_{col} separated by a intersurface distance D. The direction of the flow velocity v_{flow} is indicated at the top and bottom of the picture. For colloid 1, F_{ex} is the total inward pointing sum of all forces exerted on that colloid by particles to the left of its center of mass, and F_{in} is the equivalent outward pointing sum of forces due to particles to the right of its center of mass; mirrored definitions apply for colloid 2, i.e. left and right are exchanged. The sketch is not to scale.

In this section we study the changes of the effective interaction F_{12} between the two colloids when the shear rate is varied over a range of values that includes the critical shear rate $\dot{\gamma}_c$. The effective interaction is calculated as

$$F_{12} = (\mathbf{F}_2 - \mathbf{F}_1) \cdot \hat{\mathbf{e}}_x, \tag{3.17}$$

with negative F_{12} corresponding to attraction and positive values denoting repulsion. In order to do this analysis in a comfortable way, we have chosen a model fluid (MF1) with a relatively low critical viscosity, $\dot{\gamma}_c \approx 3\,\mathrm{s}^{-1}$. Further information on this fluid may be found in table 3.1. We will denote by D the closest distance between the surfaces of the two colloids (see Fig. 3.5).

In Fig. 3.6 (a) we have plotted F_{12} for our model fluid as a function of D for various shear rates. The drawn lines are smooth representations of the measured forces, which next have been used to calculate the effective potential energies depicted in Fig. 3.6 (b). Note that whereas the direct force between the two colloids has been omitted from the force plotted in Fig. 3.6 (a), which thus highlights the fluid contribution to the effective force, the corresponding potential has been included in the effective potential shown in Fig. 3.6 (b). First of all, we notice that the potential energy when $\dot{\gamma} = 0$ has the usual form and meaning of a potential

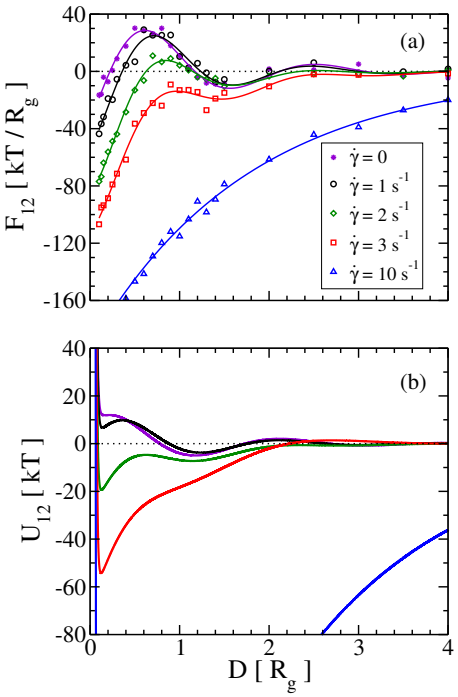

Figure 3.6: (a) Effective force between two colloids dispersed in MF1, as a function of the surface distance D for various shear rates, with positive (negative) values denoting repulsion (attraction). (b) The corresponding effective interaction potentials are obtained by integrating F_{12} over D, with U_{12} converging to zero for large separations. Direct colloid-colloid interactions ϕ_{cc}, which are absent in the fluid-induced F_{12} forces, have been included in U_{12}.

of mean force; the oscillations reflect similar oscillations in the radial distribution function. When two colloids approach each other, for surface distances D between $\sim 2R_g$ and $\sim 1R_g$ they will effectively attract each other, but on further approach they start to repel until finally the direct interaction between them prohibits further approach. On imposing shear flow, this picture changes such that the first repulsive maximum of the effective forces diminishes and gradually shifts to larger values of D. For shear rates close to $\dot{\gamma}_c$ the maximum effective force drops below zero and the interaction becomes attractive over the whole range of separations. On increasing the shear rate even further very strong attractions develop, with corresponding potentials that are very similar to depletion potentials often seen in colloid-polymer mixtures

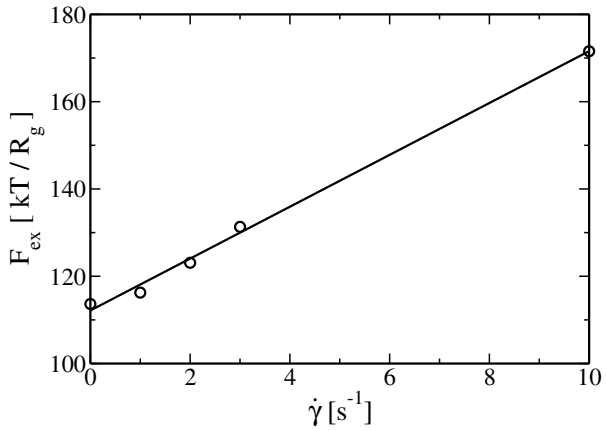

Figure 3.7: The external force F_{ex} plotted as a function of shear rate for two colloids in model fluid 1 (○). The external force F_{ex}, as defined in Fig. 3.5, measures the average force by which particles to the left (right) of the center of mass of colloid 1 (2) drive that colloid to the other colloid.

with (entropic) repulsions between colloids and polymers [114].

The effective forces acting on the colloids arise from an imbalance in the forces exerted by the particles in the region between the colloids and those exerted by the particles in the region external to the colloids. In case the resulting forces from these two regions sum to zero, there are no effective interactions between the colloids. To establish how the forces in the central and external regions change with shear rate and distance, we have calculated the average total forces applied by the external (F_{ex}) and internal (F_{in}) regions, following the definition explained in the caption of Fig. 3.5. We found that, for all shear rates, the force F_{ex} exerted by the particles in the outer regions was independent of the separation between the two colloids. This finding implies that, for a given shear rate, the variation of the effective force F_{12} with colloidal separation, as plotted in Fig. 3.6 (a), basically reflects the variation of F_{in} with surface distance. The external force steadily increased with increasing shear rate, as can be seen in Fig. 3.7. Since F_{ex} measures the average total inward pointing force on colloid 1 (2) due to particles to the left (right) of that colloid, its increasing magnitude will give rise – if not counteracted by a similar increase of F_{in} – to a flow-induced attractive force between the colloids.

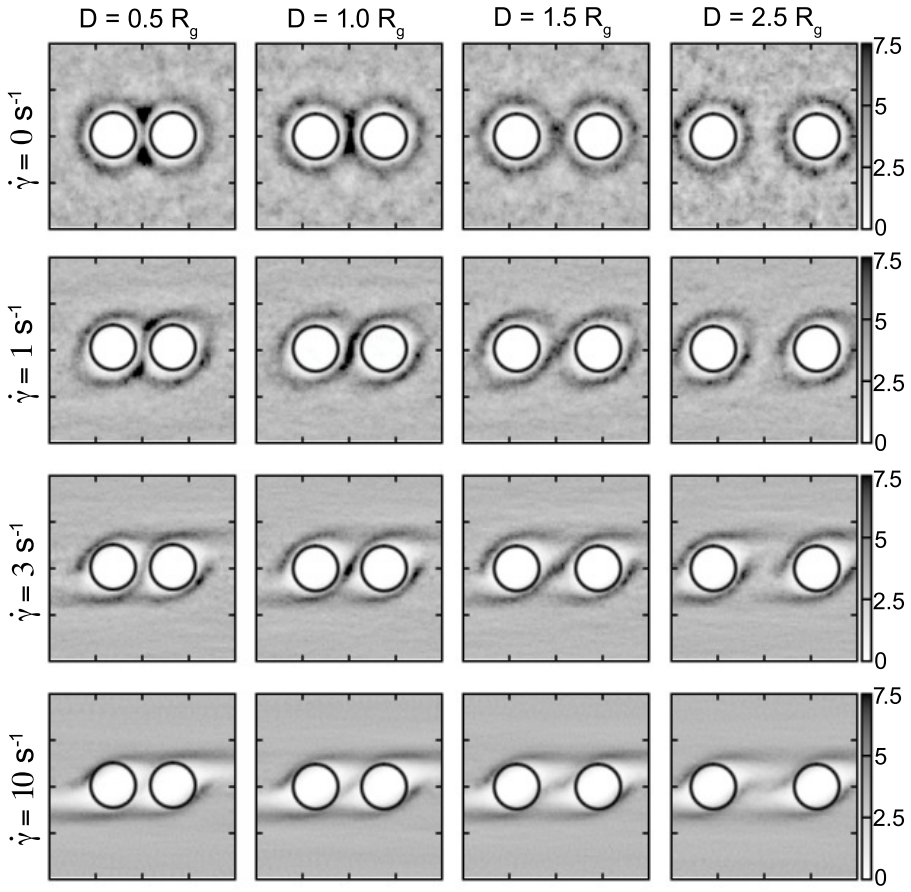

Figure 3.8: Average density distributions surrounding two colloids in model fluid 1, for the colloidal surface separations D denoted at the top and the shear rates indicated on the left. Each subplot represents the density within a volume of $8R_g \times 8R_g \times 2R_g$, projected on the flow-gradient (xy) plane. The gray scale on the right side quantifies the density, in particles per R_g^3.

The strong dependence on shear rate of the forces on and between the colloids strongly suggests that these force variations are related to flow induced changes in the particle density around the colloids. We therefore calculated the density of particles projected on the flow-gradient plane through the centers of mass of both colloids, delimited in the vorticity direction to projection distances of less than $1R_g$. The results for 4 shear rates and 4 separation distances are collected in Fig. 3.8. The case of one or two colloids in a quiescent fluid, i.e. $\dot{\gamma} = 0$, has already been studied by other investigators. For example, Doxastakis *et al.* [27,28] observed in Monte Carlo simulations to investigate the distribution of polymer chains near a single and between two spherical colloids, that with increasing polymer density the chains accumulate at the surfaces of the colloids due to packing effects. These observations were confirmed by Li and Wu [67] and Bymaster *et al.* [15], applying density functional theory. Since our system is far beyond the semi-dilute regime, at nearly 15 times the critical overlap concentration, larger concentrations of chains around the colloids are expected. This is indeed what we observe in the first row of Fig. 3.8 at large separation distance of the colloids. The reason for the accumulation of particles near colloids in the present model may easily be understood with reference to the various ingredients of the model described in Section 3.2. In a homogeneous distribution, a particle i close to a colloid will experience a polymeric volume fraction ϕ_i less than average, simply because part of its surrounding volume is excluded for neighboring polymers, leading to a Flory-Huggins free energy $a^p(\phi_i)$ less than average. Consequently, additional particles are attracted to this region and the local volume fraction rises until the chemical potential is constant throughout the entire simulation box. This phenomenon may be considered to arise from an effective attraction between the particles and the colloids. Next, when two colloids are brought close together, the effective colloid-particle attraction gives rise to colloid-colloid attraction as soon as both colloids are within the reach of particles in the internal region, i.e. when the surface separation between the colloids is less than twice the cutoff radius of $\omega(r)$ in Fig. 3.1. In practice, as is seen from Fig. 3.6, the effect gives rise to a weak attraction for intercolloidal spacings D of about $1R_g$ to $2R_g$. At closer approaches, for distances smaller than about $1R_g$, the particle density between the colloids becomes so large that they effectively start to repel the colloids.

The second row in Fig. 3.8 shows densities of particles near colloids when a small shear rate of $1\,\mathrm{s}^{-1}$ is applied. It is seen that the condensates surrounding the colloids are slightly

deformed by the shear flow. This effect becomes stronger when the shear rate is increased to $3\,\mathrm{s}^{-1}$, which is slightly above the critical shear rate for colloidal chain formation in MF1. Particles at the two upstream sides of a colloid are pushed toward the colloid, while those at the two downstream sides of a colloid are torn off from the colloid's surface. This gives rise to a skew symmetric distribution of particles around a single colloid, as seen in Fig. 3.8 for the largest D, and for smaller separations reduces the particle density between two colloids to below the density in the bulk. This depletion of particles in the internal region is the cause of a diminished pressure, i.e., a reduction of F_{in} relative to F_{ex}, which gives rise to the main effective attraction force between the colloids. Increasing the shear rate even further, to $\dot{\gamma} = 10\,\mathrm{s}^{-1}$ in the bottom row of Fig. 3.8, enhances these effects and creates a strongly depleted region between two flow-aligned colloids.

An important conclusion, distilled from the above observations, is that the conservative and restoring (transient) forces between the particles, with increasing shear rates, are finally too weak to suppress the formation of 'depletion wakes' at both downstream surfaces of a colloid in a shear flow. Nor is the diffusion rate high enough for particles to replenish the wakes swiftly; the particles that are flowing around a colloid continue to travel with the flow for some time, and hence traverse a considerable distance, before the wake is finally hemmed in by the slow inward diffusion. Symmetry implies that the total force resulting from the two depletion wakes is zero for a single colloid in a sheared polymeric solution. This balance is disturbed when a colloid enters the wake of another colloid, in which case an asymmetry in the forces – basically, the difference between F_{in} and F_{ex} – will carry the particles toward each other. We note that it is much more difficult to form similar depletion wakes in regular fluids, like water, because of the far stronger interactions between the molecules and the correspondingly much higher pressures and bulk compressibilities. This, of course, does not prevent polymeric chains dissolved in these fluids from forming wakes, with the resulting imbalance in the osmotic pressure causing the formation of colloidal strings.

We have checked the role of wakes in colloidal alignment in a large number of different solvents with dynamical parameters in the range investigated in the previous section, simply by visual inspection of the density distributions around the colloids. In each case, the colloids showed trailing wakes under conditions favouring alignment, while such wakes were absent below the critical shear rate of the specific fluid. In a few cases we calculated forces F_{12}

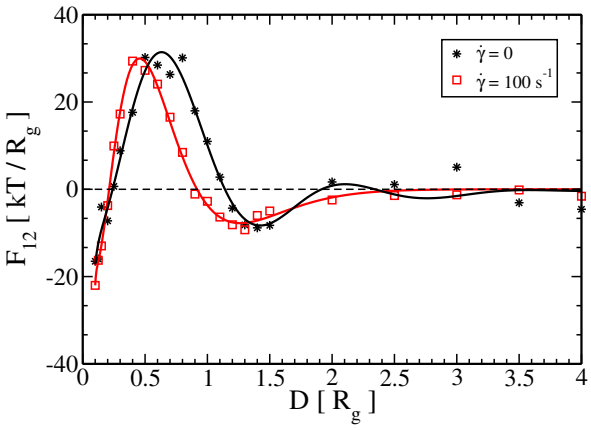

Figure 3.9: Effective force between two colloids in model fluid 2, as a function of their surface distance. Both model liquids are thermodynamically identical by construction, hence the force curve in the quiescent fluid is the same as that for MF1 in Fig. 3.6. The pair force remains largely repulsive at the high shear rate of $\dot{\gamma} = 100\,\mathrm{s}^{-1}$*, and consequently the colloids will not align.*

and compared the results with those for MF1. Since from a thermodynamic point of view all liquids are the same, their force curves at zero shear rate are all equal. With non-zero shear rates we found results very similar to those in Fig. 3.6. We found that curves with the same value for $\dot{\gamma}/\dot{\gamma}_c$ are roughly identical. In one extreme case (MF2 in Table 3.1) with $\dot{\gamma}_c \approx 4 \cdot 10^3\,\mathrm{s}^{-1}$ we checked that even at a shear rate as high as $100\,\mathrm{s}^{-1}$ the force curve is very close to that for quiescent fluid (see Fig. 3.9). It is not easy to disentangle the influences of ξ_e and α from each other, since both affect all dynamical properties of the fluids. For example in going from MF1 to MF2 the friction goes down by a factor of one hundred, yet the diffusion goes down by a factor of ten (not shown) due to an increase of α by a factor of one hundred. Moreover it is not evident that the bulk diffusion coefficient is relevant for diffusion of particles from the particle rich part of the system into the particle lean wake. Let us therefore end with just one general observation. Entanglements between chains have the tendency to keep the system homogeneous and strongly resist the formation of wakes. This effect increases strongly with increasing α.

3.5 Summary and conclusions

We have investigated the origin of flow induced alignment of colloids dispersed in viscoelastic liquids. To this end we have first characterized, from a rheological point of view, a large class of viscoelastic liquids modeled with the RaPiD simulation method. The thermodynamic state of all liquids was taken to be the same, while their rheological properties were varied by varying two parameters in the simulation model. We covered a large area of our parameter space between two extreme cases that we previously tuned to represent two experimental model fluids used to study colloidal alignment. We found that with each fluid a critical shear rate could be attributed below which dissolved colloids do not align, and above which they do align in chains.

We next calculated the effective forces between two colloids placed at various distances along the flow direction in a sheared liquid. Since our viscoelastic liquids themselves are solutions of complex polymers, the force curve at zero shear rate has all the characteristics of forces between colloids in polymer solutions. With decreasing distances between the two colloids their polymer mediated interactions become first weakly attractive, next repulsive and finally attractive again. The repulsions occur when the two adsorbed polymer layers start to repel each other while the attractions result from overlap of the two depletion zones. With increasing shear rates the repulsion becomes weaker and the depletion attraction becomes stronger. At the critical shear rate the repulsion has disappeared altogether.

In order to gain further insights we investigated the distribution of polymers around the colloids. We found that with increasing shear rates increasingly more prominent polymer lean wakes appear on the down stream sides of the colloids, while polymers collect at the upstream sides. At large colloid separation the polymer distribution around each colloid still has inversion symmetry, leading to zero forces on the colloids. At shorter distances, and sufficiently high shear rates, one of the down stream wakes of each colloid interferes with one of the upstream polymer heaps of the other colloid, thereby perturbing the symmetry, which leads to effective attraction between the colloids. One of the consequences of this mechanism is that with larger colloids (relative to the radius of gyration of the polymer) the attractive forces become substantial only when the colloids are very close together, probably even touching.

One of the ingredients of the RaPiD simulation model is a correction to the average,

thermodynamic, force between two polymers when their degree of entangling is not equal to its value in equilibrium, i.e., when the polymers have been kept in position, in a quiescent fluid, for a long time. These forces have the tendency to push the particles to distances where the actual degree of entangling is equal to its equilibrium value. This leads to strong resilience to the occurrence of concentration gradients, thereby raising the critical shear rate for colloidal alignment.

4 Alignment and segregation of bidisperse colloids in a shear-thinning viscoelastic fluid under shear flow

Computer simulations are presented of colloids, bidisperse in size, suspended in a shear-thinning viscoelastic fluid with the flow characteristics of a surfactant solution. The worm-like micelles are modeled in Responsive Particle Dynamics (RaPiD) as single soft particles obeying a generalized Brownian equation of motion including transient forces that effectively account for the entanglements of the polymeric chains. The colloids mix homogeneously in the quiescent fluid, but in a shear flow they string together and form colloidal trains. Besides alignment, we also observe simultaneous segregation of the colloids by size. Experimental studies have reported on separation by size occurring near the walls of the rheometer, while in the current study the colloids segregate in the bulk of the fluid.

4.1 Introduction

Colloids dissolved in viscoelastic fluids display intriguing behavior, markedly different from that shown by their counterparts in simple Newtonian liquids. For instance, colloids in shear-thinning polymer solutions are known to migrate under shear to the walls of the rheometer, where they subsequently order into shear-aligned strings [82, 93, 96]. Colloids in a shear-thinning solution of worm-like micelles have been reported to form trains in the bulk of the sheared fluid [92]. The physical origins of the alignment are still poorly understood, and several explanations have been put forward in the literature [53, 103, 122]. Two experiments

using polymeric solvents showed that colloids, bidisperse in size, tend to segregate by size into trains of small colloids and trains of large colloids. In the experiments executed by Pätzold and presented by Giesekus [38], the slit of the rheometer was hardly wider than the diameter of the largest colloid and hence wall effects may be expected to have played an important role. This also appears to be the case in the experiments by Lyon et al. [72].

Computer simulations to help understand the physical process driving colloids in sheared viscoelastic fluids have been developed by several groups [4, 20, 34, 43, 54, 94]. These simulations have typically been restricted to two dimensions, or to a few colloids when run in three dimensions, because of the heavy computational demands of numerical flow solvers. We have recently developed and validated Responsive Particle Dynamics (RaPiD) as an efficient method to simulate viscoelastic fluids [14, 63, 109, 117], with the capability of handling a hundred colloids in three dimensions when run on a regular desktop computer. By tuning the fluid parameters to the flow characteristics of two shear-thinning experimental fluids, we found that the simulations reproduced shear-induced colloidal alignment in the bulk for one fluid but not for the other, in perfect agreement with experiments [102]. Here we present RaPiD simulations on the ordering of bidisperse colloids in a sheared viscoelastic fluid, and show that size segregation may also occur in the bulk of the fluid.

4.2 Simulation model

In order to reach the long time and length scales required for colloidal alignment, the flexible polymeric chains of the viscoelastic fluid are coarse-grained in Responsive Particle Dynamics (RaPiD) [14, 87, 117] to single particles obeying Brownian dynamics with transient forces. We here briefly summarize the features of the model, referring the reader to [63, 102] for a deeper motivation and technical details. Previous applications of RaPiD, besides colloids alignment in sheared viscoelastic fluids [102], include polymer melts [63], solutions of polymeric core-shell colloids [115], telechelic polymer networks [109], concentrated solutions of star polymers [90] and glue [88, 89].

The conservative forces on the particles are derived from the potential of mean force Φ_C, which is the free energy governing the distribution of the polymeric centers of mass. In

equilibrium, the probability distribution of the positions r of the N particles is given by

$$P_{eq}(r) \propto \exp[-\beta\Phi_C(r)], \tag{4.1}$$

where $\beta = 1/kT$ with Boltzmann's constant k and temperature $T = 300\,\mathrm{K}$. We use a free energy Φ_C based on the Flory-Huggins theory for polymeric chains in an athermal solvent [36, 51], expressed as a sum of single particle contributions that depend on the local density around the particle. This approach is explained in detail in our previous study [102].

The transient forces in the RaPiD model account for correlations between the retained and eliminated degrees of freedom of the polymeric chains. Since the polymeric chains are coarse grained as single particles, the simulation model does not automatically include the explicit entanglements of polymeric chains that are deemed important for the dynamic behavior of the fluid. To reinstate entanglement effects, we therefore introduce a new variable n_{ij} with every pair of particles i and j to represent their degree of entanglement. The corresponding force is calculated as the deviation of this entanglement number from its distance dependent equilibrium value $n_0(r_{ij})$, which is modeled as a quadratic function decaying from $n_0(0) = 1$ to $n_0(r_c) = 0$ with $r_c = 2.5R_g$ the cut-off radius. The transient potential is then written as

$$\Phi_t(r,n) = \frac{1}{2}\alpha\sum_{ij}(n_{ij} - n_0(r_{ij}))^2, \tag{4.2}$$

with $\alpha = 0.1kT$ representing the strength of the entanglements. The quadratic form of $\Phi_t(r,n)$ ensures that the probability density of Eq. (4.1) is recovered as the equilibrium state. The propagation of the entanglements numbers, over a time step dt on the Smoluchowski time scale, is given by

$$dn_{ij} = -\frac{1}{\xi_n}\frac{\partial\Phi_t}{\partial n_{ij}}dt + \Theta_{ij}(t)\sqrt{\frac{2kT\,dt}{\xi_n}}, \tag{4.3}$$

where $\xi_n = 20kTs$ is a friction coefficient, and $\Theta_{ij}(t)$ is a time-dependent random Markovian scalar with zero mean, unit variance, and without correlation across different particle pairs.

The displacement of fluid particle i over a time step dt reads as

$$d\mathbf{r}_i = -\frac{1}{\xi_i}\left(\nabla_i\Phi_C + \nabla_i\Phi_t\right)dt + \nabla_i\left(\frac{kT}{\xi_i}\right)dt + \mathbf{\Theta}_i(t)\sqrt{\frac{2kT\,dt}{\xi_i}} + V(y_i)\hat{\mathbf{e}}_x dt. \tag{4.4}$$

On the Smoluchowski time scale, the conservative and transient forces in the first term on the right hand side are balanced by friction, which naturally arises in a Brownian dynamics

algorithm from the eliminated degrees of freedom of the system. In RaPiD, the friction parameter is expressed as

$$\xi_i = \xi_0 + \xi_e \sum_{j \neq i} \sqrt{n_{ij} n_0(r_{ij})}, \tag{4.5}$$

where $\xi_0 = 5 \times 10^{-9}$ kg/s is the background friction stemming from the solvent and $\xi_e = 7 \times 10^{-7}$ kg/s is the friction per 'entanglement' of particle i. This non-constant friction parameter gives rise to spurious diffusion, which is corrected for by the second term on the right hand side in Eq. (4.4) [14]. The third term describes Brownian displacements of the particles, where $\boldsymbol{\Theta_i}(t)$ is a random Markovian vector with unit variance, zero mean, no memory and uncorrelated across particles. Finally, the last term in Eq. (4.4) represents motion with the flow. In this case, Lees-Edwards sliding boundary conditions maintain a shear flow in the x direction with an average velocity gradient $\dot{\gamma}$ in the y direction. The velocity profile $V(y_i)$ is evaluated every step, following the procedure outlined in [109,116], and allows for non-linear profiles.

4.3 Systems

We have recently developed a RaPiD model representing a solution of worm-like micelles, based on an experimental solution of cetylpyridinium-chloride (CPyCl) and sodiumsalicylate (NaSal) in salt (NaCl) water [102]. For simplicity, the very wide size distribution of worm-like micelles was replaced by a uniform radius of gyration of $R_g = 40$ nm, and the number density was fixed at 3.5 particles per R_g^3. The most relevant simulation parameters are those pertaining to the particle dynamics, α, ξ_e and $\tau = \xi_n/\alpha$. These were tuned to reproduce the experimental storage $G'(\omega)$ and loss moduli $G''(\omega)$ [107], which show the characteristics of a Maxwell fluid with a single relaxation time [29, 66]. Through an iterative process, we recovered a good agreement with the experimental results, as shown in [102]. The zero shear viscosity η_0 and the viscosity under rate $\eta(\dot{\gamma})$ are also in reasonable concordance with experiments [107], reproducing the fluid's shear-thinning characteristic.

Here we report simulations of mixtures of spherical colloids with two different radii dissolved in the aforementioned fluid. The small colloids have a radius of $R^s_{\mathrm{col}} = R_g$, the large colloids measure $R^l_{\mathrm{col}} = 1.5\,R_g$. We note that these colloids are about three order of magnitude

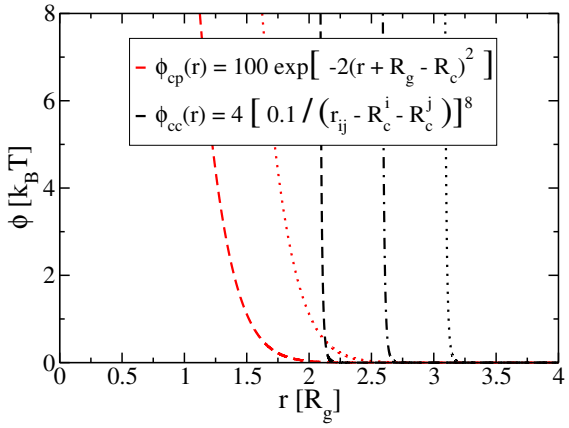

Figure 4.1: The colloid-colloid (black lines) and colloid-particle (red lines) interaction potentials as function of the distance r. Dotted lines refer to the small colloids, $R^s_{\mathrm{col}} = 1R_g$, dashed lines to the large colloids, $R^l_{\mathrm{col}} = 1.5R_g$, and dash-dotted lines to a large-small combination.

smaller than the 10 μm to 75 μm colloids used in the experiments by Giesekus and Lyon *et al.* [38, 72]. Due to computational limitations, however, it is not feasible to simulate colloids that are many times larger than the worm-like micelles. Because of this relatively small size, the Peclet number $\mathrm{Pe} = 6\pi R^3_{col}\dot{\gamma}\eta(\dot{\gamma})/kT$ peaks at a value of about 10 in our simulations, as apposed to $\mathcal{O}(10^6)$ in the experiments. As a result, Brownian displacements of the colloids will be more important in the simulations than in the experiments. From our earlier simulations, however, we do not expect the enhanced thermal motions to change the steady state configuration qualitatively.

The interaction between two colloids i and j is described by a relatively hard potential, scaling with the 8$^{\mathrm{th}}$ power of the surface-to-surface distance $D = r_{ij} - R^i_{\mathrm{col}} - R^j_{\mathrm{col}}$, as illustrated in Fig. 4.1. Based on the work of Bolhuis and Louis [11], the colloid-particle interaction is modeled by a much softer Gaussian potential. A particle, i.e. the center of mass of a worm-like micelle, is thus allowed to approach a colloid to distances close to or even smaller than R_{col} – this represents the ability of long flexible chains to enlace a colloidal particle, such that its center of mass is located inside the colloid. Similarly to the fluid particles, the displacements of the colloids over a time step dt are described by the Brownian dynamics

propagator described in Eq. (4.4). In this case, however, the entanglement forces are absent since colloids can not entangle between themselves nor with fluid particles. Furthermore, the friction coefficient of the colloids is calculated using Stokes's law, $\xi_{\mathrm{col}} = 6\pi\eta(\dot{\gamma})R_{\mathrm{col}}$, and is held constant during a simulation.

All simulations are performed at the same chemical potential for the fluid particles. The appropriate adjustment of the number of particles with the insertion of a colloid is not readily determined from the interaction potentials. In stead, we performed simulations of a system divided by semi-permeable walls into sections with and without colloids; a volume rescaling algorithm was used to equilibrate the number density of the latter section to the $\rho_{\mathrm{ref}} = 3.5/R_g^3$ of the reference fluid, and thereby establishes the desired chemical potential, while the volume V_{disp} of the dispersion phase was kept fixed [102]. The apparent volume v^l_{app} and v^s_{app} of the large and small colloids, respectively, were then established by evaluating the relation for the number of particles in the colloidal phase, $N_p^{\mathrm{disp}} = \rho_{\mathrm{ref}}\left(V_{\mathrm{disp}} - N^s_{\mathrm{col}}v^s_{\mathrm{app}} - N^l_{\mathrm{col}}v^l_{\mathrm{app}}\right)$, for various numbers N^l_{col} and N^s_{col} of large and small particles. The apparent volumes are smaller than the nominal volumes $\frac{4}{3}\pi R^3_{\mathrm{col}}$, indicating that the particles accumulate around the colloids despite their purely repulsive interaction, see Fig. 4.1. The effective attraction arises from the Flory-Huggins interactions between the particles, with the increased density near the colloidal surface compensating for the loss of neighbors by steric hindrance. Density plots illustrating the condensation on the colloidal surface are presented in [101].

4.4 Results

In a preceding study we established that the current shear-thinning viscoelastic fluid stimulates the formation of strings of the small colloids, provided the applied shear rate exceeds a critical value of about $3\,\mathrm{s}^{-1}$ [101, 102]. We will now investigate the behavior of bidisperse colloids in this fluid. The colloids, 44 small ones and 30 large ones, were placed in a rectangular simulation box measuring $37.5R_g \times 25.5R_g \times 10R_g$ ($0.6\,\mu\mathrm{m}^3$), along with 32 693 fluid particles. The colloidal volume fractions of $\varphi^s \sim 2\%$ and $\varphi^l \sim 4\%$ for the small and large colloids, respectively, are comparable to experimental values. To facilitate the formation of strings, and to simplify their visualization in Visual Molecular Dynamics (VMD, [52]), the colloids were initially distributed over the plane formed by the shear velocity and the velocity-

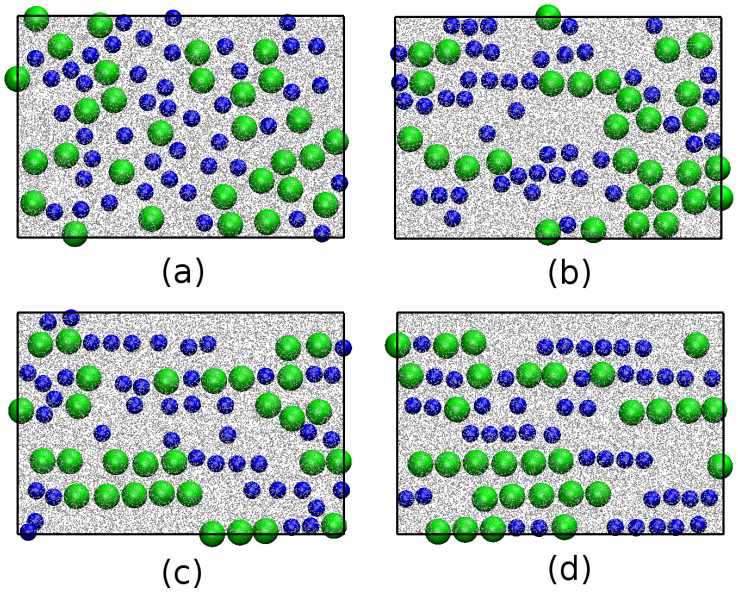

Figure 4.2: Snapshots of a simulation with 44 small colloids (blue spheres) and 30 large colloids (green spheres) in a sheared viscoelastic solvent modeled by RaPiD particles (grey dots). The flow velocity is along the horizontal x direction, the velocity gradient along the vertical y direction. All colloids are initially randomly placed in the xy plane, and they remain close to that plane in the three-dimensional simulation. The pictures show projections on the xy-plane, taken at (a) $t = 0\,\mathrm{s}$, (b) $t = 1\,\mathrm{s}$, (c) $t = 3\,\mathrm{s}$ and (d) $t = 19\,\mathrm{s}$ after the onset of a $\dot{\gamma} = 10\,\mathrm{s}^{-1}$ shear flow. A movie will be available as supplementary material, on `html://cbp.tnw.utwente.nl/Downloads`.

gradient, i.e. the *xy*-plane. A shear rate of $10\,\mathrm{s}^{-1}$ was initialized at time $t = 0$ by means of sliding periodic boundary conditions and a linear fluid velocity profile $V(y) = \dot{\gamma} y \hat{\mathbf{e}}_x$; the latter was subsequently allowed to evolve freely, restricted only by the overall shear rate. Snapshots taken at several times during the simulation are shown in Fig. 4.2, and a movie is available as supplementary material. The first frame shows the initial box with the colloids randomly distributed in the *xy*-plane. In frames Fig. 4.2 (b) and Fig. 4.2 (c) the particles are seen to align in the flow direction, as well as segregating by size. The combination of processes results in a clearly ordered state at $t = 19\,\mathrm{s}$, see Fig. 4.2 (d). The system did not evolve significantly

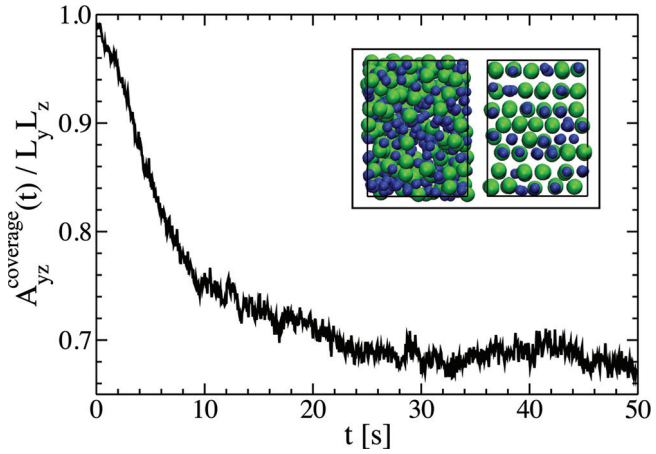

Figure 4.3: Fractional coverage of the gradient-vorticity (yz) plane when looking at the simulation box along the flow (x) direction, plotted as a function of time since the onset of shear. The 162 large colloids (green) and 274 small colloids (blue) are homogeneously distributed at the start of the simulation, resulting in the nearly complete coverage of the yz plane in the left inset. Exposure for 50 s to a shear rate of $10\,\mathrm{s}^{-1}$*, with the flow perpendicular to the (yz) plane of the paper, produced the configuration of the right inset with its markedly lower coverage due to colloidal alignment.*

over the next 7 s, apart from the obvious motion of the trains with the flow, at which point the simulation was stopped. The behavior seen in Fig. 4.2 is in agreement with two experiments that reported alignment and segregation of bidispere colloids in sheared viscoelastic fluids [38, 72]. It should be noted, however, that these experiments used shear-thinning polymer solutions, which tend to have different storage and loss moduli than the fluid simulated here, and that the experimentally observed alignment and segregation occurred close to the walls of very narrow rheometer slits, whereas the simulated process occurs in the bulk of the fluid. Flow-induced alignment of monodisperse colloids has been observed in experiments to occur in the bulk of a fluid comparable to the one studied here [92]. It is therefore likely that the segregation observed in the simulations will also occur in experiments.

In the second and larger system, the colloids were initially randomly distributed over the entire volume of the $41R_g \times 27R_g \times 20R_g$ ($1.4\,\mu\mathrm{m}^3$) simulation box. The 162 large and 274

small colloids occupied volume fractions of $\varphi^l \sim 10\%$ and $\varphi^s \sim 5\%$, respectively, and were surrounded by 65 472 liquid particles. The colloids remained homogeneously distributed in the quiescent fluid, but under a shear flow in the x direction with a velocity gradient of $\dot{\gamma} = 10\,\mathrm{s}^{-1}$ in the y direction, the colloids were again observed to align and segregate. An assessment of the progression rate of the alignment process was obtained by projecting the colloids onto the gradient-vorticity (yz) plane and calculating the resulting fractional coverage of this box face by the colloids. For the initial frame, with randomly distributed colloids, this coverage was about 99%. During the sheared simulation this fractional coverage steadily decreased, as shown in Fig. 4.3, to reach a plateau value of about 68% after around 20 s. The covered area, and hence the degree of alignment, remained fairly constant for the next 30 s, at which point the run was terminated. Snapshots of the initial and final frames of the simulation, displayed as insets to Fig. 4.3, confirm the considerable reduction of the covered area, which is a hallmark of alignment in the direction perpendicular to the yz plane. We note that in the current analysis the area covered by an outlier, i.e. a colloid that is not entrained, is comparable to that of an entire train, and hence that the actual degree of alignment is higher than indicated by the coverage fraction. The number of outliers changes only very slowly after the major aggregation process into chains has been completed.

To assess the colloidal segregation by size, beyond the impressions obtained by visual inspection, we counted the numbers of like and unlike pairs of consecutive colloids in the strings, as well as occurrences of unchained colloids, see Fig. 4.4. In this context, two colloids i and j are considered consecutive members of the same train when their centers of mass are within $R^i_{\mathrm{col}} + R^j_{\mathrm{col}} + 0.8\,R_g$ in the flow direction and within $0.5\,R_g$ in the two perpendicular directions; the minimum length of a train is two colloids. For clarity of interpretation, the development toward steady state has been skipped in favour of an analysis of the stationary phase during the final 25 s of the simulation. Although Fig. 4.3 suggests a steady state, computer animations of aligned systems reveal that colloidal trains repeatedly lose particles from either end and (re)capture colloids traveling on the same flow line; these variations are being averaged over in Fig. 4.4. The average numbers of like and unlike colloidal pairs are compared in Fig. 4.4 against their mean values expected from randomly mixed systems. In the latter case, all colloids occurring in one of the chains are randomly relabeled as ‘large’ or ‘small’, keeping constant the correct total numbers for each type and preserving the connec-

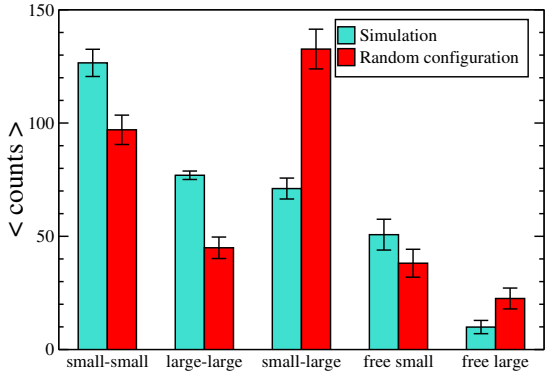

Figure 4.4: Histogram of the average counts of neighboring entrained colloids with equal or distinct sizes, and of unchained (free) colloids. The system contains 274 small colloids and 162 large colloids. Blue bars (left) show the simulation results, red bars (right) represent the averages for randomized systems with chain length distributions identical to those in the simulations. The error bars indicate standard deviations.

tions within all chains (as would have happened naturally when randomizing the colours of the colloids), before the neighbor analysis is performed. The results indicate a larger number of like pairs, and consequently a lower number of unlike pairs compared to those in the randomly mixed system. The comparison between the simulation and random configurations proves that size segregation indeed occurs in the system. We observe a larger number of free small colloids compared to when all colloids, those in the chains and the free ones, have been randomly renamed, while for large colloids we find the opposite. This result suggests that there is a larger proportion of chained large colloids than small ones.

The application of a shear flow is crucial for the formation and stabilization of strings and size segregation, since neither effect is observed in quiescent systems. The results presented thus far are also representative of simulations with smaller colloidal volume fractions, $\varphi^l = 4\%$ and $\varphi^s = 2\%$, and of simulations with a slightly larger size difference, $R^s_{\mathrm{col}} = 1R_g$ and $R^l_{\mathrm{col}} = 2R_g$.

In a recent work we presented an analysis of the net polymeric forces on a pair of equally sized colloids as a function of their separation distance [101]. This is conveniently realized in simulations with just two colloids dissolved in the sheared fluid, by moving the pair col-

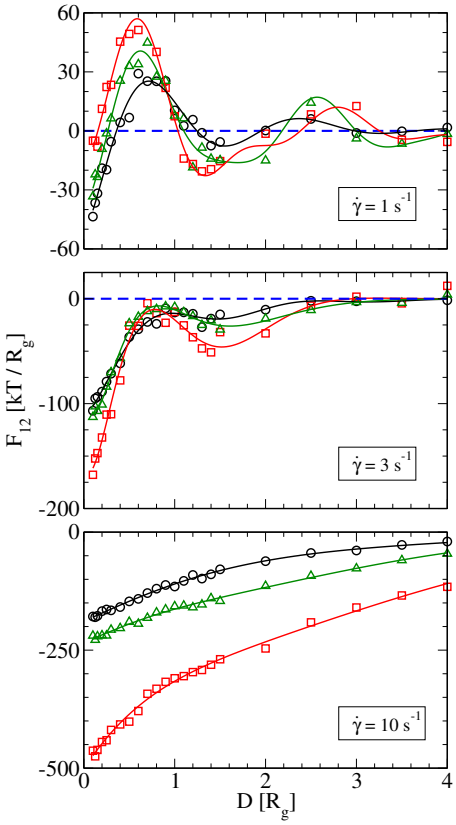

Figure 4.5: Effective particle-generated forces between two colloids as functions of the surface distance D between the colloids, for three shear rates. The markers distinguish between small-small (black ◯), large-small (green △) and large-large (red □) colloidal pairs.

lectively, as a rigid unit, under the sum of the forces $\mathbf{F}_1$ and $\mathbf{F}_2$ acting on colloids 1 and 2, respectively. For interpretational convenience, the orientation of the pair is kept parallel to the flow field. The RaPiD particles give rise to an effective force $F_{12} = (\mathbf{F}_2 - \mathbf{F}_1) \cdot \hat{\mathbf{e}}_x$ between the colloids, which is plotted in Fig. 4.5 as a function of the distance D separating the colloidal surfaces. Note that the purely repulsive direct inter-colloidal interaction ϕ_{cc}, whose range is limited to $D \sim 0.1R_g$, still has to be superimposed to get the total force between the colloids. For $\dot{\gamma} = 1\,\mathrm{s}^{-1}$, the colloids repel each other upto $D \sim 1R_g$, while for larger distances the force is close to zero. This tallies with the preceding simulation results, which indicate that the col-

loids do not align at this low shear rate. At the higher shear rate of $3\,s^{-1}$, the effective force has become attractive for almost all distances, and especially so at small distances. These forces are sufficiently strong to induce alignment, yielding strings with a colloidal spacing of $D \sim 0.4R_g$. The force curves for small-small and large-small are fairly similar, but the large-large pair has deeper minima reflecting stronger attractions – this difference is probably the origin of the segregation by size. Upon increasing the shear rate to $10\,s^{-1}$, the particle-induced attraction between the colloids gains in strength and the curves for the three distinct size combinations grow apart, see Fig. 4.5. At any given distance D, the largest force arise between two large colloids and the smallest force between two small colloids.

4.5 Conclusions

The highly coarse-grained Responsive Particle Dynamics method has been used to simulate colloids of two different sizes suspended in a visco-elastic fluid with the flow characteristics of a worm-like micellar solution. Under shear flow, the colloids are observed to flow-align into strings with a clear propensity to segregation by colloidal size. Simulations with pairs of colloids indicate that, beyond a critical shear rate, the sheared polymeric fluid generates an effective attractive force between the colloids, which increases with the sizes of the colloids involved. This attractive force drives the alignment, with the size-specificity giving rise to segregation. At low shear rates, however, the effective force is predominantly repulsive and the colloids mix homogeneously through the fluid.

To the best of our knowledge, flow alignment into segregated colloidal trains in the bulk of a fluid has not yet been observed experimentally. Segregated alignment of disperse colloids has been reported by two groups [38, 72] to occur in a very narrow slit containing a polymer solution, and alignment in the bulk has recently been observed in a worm-like micellar fluid [92]. Combining these experimental results with the current numerical study, it is very likely that segregated alignment will occur in the bulk of a worm-like micellar fluid.

5 Shear-induced colloids migration in a confined shear-thinning viscoelastic fluid

Spherical particles dispersed in viscoelastic fluids near a solid boundary are known to migrate toward the boundary during shear flow. Additionally, recent experiments show that these particles can form flow-induced structures near the walls, while in bulk, the particles remain randomly distributed. Previous simulation studies performed in our group demonstrated that spherical colloids dispersed in viscoelastic fluids may or may not shear-align in the bulk, depending on the rheological characteristics of the fluid. In this work, solid walls are added to the simulation boxes to investigate the effect of confinement on the distribution of colloids subjected to shear flow. The shear thinning viscoelastic fluid is simulated using the Responsive Particle Dynamics (RaPiD) method. In the RaPiD simulation method, each chain is modeled by a single smooth Brownian particle with slowly evolving interparticle degrees of freedom, which account for the entanglements between particles. The results obtained show that spherical particles dispersed in the simulated fluid mix homogeneously, while under shear, they migrate toward the closest wall. These results are in agreement with experimental observations.

5.1 Introduction

Wall effects can modify the dynamics of spherical particles dispersed in a suspending fluid subject to flow. A well-known effect is the particle migration in the system. The term migration refers to the lateral motion of a particle across the streamlines of the applied flow field. In Newtonian fluids, particle migration is expected only when inertial effects are important [33,46,104,106]. Experiments on neutrally buoyant spherical particles in Newtonian fluids flowing through a narrow tube demonstrate that rigid particles do not simply follow flow lines but can, in fact, migrate perpendicular to them [104]. Particles flowing at low Reynolds numbers through a cylindrical tube converge to a ring positioned at approximately 0.6-tube radius from the channel axis (the tubular pinch effect), while in rectangular (square) slits, the particles are driven to the mid-plane (mid-planes) of the channel [8, 16, 42, 46, 62, 105, 111]. These subtle effects originate in the non-linear inertial term of the Navier-Stokes equation, with an attractive lift arising from wall contributions, and an additional "lift" driving the particle down along the shear gradient direction [6, 7, 46, 61, 78, 100, 106]. Related effects have been observed for particles falling through a narrow canal as well as for particles in shear flows.

In contrast, if the suspending media presents characteristics of a non-Newtonian fluid, the migration of dispersed particles can be observed even for situations where inertial effects can be ignored (very low Reynold numbers). Experiments have reported that the particles accumulate at stationary positions ranging from the center of the slit to nearly touching the channel walls [37, 44, 45, 56, 58–60, 70, 71, 112]. Due to the complex rheological behavior of the visco-elastic solvent, theoretical investigations have progressed more slowly than investigations of viscous fluids and typically require numerical solutions of the Navier-Stokes equations for approximate solvent models in geometries with complex boundary conditions [9, 23, 24, 47, 49, 50, 95].

Spherical particles have been observed to migrate toward the closest wall in planar shear flows, both numerically and experimentally, by Caserta et al. [17] and D'Avino et al. [22]. They argue that viscoelasticity, when combined with confining walls, causes an imbalance in the normal stresses around the particle surface, resulting in its lateral motion. In this chapter, we describe observations of the colloids migration when dispersed in a shear-thinning viscoelastic fluid subject to linear shear flow and the presence of confining walls. The Re-

sponsive Particle Dynamics (RaPiD) method is used to simulate the suspending fluid.

5.2 Simulation method

5.2.1 The polymer solution

The shear-thinning viscoelastic properties of the liquid to be simulated are caused mainly by entanglements between the many long chains constituting the fluid. However, to reach long time and length scales, each polymer chain is represented only by the position of its center of mass in the RaPiD method [14, 117]. The interaction potential between the coarse-grained particles is responsible for describing the equilibrium position of the polymer chain's center of mass. The effect of entanglements between chains is included in the RaPiD method by the addition of a set of variables accounting for the number of entanglements between a particle and its neighbors. This number is compared against the system equilibrium entanglement number. As a result, a restoring potential is created that slows down the particle's dynamics. The interaction potential is then written as

$$\Phi(r,n) = pkT \sum_{i=1}^{N_p} \left[\frac{1-\phi_i}{\phi_i} \ln(1-\phi_i) - \chi\phi_i \right] + \frac{\alpha}{2} \sum_{i,j} (n_{ij} - n_0(r_{ij}))^2. \tag{5.1}$$

The first sum on the right-hand side gives the conservative potential describing the equilibrium thermodynamics of the system. It is based on the Flory-Huggins theory [36,51], adapted to compute the particle free energy given the chain's center-of-mass position [102]. The variable p is the number of Kuhn segments in the chain, k is the Boltzmann's constant, T is the temperature and N_p is the total number of chains. The particle free energy is calculated as a function of its local volume fraction ϕ_i, given by:

$$\phi_i = \frac{1}{\rho_{max}} \sum_{j=1}^{N_p} \omega(r_{ij}), \tag{5.2}$$

where ρ_{max} is the maximum particle density the system can reach for a given polymer concentration and $\omega(r)$ is a normalized function describing the local polymer density as a function of the distance between the particles i and j. The sum of $\omega(r)$ over N_p gives the local density ρ_i around particle i. The function $\omega(r)$ is a linear decreasing function and goes smoothly to zero at distances close to the cutoff radius, more details can be found on Ref. [102].

The second sum on the right-hand side of Eq. (5.1) describes the transient forces in the system due to entanglements between neighbor particles. The number of entanglements n_{ij} in a given configuration is compared with the system equilibrium number of entanglements:

$$n_0(r) = \left(\frac{r}{r_c} - 1\right)^2 : \forall\, r \leq r_c, \tag{5.3}$$

where r is the distance between two particles, and r_c is the cutoff radius for r. Deviations from the equilibrium imply transient forces, which evolve to zero as the number of entanglements is updated during the simulation according to:

$$dn_{ij} = -\frac{1}{\xi_t}\frac{d}{dn_{ij}}\Phi(r,n)dt + \sqrt{\frac{2kT\,dt}{\xi_t}}\Theta_{ij}. \tag{5.4}$$

The last term accounts for random displacements in n_{ij}. Θ_{ij} is a time-dependent random Markovian scalar with zero mean, unit variance and without correlation across particle pairs. The parameter ξ_t behaves as an "entanglement friction", which is given by $\xi_t = \alpha\tau$, where τ is the entanglement relaxation time and α is a parameter to adjust the strength of the entanglement potential. At equilibrium, the transient forces vanish, and the particle positions are only governed by the conservative part of the potential in Eq. (5.1).

5.2.2 Representing wall and colloids interactions

To construct the simulation box, two flat walls are added at the top and bottom in the y-direction. The wall-polymer and wall-colloid interactions, as well as colloid-colloid and colloid-polymer interactions, are given by the following equations:

$$\varphi_1(r) = 4\left(\frac{0.1}{r - a_1 R_{col}}\right)^8, \tag{5.5}$$

$$\varphi_2(r) = b_0 \exp[-b_1(r+b_2)^2]. \tag{5.6}$$

The potential $\varphi_1(r)$ represents the colloid particle's interactions with other colloid particles or with the walls, where r is the distance between the center of two colloids or its distance to the walls. In Eq. (5.5), $a_1 = 1$ for colloid-wall interactions and $a_1 = 2$ for colloid-colloid interactions. The potential $\varphi_2(r)$ gives the polymer-colloid and polymer-wall interactions, with b_k ($k = 0,\ 1,\ 2$) representing the potential fitting parameters, which values are listed in table 5.1.

The conservative potential described in Eq. (5.1) is written as a function of the local volume fraction ϕ_i around each particle i. The particles located close to the walls have a smaller number of neighbors compared with those in the bulk region and, as a consequence, the local volume fraction is also smaller in the vicinity of the walls. This imbalance in the density results in a non-realistic condensation of particles close to the walls during the simulations. To circumvent this problem, an extra density contribution is added in ρ_i (the sum in Eq. (5.2)) for particles located close to the walls. This additional density mimics the effect of having walls composed of fluid particles that have the same density as the particles in the bulk region. To calculate the extra density factor, we compute ρ_i for a single particle located close to a wall at various separation distances. It is important to assure that the wall dimensions are large enough to always have a particle within the cutoff radius of the target particle inside the box. The result is then plotted and fitted with a function of the form

$$\rho_i^w(r) = \frac{c_0(r-r_s)}{1+c_1\exp[-c_2(r-r_s)]}, \tag{5.7}$$

where r is the distance of particle i from the wall, c_k are the fitting parameters summarized in table 5.1, and $r_s = L_w - r_c$, with L_w representing the wall distance from the center of the box and r_c the cutoff radius. The function $\rho_i^w(r)$ is added as an extra local density for particles located inside r_c, which results in an additional contribution to the conservative potential. This procedure results in a smoother distribution of particles close to the walls, and allows for measuring the effect of a wall made of particles indirectly, rather than actually adding particles to represent them during the simulations. This simplification of the model demands a smaller computational effort, which in turn allows the simulation of larger systems.

5.2.3 Moving walls

A linear flow profile in the system is created by moving both walls in opposite directions, in this way the liquid velocity is maximum at the walls and zero at the middle of the box. The friction between the wall and the surrounding liquid and the friction between the liquid particles itself are responsible for creating the flow profile. The friction between the RaPiD particles is caused mainly by entanglements. The friction per particle ξ_i is then assumed to be proportional to the number of entanglements of particle i with its neighbors and is written

Potential parameters					
$\phi_{col-pol}$		$\phi_{wall-pol}$		ρ_i^w	
b_0	100	b_0	150	c_0	0.5
b_1	2	b_1	0.25	c_1	68.8
b_2	(R_g - R_{col})	b_2	3	c_2	2.1

Table 5.1: Parameters describing colloid-polymer and wall-polymer interactions (Eq. (5.6)), and for the function representing the additional density for fluid particles located close to the walls (Eq. (5.7)).

as

$$\xi_i = \xi_s + \xi_e \sum_{j \neq i} \sqrt{|n_{ij}| n_0(r_{ij})}, \tag{5.8}$$

where ξ_s is the solvent friction and ξ_e is an input parameter that defines the entanglement friction per particle. The wall friction is described by a decaying function that depends on the particle-wall distance $\xi_i^w(y_i)$, where y_i is the distance between particle i and the walls along the y-direction,

$$\xi_i^w(y_i) = \begin{cases} \xi_0^w \left(\frac{y_i}{r_c} - 1\right)^2 & : \quad y_i < r_c, \\ 0 & : \quad y_i > r_c, \end{cases} \tag{5.9}$$

r_c is the cutoff radius defining the region where the wall-polymer friction is present, and ξ_0^w is an input parameter that defines the strength of the polymer-wall friction.

Having described all the interactions between the system components, the displacement of particle i over a time step dt is updated with the following propagator:

$$d\mathbf{r}_i = \frac{1}{\xi_i + \xi_i^w} \left(\mathbf{F}_i + \xi_i \langle V \rangle_i + \xi_i^w v_w\right) dt + \nabla_i \left(\frac{kT}{\xi_i + \xi_i^w}\right) dt + \sqrt{\frac{2kT\,dt}{\xi_i + \xi_i^w}}\, \boldsymbol{\Theta}_i, \tag{5.10}$$

where $\mathbf{F}_i$ is the force acting between liquid particles, given by $-\nabla[\Phi(r,n) + \varphi_{col-pol}(r) + \varphi_{wall-pol}(r)]$. The wall velocity is given by v_w. If $v_w \neq 0$, the box is divided into layers and the instantaneous flow field in the x-direction is calculated by attributing the displacements of each particle to its two surrounding planes by a lever rule. The flow field is then smoothed by averaging at every plane over the flow field history using an exponentially decaying weight

function [102]. In this way, the average liquid velocity, $\langle V \rangle_i$, at the position of particle i is obtained. In the case where the walls are kept stationary, $\langle V \rangle_i$ is always zero. This procedure is sufficient to create a linear flow profile in the box. To accelerate the simulations, the systems are started with the expected steady-state flow profile, rather than simulating the slow start-up behavior required to develop a linear flow profile. Since $\xi_i + \xi_i^w$ is not constant the second term on the right-hand side of Eq. (5.10) is added to correct for this fact. And the last term is a time-dependent Markovian random vector, accouting for Brownian motion. The particle-wall friction ξ_i^w is only defined in Eq. (5.10) if $v_w \neq 0$.

The colloids motion is updated in a similar way, according to

$$d\mathbf{r}_i^c = \frac{1}{\xi_c}\mathbf{F}_i^c dt + \langle V \rangle_i \hat{e}_x dt + \sqrt{\frac{2kT\,dt}{\xi_c}}\,\mathbf{\Theta}_i^c. \tag{5.11}$$

As the colloids do not entangle with liquid particles, they have a constant friction coefficient ξ_c, and are subject to the flow field created by moving the walls according to the second term in the right hand side. $\mathbf{F}_i^c$ is the force acting on colloid i, given by $-\nabla[\varphi_{col-col}(r) + \varphi_{col-pol}(r) + \varphi_{col-wall}(r)]$. The last term is again a time-dependent Markovian random vector.

5.3 Results

The simulated viscoelastic fluid has characteristics of a semi-dilute polymer solution. Using the RaPid simulation method, we have recently simulated the rheological properties of a shear-thinning viscoelastic polymer solution [102], where we demonstrated good agreement with experimental rheology measurements [107]. Colloids dispersed in the bulk of the suspending fluid remained randomly distributed after the onset of shear flow, while colloids homogeneously dispersed in a second shear-thinning fluid, which simulated a wormlike micellar solution, formed chains of colloids along the flow direction when the shear rate was increased over some critical value. These observations are also in agreement with experiments [92]. In this chapter, we investigate the effects of confinement on the distribution of colloids dispersed in a simulated polymer solution subjected to shear flow. Information about the polymer solution simulation and experimental parameters can be found in Ref. [102].

Before adding colloids to the simulation box, we computed the distribution of liquid particles for the quiescent fluid. The simulations are performed in a box with dimensions

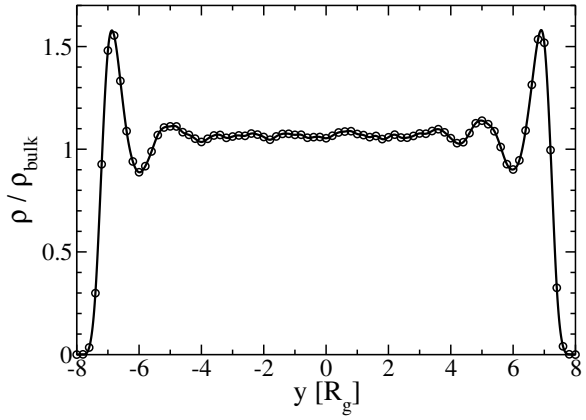

Figure 5.1: Polymer density as a function of the distance from the walls, located at $y = -8\,R_g$ and $y = 8\,R_g$. The density is normalized by the bulk density ρ_{bulk}

$8 \times 16 \times 8\,\mathrm{R}_g$, the walls are located in the y-direction at -8 and $8\,\mathrm{R}_g$. In the x and z-directions, the system obeys periodic boundary conditions. The box is filled with coarse-grained polymer particles with a bulk density of $\rho_{bulk} = 3.5$ polymers/R_g^3, resulting in 3585 particles inside the box. The particle's density is plotted as a function of the distance perpendicular to the walls in Fig. 5.1. The result shows a larger concentration of polymer particles close to the walls, in comparison to the bulk region, with a peak of $1.6\,\rho_{bulk}$ at a distance of $1\,\mathrm{R}_g$ from the wall. Additionally, there is also a second smaller peak at $y = 5\,\mathrm{R}_g$. The system is symmetric in respect to the center of the box, and thus has similar density peaks on the negative side. The adsorption of polymers near the walls can be explained by the development of a depletion layer caused by entropic effects. Bolhuis et al. [12], using Monte Carlo simulations, showed that the probability of a polymer's center-of-mass being close to a hard wall increases as the polymer density in the system is increased. This phenomenon is known as liquid layering.

To investigate the effect of shear flow on the distribution of colloids dispersed in a confined viscoelastic polymer solution, a string of 6 colloids, each one with a radius of $\mathrm{R}_{col} = 1\,\mathrm{R}_g$ and an initial separation of $0.4\,\mathrm{R}_g$, is placed in the center of a box with dimensions $16 \times 16 \times 10\,\mathrm{R}_g$ and walls at the top and bottom in the y-direction (see Fig. 5.3). Different shear rates are applied by moving the walls with constant velocity, which allows the system to create a linear flow profile due to the polymer-wall friction defined in Eq. (5.9), we set

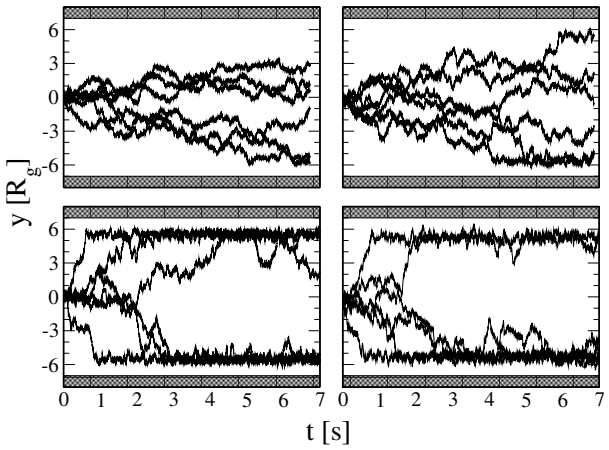

Figure 5.2: Trajectory along the direction perpendicular to the walls of 6 colloids, initially aligned in the center of the box, as a function of time. The applied shear rates are given by: top left: $\dot{\gamma} = 10\,s^{-1}$*, top right:* $\dot{\gamma} = 30\,s^{-1}$*, bottom left:* $\dot{\gamma} = 100\,s^{-1}$ *and bottom right:* $\dot{\gamma} = 200\,s^{-1}$.

$\xi_0^w = 10^2\xi_e$. In Fig. 5.2, we plot the trajectory of the center of each colloid during the simulation run for four different shear rates ($\dot{\gamma}$). The results show that the colloids migrate towards one of the walls. As the system is symmetric, the colloids have the same probability to move to the bottom or top wall. When the shear rate is increased, the migration rate also increases. When the lower shear rate of $\dot{\gamma} = 10\,\mathrm{s}^{-1}$ is applied, most of the colloids do not have time to reach an equilibrium distance from the walls in the allowed simulation time. The number of colloid particles migrating to the walls increases when the shear rate is increased. For the shear rates $\dot{\gamma} = 100\,\mathrm{s}^{-1}$ and $\dot{\gamma} = 200\,\mathrm{s}^{-1}$, all 6 colloids approach an equilibrium distance from one of the walls. The shaded regions represent the zone where a colloid cannot access due its finite size. The center-of-mass of the colloids reach an average equilibrium position at around $\pm 5\,\mathrm{R}_g$, meaning that the colloids stop at $1\,\mathrm{R}_g$ away from touching the walls. This behavior can be explained by the larger density of polymers close to the walls, shown by the peaks at $\pm 7\,\mathrm{R}_g$ in Fig. 5.1. The increased polymer density prevents the colloids from moving closer to the wall.

Snapshots from the simulations for the system with $\dot{\gamma} = 100\,\mathrm{s}^{-1}$ is presented in Fig. 5.3.

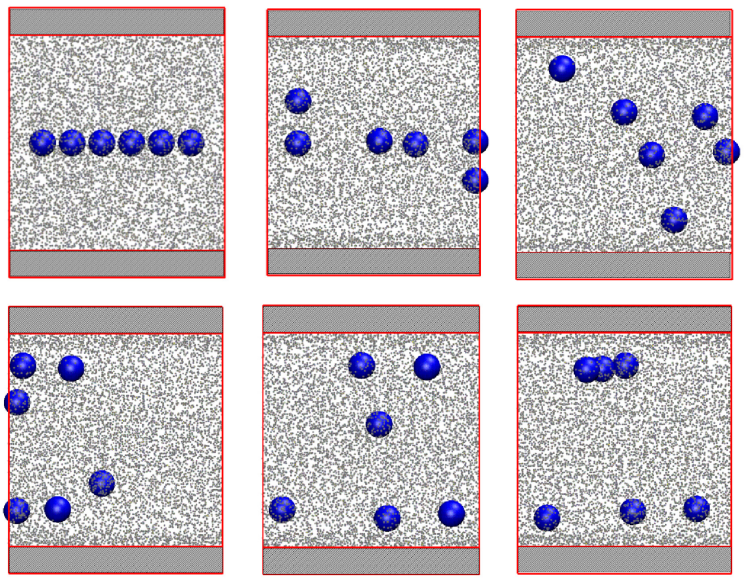

Figure 5.3: Simulation snapshots at different times. From top left to bottom right: $t =$ 0, 0.5, 1, 2.5, 3 and 5 s, respectively. The shear rate is $\dot{\gamma} = 100\,s^{-1}$, with the flow along the horizontal direction and velocity gradient in the vertical direction.

It is possible to observe that the colloids do not touch the walls, and with a closer observation one can also see a layer with higher density in the vicinity of the walls. Another point to notice is that the colloids do not align close to the walls. The colloids reach the same level in the box, but they remain homogeneously distributed in that plane. Experimental observations indicate that in some viscoelastic fluids migration toward the wall can induce alignment of the colloids [93], while in the bulk, they distribute homogeneously under shear. However, this is not the case for the polymer solution we simulated. Additionally, we attempted to increase the number of colloids already starting in their equilibrium position from the walls, but even for larger colloid concentrations they remained randomly distributed.

To investigate whether the migration is symmetric between both walls, and also to check if a pre-assembled colloid chain close to the walls would be stable in shear flow, the same box as described before is used here again. Now in each simulation, the string of colloids began at different positions relative to the walls, and a shear rate of $\dot{\gamma} = 200\,\mathrm{s}^{-1}$ is applied. The results

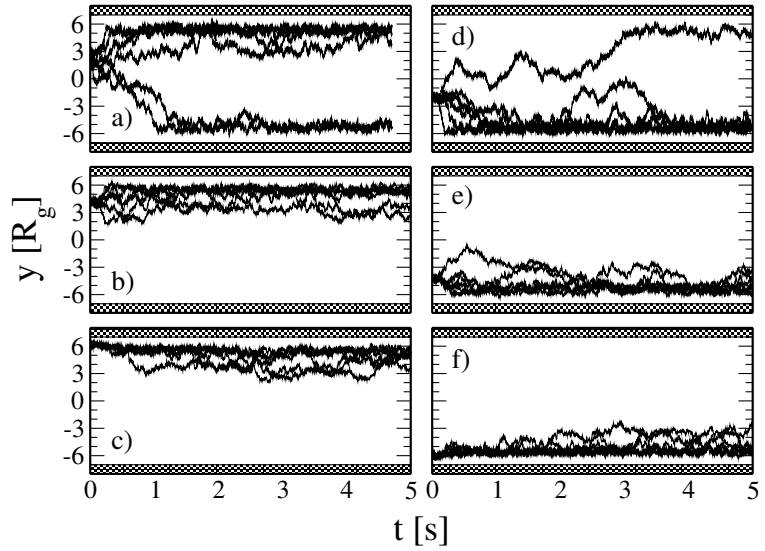

Figure 5.4: Trajectory of 6 aligned colloids starting at different heights in relation to the walls. Initial positions are: a) $2\,R_g$*, b)* $4\,R_g$*, c)* $6\,R_g$*, d)* $-2\,R_g$*, e)* $-4\,R_g$*, f)* $-6\,R_g$*. The applied shear rate is* $\dot{\gamma} = 200\,s^{-1}$.

are summarized in Fig. 5.4 and indicate that the colloids always migrate in direction of the closest wall. This behavior has also been observed experimentally by Caserta et al. [17] for spherical particles dispersed in polymer solutions subject to linear flow. Additionally, this behavior has been observed in numerical simulations [22]. At initial positions equal to $\pm 2\,R_g$, some colloids still move in direction of the most distant wall, which can occur due to collisions with the other colloids at the beginning of the simulation and because they are still close to the center of the box. When the particles are close to the center of the box, they can move to the region with inverted shear flow due to the colloid's Brownian motion. Starting at an initial position of $\pm 4\,R_g$, all of the colloids moved to the closest wall. From Fig. 5.2, we observed that the equilibrium position is again around $\pm 5\,R_g$. When the initial position of the colloid is approximately $\pm 6\,R_g$ the colloids remain around the initial level and reach a steady-state position at around $\pm 5\,R_g$. However, the colloids did not remain aligned in the flow direction as well as they did in all other cases analyzed.

Boxes with different gap values between the walls are also simulated to investigate the

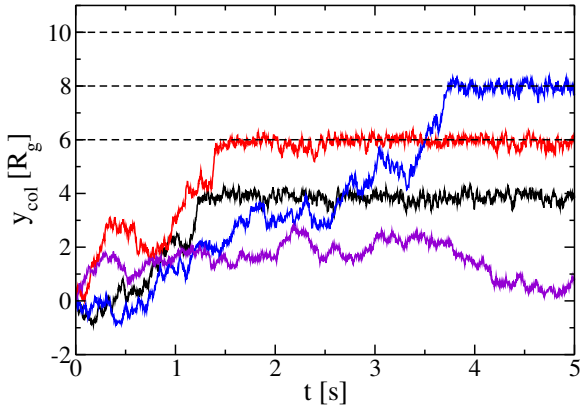

Figure 5.5: Trajectory of one colloid located in boxes with different gaps between the walls, only the positive part of the box is shown. The dashed lines represent three different walls height from the center of the box, a shear rate of $\dot{\gamma} = 100\,s^{-1}$ is applied. The wall distances from the center of box are the following: $6\,R_g$ (black), $8\,R_g$ (red), $10\,R_g$ (blue) and $20\,R_g$ (purple).

influence of confinement on the colloid's migration. The x and z-directions are fixed to $8\,\mathrm{R}_g$ in all the simulations, and the direction perpendicular to the walls is increased stepwise from 6 to $20\,\mathrm{R}_g$. In each system, a single colloid is placed in the center of the box, and a shear rate of $\dot{\gamma} = 100\,\mathrm{s}^{-1}$ is applied. As the flow and migration is symmetric for both sides of the box, as showed in Fig. 5.4, we projected all the trajectories to the positive part of the box in Fig. 5.5. The horizontal dashed lines in Fig. 5.5 represent three different gaps between the walls. The results show that the colloids migrate toward the wall, with their center stopping at an equilibrium position of $2\,\mathrm{R}_g$ away from the wall, regardless of the gap size. The exception is for a wall located at $20\,\mathrm{R}_g$ from the box center. In this case the colloid simply diffuses around its initial position, which is the same behavior found when we add periodic boundary conditions in the three box directions. Therefore, as expected, if the colloid is located too far from the wall the system recovers bulk effects. This finding confirms that confinement is crucial for colloids to migrate between streamlines in the sheared liquid. Another conclusion drawn from the trajectories is that as the colloids approach the walls or as the gap becomes smaller, they seem to increase their velocity of migration. That is, the colloid shows a less

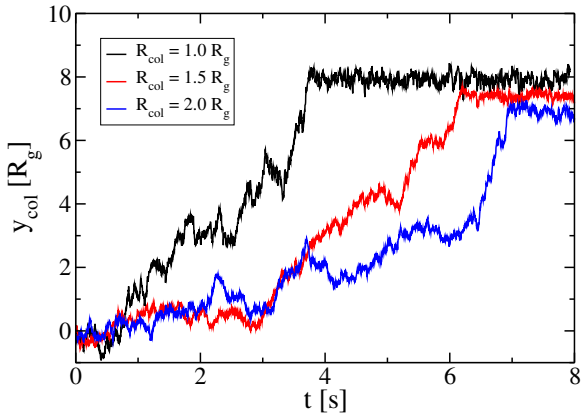

Figure 5.6: Trajectories as a function of time for a colloid dispersed in a confined box, for three different colloid radius. A shear rate of $\dot{\gamma} = 100\,s^{-1}$ *is applied.*

erratic motion as it approaches the wall.

To verify the effect of increasing the radius of the colloids in the migration process, we simulated colloids with $R_{col} = 1.5\,R_g$ and $R_{col} = 2\,R_g$ and compared their trajectories along the wall direction, where the walls were located at $10\,R_g$ from the center of the box. The results are plotted in Fig. 5.6, and also includes the trajectory for the colloid with $R_{col} = 1\,R_g$ that we have been using thus far. The calculations show that the surface position of the colloid, independently of its radius, always stops migrating at a distance of $1\,R_g$ from the wall. We also observed that colloids with larger radii take a longer time to reach the equilibrium position from the walls. The reason for this behavior is due to the increased friction between the colloid and the liquid ξ_{col} as the radius of the colloid is increased. We assumed that colloids obey Stokes law: $\xi_{col} = 6\pi\eta R_{col}$. Thus, when R_{col} is increased the mobility of the colloids is reduced.

5.4 Conclusions

We performed a simulation study to investigate the phenomenon of spherical colloid migration when dispersed in a shear-thinning viscoelastic fluid confined between hard walls. The migration was investigated by varying the confinement, the shear rate and the colloid's radius.

The system is subjected to a linear shear flow, which induces migration to regions of larger shear rates. Colloids dispersed in stationary fluids always remain homogeneously distributed in the simulation box, regardless of whether wall effects are present. The modeled polymer solution used here has already been investigated for dispersions of colloids in periodic systems without wall effects. When walls are not considered, no structuring of the colloids could be observed over a wide range of applied shear rates [102]. Therefore, the addition of the walls causes the colloids to migrate toward them in the sheared system. Increasing shear rate or confinement accelerates the migration process, and the particles have the tendency to always migrate in direction of the closest wall. These observations are in good agreement with recent experiments in similar systems [17], where a linear shear flow was also applied.

Experiments have shown that migration can induce the colloids to align close to the walls [93]. As we observed alignment in the bulk of a second model fluid previously simulated in our group, which shows rheological characteristics (shear-thinning) similar to the fluid used here, we checked whether it would also be the case that alignment appears in the simulated polymer solution. Thus, we started with an aligned chain at the equilibrium position from the walls and then observed if they would remain stable in that configuration. We found that while they do remain in the same plane, the colloids disperse along the plane. We also simulated colloids with different radii and observed that when increasing the radius, the migration becomes slower but does not stop completely. The slower migration can be related to an increase of the colloid friction as the radius is increased.

In conclusion, we showed that our particle-based model, when used to simulate viscoelastic fluids, is capable of reproducing colloid migration in confined boxes. We expect that further investigations into the migration process could proceed by changing the fluid simulation parameters to obtain different rheological properties and also by investigating stress differences in the system. We also believe that in some fluids, alignment close to the walls will be captured by our simulations even when it does not take place in the bulk.

6 Exploring RaPiD simulation parameters in the modeling of complex fluids

Responsive Particle Dynamics (RaPiD) simulations can be used to model the rheology of complex fluids. Different rheological properties are obtained by tuning the parameters responsible for describing the dynamics of the system. We show here how the simulation parameters change the linear rheology of the fluids. Results for the stress autocorrelation as a function of time and its Fourier transform, which result in the storage and loss moduli, are computed. By analyzing a number of curves we investigate the effects of each simulation parameter on the description of those quantities for a model fluid. We then use experimental data for a viscoelastic liquid to exemplify the findings, and a systematic way of tuning the parameters is suggested. The set of parameters describing the fluids sufficiently well is chosen. From this point, simulations can be carried out to make predictions about the liquid properties. This is demonstrated by computing the non-linear rheology of the solution, and comparing it to experimental measurements.

6.1 Introduction

The ability of modeling viscoelastic fluids with distinct rheological properties, by changing only few input parameters in the Responsive Particle Dynamics (RaPiD) simulation method, can be used to obtain a large variety of complex fluids. Being RaPiD a coarse-grained method, it is possible to separate the parameters in two groups. Firstly, we have a set of parameters

that are taken from the characteristics of the material to be simulated. In our case we simulate polymer solutions, thus to determine equilibrium properties some informations should be known from experimental measurements, e.g., chain length, radius of gyration, molecular weight. Secondly, there will be parameters related to the coupling between the dynamics of the eliminated and retained coordinates, and they are tuned in order to reproduce the fluid's linear rheology.

If the solution to be simulated is homogeneous and composed by long flexible chains, the potential describing the equilibrium position of the chains' center of mass results in a very soft potential, independently of the detailed structural characteristics of the material. This fact was used to simulate two distinct viscoelastic fluids in a previous work [102], where we used the experimental parameters of one fluid to simulate the rheology of two different liquids. In that case, only the parameters governing the dynamics of the systems were adjusted to obtain agreement with experiments. Despite the fact that they are both shear-thinning viscoelastic fluids, differences in their response to an applied shear flow leads to absence or formation of colloid string-like structures, in agreement with experimental observations [92]. The linear and non-linear rheology of the liquids were also in agreement with experiments [107]. The results demonstrate that RaPiD simulations can model the rheology of the fluids, and also describe the colloids alignment process caused by the complex rheology of the fluid during shear flow, validating our simulation method.

In this chapter we investigate the effect of the parameters responsible to control the dynamics of the particles by observing the linear rheology of the fluids. From analyzing curves for many combinations of parameters, we expect to get a better understanding on how they affect the rheology of the fluids, in the hope of obtaining a systematic way of fitting experimental curves. And once the parameters are obtained, predictions about the system properties can be done with our simulation model.

6.2 The RaPiD simulation model

In this work we study the possibility to simulate the rheological properties of a large class of complex fluids. Our general aim is to develop a simulation model that can be used to simulate large amount of these fluids, possibly in complicated geometries and complicated flows.

In order to speed up the simulations as much as possible, the description of the structural properties of the molecules constituting the fluid must be limited to a bare minimum necessary to obtain the correct flow behavior. In the RaPiD model that we use in this work, each molecule is represented by its center of mass position alone. Forces on RaPiD particles are of two kinds, the average forces depending on the configuration of the RaPiD particles, and transient forces describing the correlation between the dynamics of the eliminated small scale degrees of freedom and the dynamics of the retained degrees of freedom, i.e. the coordinates of the RaPiD particles.

6.2.1 Potential of mean force

The average forces on the RaPiD particles are governed by the so called potential of mean force defined as

$$\Phi_c(r) = -kT \ln\left(\int \exp\{-V(r,q)\}dq\right), \tag{6.1}$$

where $V(r,q)$ is the potential energy of the small scale system with r the RaPiD coordinates, or coarse variables, and q the internal degrees of freedom of all particles and possibly solvent degrees of freedom. A simulation of the coarse variables using the potential of mean forces as its energy will produce the exact structural and thermodynamic properties of the system. In practice, of course, the potential of mean force can only approximately be represented in a form depending very much on the characteristics of the system to be simulated [68]. In the context of RaPiD two types of representations of the potential of mean force have been used. When simulating concentrated suspensions of star polymers, Padding et al. [90] represented the potential of mean force by a sum of pair potentials depending on the distances between the stars, their diameters, and the number of arms of the interacting particles [69]. More complicated pair potentials were used in simulations of pressure sensitive adhesives [88,89]. A second type of representation of the potential of mean force was used by Kindt and Briels [63] when simulating polymer melts. In this representation each particle contributes an amount of free energy to the potential of mean force that depends on the local density of polymers around it. The precise amount contributed by each particle is simply taken to be equal to its free energy in a homogeneous bulk system with a density equal to the given local density. The resulting potential of mean force puts a penalty on large scale density

fluctuations and gives rise to the correct isothermal compressibility. In our previous work [102] we extended this model to be applicable to polymer solutions. Since this is also the model used in the present work, we briefly describe its main ingredients in the remaining part of this subsection.

For solutions, interactions between solvent and solute molecules become important and must be included in the simulation model. Instead of explicitly simulating the solvent particles, we use the Flory-Huggins (FH) theory [36,51] to incorporate interactions between polymers and solvent molecules in the potential of mean force of the polymers, and thus obtain an implicit solvent model. In the spirit of Pagonabaraga and Frenkel [63, 91, 113] we write the potential of mean force as a sum of contributions from each polymer molecule [102]. The actual contribution by polymer i is equal to the configurational free energy of a polymer in a homogeneous solution with polymer volume fraction equal to ϕ_i. The latter is the local volume fraction in the simulated solution at the position of polymer i (see below). The potential of mean force Φ_c is then

$$\Phi_c(\phi) = \sum_{i=1}^{N_p} a_p(\phi_i) = pkT \sum_{i=1}^{N_p} \left[\frac{1-\phi_i}{\phi_i} \ln(1-\phi_i) - \chi\phi_i \right], \tag{6.2}$$

where p is the number of Kuhn segments in the chain, k is the Boltzmann's constant, T the temperature, and N_p the number of polymer chains. The interaction between the polymer chains and the solvent molecules is described by the Flory-Huggins parameter χ. The latter can be used to control the quality of the solvent in relation to the polymers. Notice that the free energy contributed by translational degrees of freedom of the coarse variables has been excluded from the potential of mean force since it will be produced by the simulation.

ϕ_i is the local chain volume fraction around particle i, computed as

$$\phi_i(r_{ij}) = \frac{1}{\rho_{max}} \sum_{i=1}^{N_p} \omega(r_{ij}), \tag{6.3}$$

where ρ_{max} defines the maximum number density of polymers the system is allowed to reach. The weight function $\omega(r_{ij})$ represents the relative contribution of the monomers of polymer j to the density experienced by the monomers of partile i, hence $\omega(r_{ij})$ must be a function that smoothly decays with increasing r_{ij} until it becomes zero at some cutoff value of about twice the radius of gyration of the polymers. A random distribution of the centers of mass of

all polymers should turn the sum in Eq. (6.3) into the overall number density of chains, hence $\omega(r_{ij})$ must integrate to unity. For further details we refer to Ref. [102].

6.2.2 Transient forces

We now discuss the second type of forces felt by the RaPiD particles. It is well known that in polymer systems the chain connectivity in combination with strong repulsive forces gives rise to "topological constraints". As an example of such forces, consider two well mixed overlapping linear polymers. Topological constraints will temporarily strongly resist displacements of the centers of mass of the two polymers, while in the equilibrium state the free energy of the internal degrees may not be that different. This gives rise to the typical (linear) visco-elastic behavior of entangled polymer solutions. On the other hand, once the two polymers have been disentangled, it will take some time before they mix again. This gives rise to strong shear thinning when shear rates are larger than one over the characteristic time for mixing.

By taking minus the gradient of the potential of mean force, Eq. (6.1), with respect to one of the coarse variables $\mathbf{r}_i$ one obtains an expression that averages the force on the chosen variable over all internal degrees of freedom q. Topological constraints, however, may cause the system to make extremely large detours in order to achieve seemingly small changes in its configuration. In the potential of mean force all configurations are taken into account, while in reality only a subset of these is sampled until the coarse configuration has changed substantially. It is obvious therefore that the forces that drive the dynamics of the coarse system are not equal to those derived from the potential of mean force.

For simplicity we will refer to topological constraints by the name entanglements. The reader should not confuse "the number of entanglements" or "entanglement number", used below, with $Z = \frac{M}{M_e}$, which in reptation theory indicates that the mass of a polymer is Z times its entanglement mass [26]. The effect of entanglements is included into the model by adding to the list of dynamical variables the set $n = \{n_{ij} | r_{ij} \leq r_{cut}\}$, i.e. one dynamical variable for each pair of polymers whose distance is less than some cutoff. n_{ij} is called the number of entanglements between particles i and j. It keeps track of the thermodynamic state of the eliminated coordinates. For each coarse configuration, n_{ij} is assumed to have an equilibrium value depending only on the distance between the two polymers, and denoted by $n_0(r_{ij})$.

For Gaussian chains, $n_0(r_{ij})$ may be chosen to be proportional to the number of monomer-contacts, or the overlap between two chains at a distance r_{ij}. This overlap between Gaussian chains is itself approximately a Gaussian function of the distance between the centers of mass of the two polymers [1]. However, to avoid zero forces at short distances we represent $n_0(r_{ij})$ by a quadratically decaying function, as follow

$$n_0(r_{ij}) = \begin{cases} \left(\dfrac{r_{ij}}{r_c} - 1\right)^2 & : \; r_{ij} \leq r_c, \\ \\ 0 & : \; r_{ij} > r_c. \end{cases} \tag{6.4}$$

When all entanglement numbers are equal to their equilibrium values, the internal and the eliminated degrees of freedom are in equilibrium and the forces are equal to those derived from the potential of mean force. Deviations of entanglement numbers from their equilibrium values give rise to additional forces. These forces are modeled by adding to the potential of mean force a transient potential $\Phi_t(r,n)$. To first order, the general form of the transient potential is a quadratic function in the deviations of the entanglement numbers from their equilibrium values [14], representing the tendency of the system to always move towards its equilibrium state. So,

$$\Phi_t(r,n) = \frac{1}{2}\alpha \sum_{i,j} (n_{ij} - n_0(r_{ij}))^2. \tag{6.5}$$

The parameter α controls the strength of the fluctuations in the entanglement numbers deviations from their equilibrium values.

For any given configuration of the coarse variables, the entanglement numbers relax towards their corresponding equilibrium values. This relaxation is assumed to be governed by a simple linear equation augmented with a random contribution obeying the fluctuation-dissipation theorem [14, 117]:

$$dn_{ij} = \frac{1}{\tau}\left(n_0(r_{ij}) - n_{ij}\right) dt + \Theta_{ij}\sqrt{\frac{2kT\,dt}{\alpha\tau}}. \tag{6.6}$$

The first term gives rise to an exponential decay of n_{ij} towards $n_0(r_{ij})$ with characteristic time τ. In most polymer systems, a single relaxation time is not enough to describe the correct dynamics of the system. In the case of linear polymers, dynamical processes occur over a wide spectrum of characteristic times, either of the Rouse or the reptation type. In

other cases a wide range of characteristic times exists because experimental polymer systems often are very polydisperse. From a different point of view one may expect that Gaussian chains which hardly overlap may disentangle faster than those which overlap severely. In the former case the number of entanglements is not only smaller than in the latter case, but the entanglements are also "looser", and therefore disentangle more easily. To include this effect in the model, the relaxation time is defined to be a function of the distance between two neighboring particles, according to the expression

$$\tau_{ij} = \tau_0 \exp\left(-\frac{r_{ij}}{\lambda}\right), \tag{6.7}$$

where τ_0 is a time constant and λ defines the decay length of the relaxation time. The second term on the right hand side of Eq. (6.6) describes random fluctuations in n_{ij}, with Θ_{ij} being a time-dependent random Markovian scalar with zero mean, unit average, and without correlations across particle pairs.

6.2.3 Brownian dynamics

Having defined the interaction potentials between the particles, we proceed to define the propagator which maps the configuration at time t to that at time $t + dt$. Because the time evolution of soft matter systems is highly overdamped we adopt the Brownian dynamics propagator, implying that the position of particle i is updated during the simulation according to [14, 117]

$$d\mathbf{r}_i = -\frac{1}{\xi_i}\left(\nabla_i \Phi_C + \nabla_i \Phi_t\right) dt + \nabla_i \left(\frac{kT}{\xi_i}\right) dt + \boldsymbol{\Theta}_{ij} \sqrt{\frac{2kT\,dt}{\xi_i}}. \tag{6.8}$$

The first term on the right hand side contains minus the gradient with respect to $\mathbf{r}_i$ of the sum of the conservative and transient potential, resulting in the force applied to particle i. The force due to the transient potential is a sum of pair terms, each proportional to the derivative of $n_0(r_{ij})$ for some value of j. In order to prevent such pair-forces to become zero when the corresponding distance is zero we have made sure above that the derivative of $n_0(r_{ij})$ for $r_{ij} = 0$ is non-zero. The force on particle i is turned into a displacement over time dt by dividing by the friction ξ_i and multiplying by the time step dt. The second term in the Brownian propagator accounts for the fact that ξ_i is not in general a constant (see below), and

the last term describes the random displacements characteristic for Brownian motion; $\mathbf{\Theta}_{ij}$ is a time-dependent Markovian random vector, with unit variance and zero mean.

The friction felt by a particle is assumed to depend linearly on the degree of entanglement with neighboring chains:

$$\xi_i = \xi_s + \xi_e \sum_{j \neq i} \sqrt{|n_{ij}| n_0(r_{ij})}, \tag{6.9}$$

where ξ_e is the friction per entanglement and ξ_s is the background friction by the solvent. The somewhat peculiar way of writing the linear dependence on the number of entanglements by taking the product of $|n_{ij}|$ and $n_0(r_{ij})$ and next taking the square root is to make sure that the friction between two particles becomes zero beyond the cutoff distance.

Forces due to Φ_t are called transient forces. If we were to freeze the values of the coarse variables, i.e. we would freeze the coarse configuration of the system, the entanglement numbers would gradually relax towards their equilibrium values and the corresponding forces would relax to zero. As can be seen from Eq. (6.5), since $n_0(r_{ij})$ is a monotonous function of r_{ij}, the entanglement numbers drive the system towards configurations with interparticle distances such that all $n_0(r_{ij})$ are equal to the instantaneous values of the n_{ij}. The effect of the transient forces therefore is to severely slow down the dynamics of the particles, mimicking the effect of entanglements between long flexible chains.

The precise physical meaning of n can be adjusted to the characteristics of the system of interest. In the case of polymer chains it can be interpreted as the number of entanglements between a chain and its neighbors. To simulate telechelic polymer networks, Sprakel et al. [109] used the number of bridges between two micelles as the variable described by n. For simulations of pressure sensitive adhesives, Padding et al. [88] used two different set of variables to represent the eliminated coordinates, one being the intermixing of the chains, as we used for linear chains, and the other describing sticker groups shared between two particles. Obviously, the model may be more successful in capturing the physics of the system being described in some cases than in others. For example, for solutions of linear chains the model may be successful for systems slightly, or even substantially above the overlap concentration, but it will most probably not capture the correct physics for highly concentrated solutions or melts. It is, however, conceivable that the model may be adjusted, while keeping its main ingredients intact, such that also these systems can be described faithfully.

Simulation parameter	Symbol	Value
Temperature	T	300 K
Radius of gyration	R_g	40 nm
Density	ρ_p	3.5 particles/R_g^3
Average volume fraction	ϕ	$0.11 \rightarrow \rho_p \approx \rho_{\max}/9$
Flory-Huggins parameter	χ	0.5
Number of monomers	p	2700 mon./polymer
Solvent friction	ξ_s	$2.45 \cdot 10^{-9}$ kg/s

Table 6.1: Experimental parameters used to model a polymer solution.

6.3 Systems and model parameters

The RaPiD model as presented in the last section, has a number of parameters and functions that allow the simulation of a large class of materials. Some of the parameters refer to simple experimental conditions, such as temperature and volume fraction of polymer, or molecular properties, such as radius of gyration R_g, the number of Kuhn segments in the polymer, the Flory-Huggins parameter or the solvent friction ξ_s in Eq. (6.9). The radius of gyration R_g is used to define the weight function $\omega(r_{ij})$ in Eq. (6.3). Together these parameters determine the conservative potential, Eq. (6.2), which is responsible for the description of the equilibrium properties of the polymer chains' centers of mass.

In this chapter we have chosen the above parameters such as to describe a polymer solution of high molecular weight PIB (polyisobutylene) in Pristane. The linear and non-linear rheology of this polymer solution have been presented in Ref. [107]. From the materials properties and conditions of the experiment we obtain the parameters listed in Table 6.1. A second class of parameters contains α, τ, λ and ξ_e. Together with $n_0(r_{ij})$ they describe the coupling between the dynamics of the eliminated and retained coordinates. α appears in the transient potential Φ_t and governs the strength of the fluctuations of the entanglement numbers around their equilibrium values and at the same time the strength of the transient forces. The characteristic relaxation time τ (Eq. (6.6)) can, in principle, be estimated from the crossing frequency of the storage $G'(\omega)$ and loss $G''(\omega)$ moduli measured in experiments. However, since in most polymer systems a range of frequencies is observed, which we introduce by

using Eq. (6.7), the crossing frequency only provides a rough estimate of the dominant characteristic time τ_d. Assuming that the radial distribution function between polymers is very close to unity, one may expect that τ_d in the simulation model is the one that corresponds to a separation r that makes $r^2 \exp\{-r/\lambda\}$ a maximum, i.e., $\tau_d = \tau_0 e^{-2}$.

Later in this paper we will use the parameters in this second class as fit parameters that may be adjusted to obtain the best agreement with the experimental results [107]. Before doing so we will investigate the effect of these simulation parameters on the linear rheology using fixed values for the parameters of the first class. Our goal will be to explore the influence of the various parameters on the rheological behavior of polymer solutions. In this part we will restrict ourselves to linear rheology.

All the simulations are performed in cubic boxes with $V = 216\,R_g^3$, containing 756 coarse-grained particles.

6.4 Dependence of the linear rheology on RaPiD parameters

The main observable in this section will be the shear relaxation modulus defined by

$$G(t) = \frac{V}{kT}\langle S_{xy}(t) S_{xy}(0)\rangle, \tag{6.10}$$

where $V = 216\,R_g^3$ is the volume of the simulation box. $S_{xy}(t)$ is the xy component of the stress tensor calculated according to

$$S_{xy}(t) = -\frac{1}{V}\sum_{i,j}(r_{i,x} - r_{j,x})F_{ij,y}, \tag{6.11}$$

with $F_{ij,y}$ denoting the y-component of the force on particle i due to conservative and entanglement interactions with particle j. Storage and loss moduli can be obtained by Fourier transforming $G(t)$, according to

$$G'(\omega) = \omega\int_0^\infty \sin(\omega t)G(t)\mathrm{d}t, \tag{6.12}$$

$$G''(\omega) = \omega\int_0^\infty \cos(\omega t)G(t)\mathrm{d}t. \tag{6.13}$$

6.4.1 Shear relaxation moduli

In Fig. 6.1 we plot $G(t)$ for different values of α, ξ_e, τ_0 and λ. The figure contains three blocks of nine panels. All plots in the upper block are made with $\alpha = 0.1kT$, those in the middle block with $\alpha = 1kT$ and those in the lower block with $\alpha = 10kT$. Within each block the panels are arranged in a matrix such that from left to right τ_0-values are $0.2s$, $2s$ and $20s$ respectively, while from top to bottom ξ_e-values are $10^{-4}\,\mathrm{kgs}^{-1}$, $10^{-6}\,\mathrm{kgs}^{-1}$ and $10^{-8}\,\mathrm{kgs}^{-1}$ respectively. Within each panel we plot three curves pertaining to three different values of λ.

First, consider the influence of α on the form of $G(t)$. In each block with constant α all curves always reach the same maximum value for $G(t)$ at small times, independently of all the other parameters. In some cases with $\lambda = 0.2R_g$ this may seem not to be the case, but further inspection at even lower times indicated that also these curves finally reach the same maximum value as all the others do. As α increases, the maximum value in $G(t)$ increases, indicating an increasing contribution of transient forces to the stress tensor in Eq. (6.11).

Next, we consider the significance of ξ_e on the form of $G(t)$. We observe that the main effect of decreasing ξ_e is a reduction of the time taken for the system to reach low $G(t)$ values, i.e. a shift of the curves to the left. With lower frictions the particles move faster, decreasing the time to de-correlate stress-values. Since the friction does not change the maximum values of the stress tensor, the $G(t)$ values at small times remain the same.

In many cases the system exhibits two pronounced relaxation zones. This is particularly true for the smallest τ_0. In these cases $G(t)$ seems to be a sum of two independent contributions. With constant values of ξ_e the slowest of these contributions is more or less independent of the other variables. Also this contribution is the one which obeys more strictly the rule that it shifts to the left with increasing friction. All these findings point at the same suggestion, that the slowest contribution to $G(t)$ basically comes from the conservative forces. Indeed, removing the transient potential from Eq. (6.8) will make $G(t)$ independent of α, τ and λ. Moreover, assuming that ξ_i may be replaced by some average ξ we will have $G_{\xi'}(t) = G_{\xi''}(t\xi''/\xi')$ for two values ξ' and ξ'' of ξ, explaining the shift of the curves along the horizontal axis.

The second contribution depends on all four parameters considered in this section. It increases with α and it is rather insensitive to the friction. The actual decay depends strongly on τ_0 and λ. When $\lambda = \infty$, i.e., $\tau = \tau_0$ the entanglement contribution to $G(t)$ is very much an

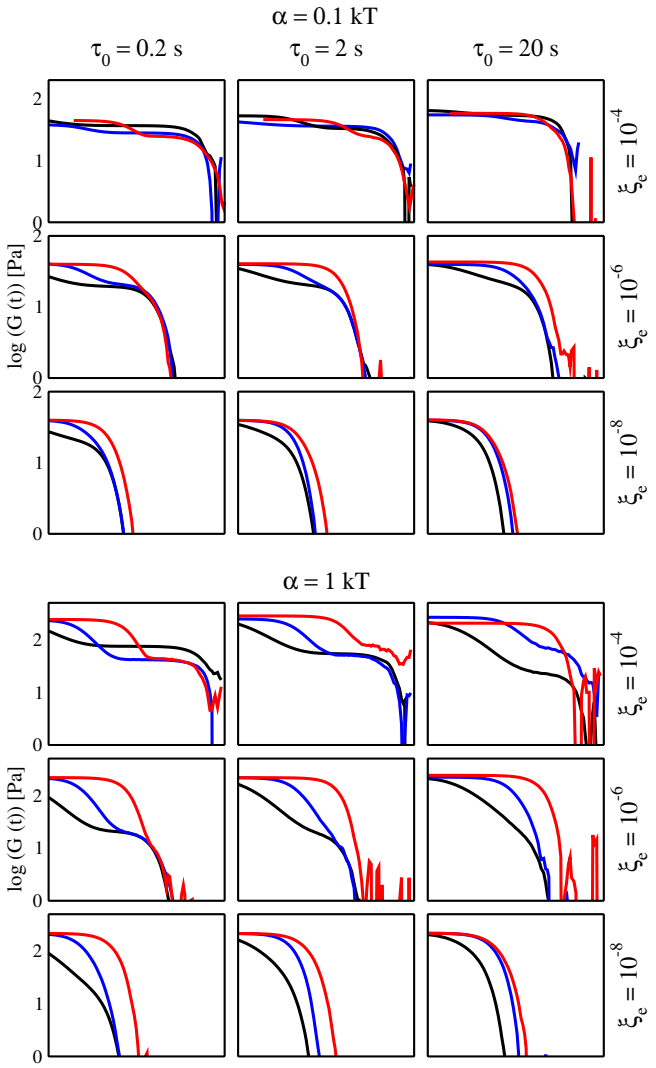

Figure 6.1: (Part A) Stress autocorrelation function $G(t)$ calculated for a set of simulation parameters, as a function of time. On upper panel $\alpha = 0.1\,kT$ and at the lower panel $\alpha = 1\,kT$. The black curves are calculated for $\lambda = 0.2\,R_g$, blue ones for $\lambda = 0.4\,R_g$ and red curves are for constant $\tau = \tau_0$. ξ_e has units of kgs^{-1}.

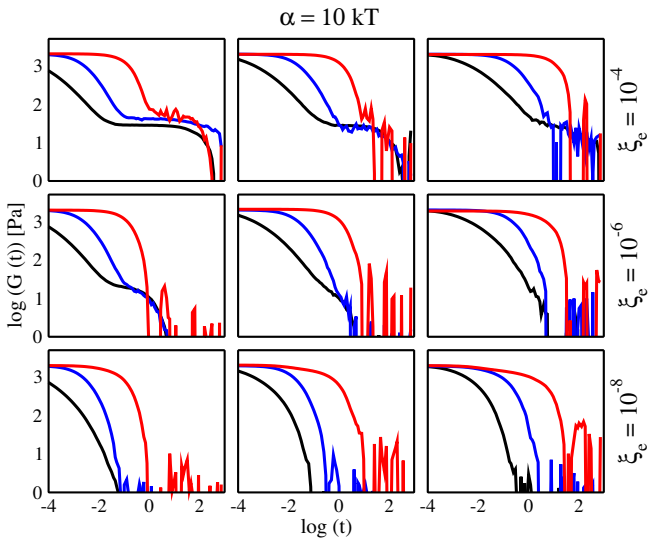

Figure 6.1: (Part B) Stress autocorrelation curves calculated for $\alpha = 10\,kT$ (see description on Fig. 6.1 Part A).

exponentially decaying function. Its decay time is obviously determined by τ_0. Depending on τ_0 and ξ_e either the entanglement or the conservative contributions decays faster. As is clear from its definition, the parameter λ can be used to tune the spectrum of decay times. In Fig. 6.1 we observe that the decay of $G(t)$ becomes less abrupt with decreasing values of λ.

6.4.2 Storage and loss moduli

Experimentally it is much easier to measure in-phase (storage modulus $G'(\omega)$) and out-of-phase (loss modulus $G''(\omega)$) stress-responses to oscillatory deformations, rather than to measure $G(t)$. $G'(\omega)$ provides a measure of the energy stored during one deformation cycle, and $G''(\omega)$ a measure of the energy lost. The usual picture is that at low frequencies the loss modulus increases linearly until it reaches a maximum and begins to decrease. The storage modulus initially increases proportional to the frequency squared and crosses the loss modulus in its maximum, after which it is more or less constant. Several other pictures are possible however, depending on the precise system.

To keep the number of figures in this subsection within limits, we only show a restricted

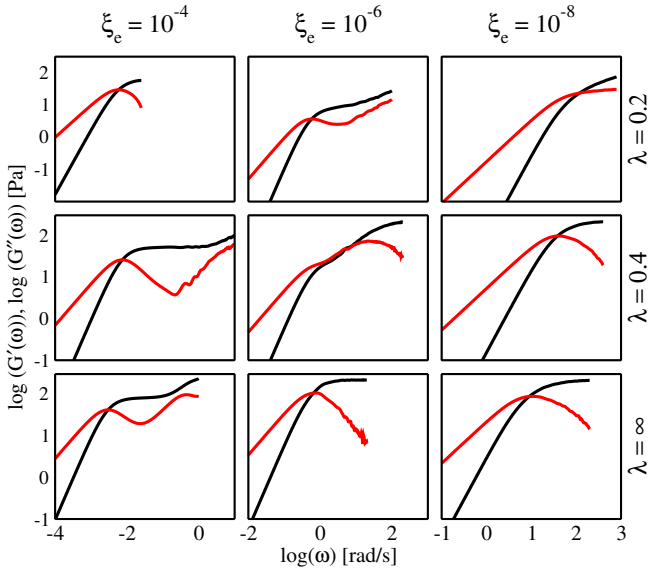

Figure 6.2: $G'(\omega)$ (black) and $G''(\omega)$ (red) curves computed for $G(t)$ functions obtained from simulations with $\alpha = 1\,kT$. The values for ξ_e [kgs^{-1}] and λ [R_g] are given in the top and right side of the picture, respectively. And $\tau_0 = 2\,s$, $\lambda = \infty$ means that τ is always constant.

set of all possible curves in Fig. 6.2 and Fig. 6.3, with the Fourier transform of $G(t)$ calculated according to Eq. (6.12) and Eq. (6.13).

In Fig. 6.2 we present the storage and loss moduli for $\alpha = 1kT$ and $\tau_0 = 2s$, at three different values for ξ_e and three different values of λ. The curves in this figure correspond to those in the middle column of the second block in Fig. 6.1. At low frequencies $G'(\omega) \propto \omega^2$ and $G''(\omega) \propto \omega$, as mentioned above, which comes from the fact that at long times $G(t)$ decays exponentially. The crossing point between $G'(\omega)$ and $G''(\omega)$ is roughly constant for fixed ξ_e, independent of the precise value of λ. By decreasing the friction this point shifts to larger frequencies. The characteristics of the fluid beyond the crossing point strongly depend on the value of λ. So, λ provides a means to tune the viscoelastic properties of the fluid. This is particularly true at intermediate values of the friction. In Fig. 6.3 we consider the effect on $G'(\omega)$ and $G''(\omega)$ of varying α and λ, keeping ξ_e and τ_0 constant. Increasing λ once again modifies the behavior of the curves beyond the crossing point. In addition larger α values shift the crossing point to higher values of ω, while also increasing its modulus.

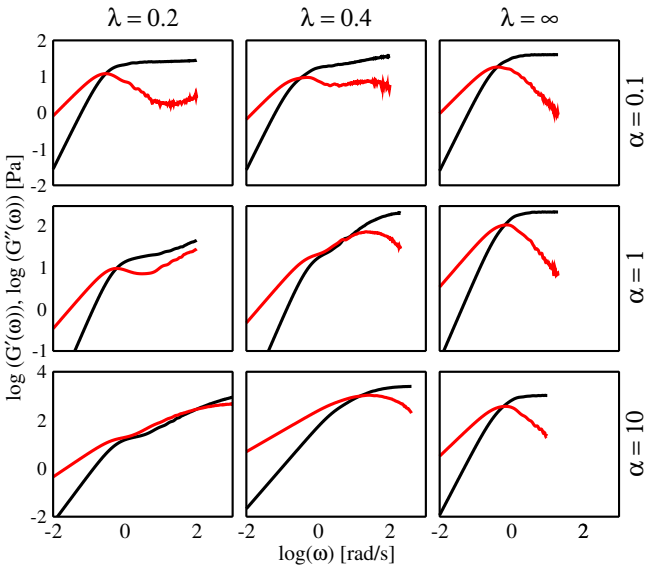

Figure 6.3: $G'(\omega)$ (black) and $G''(\omega)$ (red) calculations for a system with $\xi_e = 10^{-6}\, kgs^{-1}$ and $\tau_0 = 2\, s$, for three values of α [kT] and λ [R_g] parameters.

In Fig. 6.4 (upper graphs) we plot the linear rheology simulation results for a system whose parameters were chosen to give rise to two transitions in the behavior of the storage and loss moduli, indicated by A and B in the graph. The simulation parameters used are listed in the caption of Fig. 6.4. The first transition at crossing point A is interpreted as an evolution from a simple liquid behavior, at low frequencies, to the region where the system starts to present elastic behavior. On increasing the frequency one finds a second transition (point B), to a glassy state. In experiments it is normally a necessity to measure the linear rheology at different temperatures in order to obtain the complete curve as shown here [66]. The results in Fig. 6.4 demonstrate that RaPiD is capable of describing multiple state transitions in the rheology of a fluid through a single simulation run. We also plot in Fig. 6.4 (lower graphs) results for $G(t)$ and its Fourier transform for a system where the rubbery plateau is not observed. For the set of parameters chosen, indicated in the caption of Fig. 6.4, $G''(\omega)$ only becomes smaller than $G'(\omega)$ at higher frequencies, where the system converges to a glassy state.

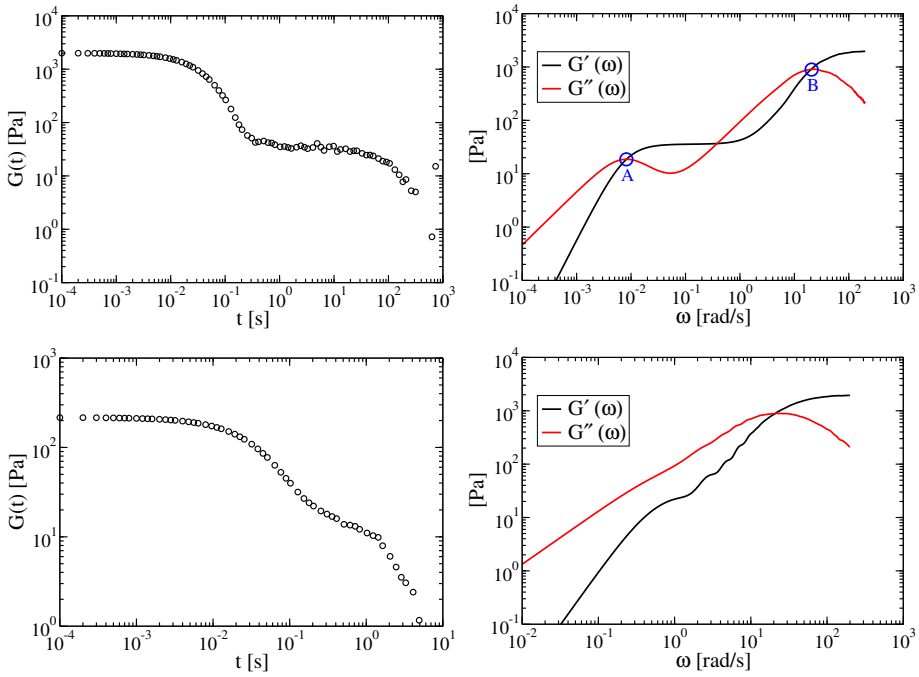

Figure 6.4: Stress autocorrelation function (left), and storage and loss modulus (right). The system parameters for the upper graphs are: $\alpha = 10\,kT$, $\xi_e = 7 \times 10^{-4}\,kg/s$, $\tau_0 = 0.2\,s$ *and* $\lambda = 0.1R_g$. *The points A and B indicate transitions in the fluid's rheology. For the lower graphs we plot the same quantities using the following parameters in the simulations:* $\alpha = 1\,kT$, $\xi_e = 7 \times 10^{-6}\,kg/s$, $\tau_0 = 0.2\,s$ *and* $\lambda = 1.0R_g$.

6.5 Fitting experimental curves

In this section we will use experimental data to exemplify the use of the RaPiD method to simulate the rheology of a viscoelastic fluid. We simulate the polymer solution with parameters described in Table 6.1, which were used to describe the conservative potential. The storage and loss modulus curves for this fluid are known from experimental measurements [107]. We have previously simulated this fluid [102], however in that study we did not tune the parameters to have a perfect agreement with the experiments. Instead, we were only interested in having a qualitative description of a shear-thinning viscoelastic solution. Now we focus on recovering, in the best way possible, the linear rheology of the fluid to gain a better

G_i (Pa)	τ_i (s)
848.36	8.15×10^{-3}
314.24	7.86×10^{-2}
65.80	0.54
2.65	3.71

Table 6.2: Coefficients used to fit the experimental $G'(\omega)$ and $G''(\omega)$ data with the Maxwell model.

understanding of the physical relevance of RaPiD simulation parameters.

From our simulations we obtain the stress auto-correlation function, i.e. $G(t)$. Hence in order to tune the simulation parameters it is easier to compare our results with the experimental $G(t)$ instead of making a detour via $G'(\omega)$ and $G''(\omega)$. We have extracted the "experimental" $G(t)$ by first fitting the experimental $G'(\omega)$ and $G''(\omega)$ with the Maxwell model and next calculating $G(t)$ of the fit. The Maxwell model combines a purely viscous damper and a purely elastic spring connected in series [66], resulting in the description of a viscous-elastic material. Assuming a number of these systems in parallel, known as Generalized Maxwell model, the storage and loss moduli can be computed as

$$G'(\omega) = \sum_{i=1}^{n} \frac{G_i \tau_i^2 \omega^2}{1+\tau_i^2\omega^2}, \tag{6.14}$$

$$G''(\omega) = \sum_{i=1}^{n} \frac{G_i \tau_i \omega}{1+\tau_i^2\omega^2}, \tag{6.15}$$

where G_i and τ_i are fitting parameters defining the strength and relaxation time of the modulus, and n is the number of functions used to fit the data. For the polymer solution we used four functions, the coefficients of which are given in Table 6.2. The shear relaxation modulus is then given by

$$G(t) = \sum_{i=1}^{n} G_i \exp(-t/\tau_i). \tag{6.16}$$

The result is shown, represented by the drawn line, in the upper panel in Fig. 6.5.

Following the trends observed in Section 6.4 on changing the parameters, we now adjust the simulation parameters α, τ_0, λ and ξ_e to obtain the best possible agreement between the simulated and experimental shear relaxation modulus. We have observed in Section 6.4

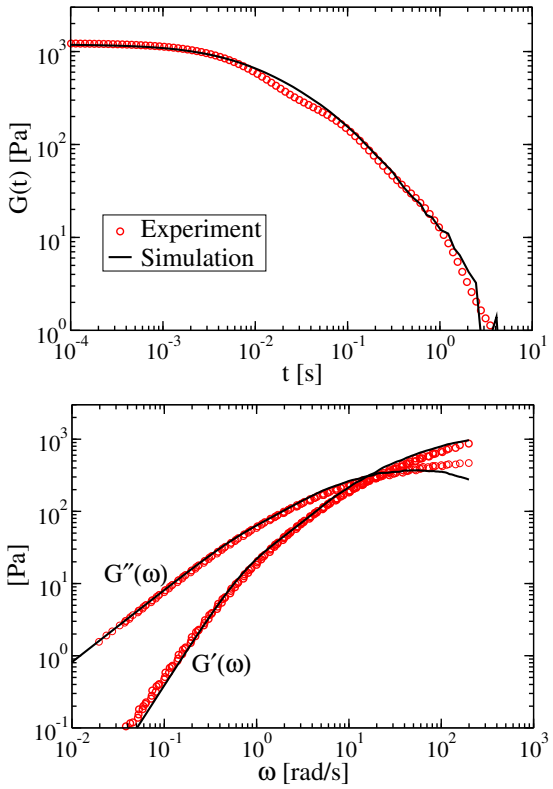

Figure 6.5: Linear rheology of a PIB polymer solution. Red circles are experimental results by Snijkers et al. [107], and black lines the simulation results.

that α is mainly responsible for controlling the maximum value reached by $G(t)$. Therefore, once we had found an α value that reproduces sufficiently well the stress autocorrelation value at small time, we fixed this value and started to tune the other three parameters. We found that $\alpha = 6\,\mathrm{kT}$ reproduces sufficiently well the maximum value of $G(t)$. The use of four exponential functions to represent the experimental $G(t)$ indicates that one single relaxation time is not enough to represent this system. We therefore made use of Eq. (6.7) to describe the relaxation of the entanglement numbers. We adjusted τ_0 and λ to obtain the best qualitative agreement, without giving much attention to possible shifts along the time axis. The friction per entanglement was next adjusted in order to get the correct position along the time axis. The last two steps had to be repeated in order to fine-tune the result. The final parameters so

obtained are $\tau_0 = 4\,\mathrm{s}$, $\lambda = 0.3\,R_g$ and $\xi_e = 6 \times 10^{-6}\,\mathrm{kg/s}$. The simulation result with these parameters is compared with the experimental $G(t)$ curve in Fig. 6.5 upper panel. The lower panel shows the comparison of the simulated storage and loss moduli with curves obtained from experiments.

The steps necessary to fit the linear rheology of a complex fluid using the RaPiD model, and obtain the input parameters required to run the simulations, can be summarized as follow:

1. Obtain a potential describing the equilibrium configuration of the RaPiD particles. The properties of the molecules constituting the fluid should be informed here, e.g., chain length, radius of gyration, etc. And also the conditions of the experiment, such as temperature, density of particles, etc.

2. Usually, only the storage and loss moduli are known experimentally for the liquid to be simulated. In this case, it is better to fit the experimental data with the Maxwell model and obtain the stress autocorrelation to be directly compared with $G(t)$ calculated during the simulations. Have obtained the experimental $G(t)$, the parameter α is tuned in the simulations to get good agreement at small times.

3. After finding α, the parameters τ_0 and λ are adjusted to reproduce the correct decay rate of $G(t)$.

4. The friction per entanglement ξ_e also determines how fast $G(t)$ decays to zero, and can be used to adjust the curve to the correct time scale.

6.6 Predicting non-linear rheology

Having fitted the linear rheology of our fluid, the simulation parameters are now fixed and we can start to make predictions by calculating new properties, like for example non-linear rheological response properties. Here we restrict ourselves to calculating flow curves and Weissenberg numbers as a function of shear rate for the fluid from Section 6.5, and then compare the results with experiments. Flow curves are obtained by calculating the steady-state shear stresses over a range of shear rates according to

$$\eta(\dot{\gamma}) = \frac{S_{xy}(\dot{\gamma})}{\dot{\gamma}}, \tag{6.17}$$

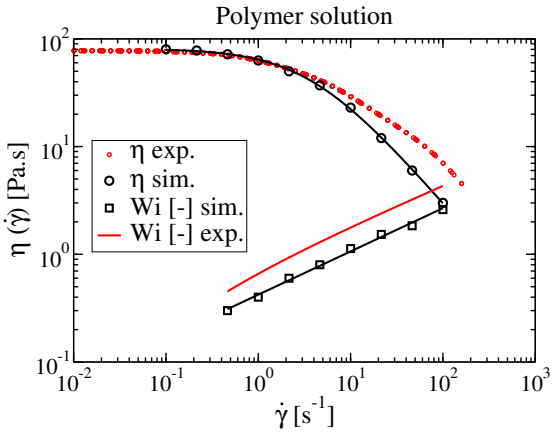

Figure 6.6: Comparison between the simulated shear viscosity and Weissenberg number with experiments for a polymer solution [107].

where S_{xy} is the xy-component of the stress tensor, given by Eq. (6.11), and $\dot{\gamma}$ is the applied shear rate. The Weisseberg number (Wi) is a dimensionless quantity that characterizes the elasticity of the viscoelastic media, and is defined as

$$Wi(\dot{\gamma}) = \frac{N_1(\dot{\gamma})}{S_{xy}(\dot{\gamma})}, \tag{6.18}$$

where $N_1(\dot{\gamma}) = S_{xx}(\dot{\gamma}) - S_{yy}(\dot{\gamma})$ is the first normal stress difference. Simulations are performed using Lees-Edwards boundary conditions [3].

The results are summarized in Fig. 6.6. The simulated shear viscosity has a very good agreement at low shear rates. The shear-thinning behavior of the system is well captured by the simulation, although for higher shear rates the simulated $\eta(\dot{\gamma})$ decays slightly steeper than for the real fluid. The reason for shear thinning in the RaPiD model, and probably also in reality, is that disentangled polymers have no time to entangle with new partners before they have been displaced by the flow far enough to be out of reach. The reason for the slightly too fast shear thinning of the RaPiD model is that the model does not include the possibility for the polymers to deform and elongate, and by doing so have more time to entangle with their instantaneous neighbors. The calculated Weissenberg numbers increase with the same power of shear rate as the experimental results, but they are about 1.6 times smaller than experimental Wi. Also here the lack of possible elongations may be the origin of the difference

between theory and experiment. It is not difficult to imagine ways to include this possibility in the RaPiD model, at the price of course of having a slightly more complicated simulation model. Similar adjustments of the model have been applied in the case of pressure sensitive adhesives [88, 89].

6.7 Conclusions

We investigated the effect of the simulation parameters, responsible to describe the dynamics of the fluids in the RaPiD method, on describing the linear rheology of complex fluids. By analyzing a number of results for the stress autocorrelation function, and storage and loss moduli, we observed that the parameter α, responsible to control the strength of transient forces, can be used to adjust the maximum $G(t)$ value at short times. The friction per entanglement ξ_e and a constant entanglement relaxation time τ determine how long the stresses take to become uncorrelated in the system, showing that the time decreases for smaller parameter values. Non-constant τ have the effect of changing the decay rate of the stress autocorrelation function to zero, and it is an important parameter to tune for modeling the rheological properties of systems with more than one entanglement relaxation time.

In a second part, we exemplify the process of tuning the RaPiD simulation parameters by modeling a particular shear-thinning viscoelastic polymer solution. The fluid is fitted with four terms in the Maxwell model, hence having different relaxation times. We then propose a systematic way of fitting the linear rheology of complex fluids, obtaining the parameters which are not directly known from the system properties.

After we have parameterized the fluid, the input parameters are fixed and we run simulations to obtain shear viscosity and Weissenberg number. The results are compared with experiments, showing a reasonable good agreement with them. The observations obtained here can be used as a reference to model other complex fluids, using the RaPiD simulation method.

Summary

In this thesis we report on simulations of colloidal ordering phenomena in shear-thinning viscoelastic fluids under shear flow. Depending on the characteristics of the fluid, the colloids are observed to align in the direction of the flow. These string-like structures remain stable as long as the shear rate exceeds a critical value. This phenomenon has been subject of study for over 30 years, both theoretically and experimentally, because of to its importance in many technological processes, as for example in the food and cosmetics industry. Nevertheless, the mechanism driving the colloids to the aligned configuration has not yet been elucidated. The goal of this study is to simulate the alignment of colloids during shear flow in polymeric fluids with viscoelastic behavior. A coarse-grained method based on Brownian dynamics was used, where every polymeric chains is modeled as a single particle. With these simulations we are able to obtain new insights and a better understanding for this ordering behavior.

The particle-based simulations are carried out with the Responsive Particle Dynamics (RaPiD) method. In *Chapter 2* the interactions between the RaPiD particles are discussed. A Flory-Huggins potential is developed to describe the conservative interactions between polymeric chains and with the implicit solvent. Transient non-conservative forces are included to qualitative account for dynamical effects resulting from entanglements of the chains. The simulation parameters of the entanglement dynamics are then adjusted to reproduce the rheology of two distinct shear-thinning fluids: a polymer and a wormlike micellar solution. The simulation results obtained for linear and non-linear rheology of both fluids are in reasonable agreement with experiments. After successfully modeling the fluids, colloids are homogeneously dispersed in the suspension media and their distribution is monitored over time. For the stationary fluids, the colloids distribute homogeneously throughout the volume of the simulation box. In the fluid with the rheology of a polymer solution, the colloids remained randomly distributed over the complete range of shear rates analyzed. For the fluid with the flow behavior of a wormlike solution, however, the colloids start to align in the flow direction when the shear rate overcomes a critical value. Once the flow is interrupted, the colloids again distribute over the entire box. These observations are in agreement with experiments in both systems, proving that our model is capable of reproducing the rheology of viscoelastic

fluids and the phenomenon of colloids alignment.

Having defined the potentials and parameters in the RaPiD method to reproduce the colloidal alignment observed in the experiments, they are used in *Chapter 3* to investigate and obtain a deeper understanding of this ordering phenomenon. By varying the simulation parameters we obtained an equation for the critical shear rate beyond which the colloids start to align. This result in principle allows to predict whether the colloids will align in a specific fluid under experimentally achievable shear rates. To be definitive, however, requires additional experiments and simulations of more fluids. The effective interactions between two fixed colloids, and the distribution of the fluid particles around them, were also investigated in this chapter. At low or in zero shear rate there is an increase of the fluid particle density near the colloids; when two colloids are brought close together they repel each other due to the resulting large particle concentration between the two colloids. Upon increasing shear rate, 'wakes' are observed at both side of the colloids, parallel to the flow direction. For two colloids located close to each other in the flow direction, the combined wakes result in a lower particle density between the colloids, which in turn gives rise to an effective attraction between the colloids. In the simulated fluids where no alignment is observed, we found that even for high values of shear rate the flow is not strong enough to deform the distribution of the particles around the colloids. The strength of the transient non-conservative forces is crucial in determining this behavior, since strong restoring forces result in less deformation of the fluid during shear flow.

Motivated by experimental works with colloids bidispersed in size and suspended in viscoelastic fluids, which are observed during shear flow to have a preference for forming strings of colloids with same size only, in *Chapter 4* we used the model fluid where colloids are observed to align in the flow direction (wormlike micellar solution) and added colloids with two distinct sizes. For the stationary fluid and at low shear rates, the colloids distribute homogeneously over the simulation box. Above a critical shear rate, which turns out to be identical to that observed for mono-disperse colloids in Chapters 2 and 3, the colloids again align along the flow direction. But this time the colloids show a tendency to segregate by size, into chains having predominantly colloids with same size. The few experiments presented in the literature on similar systems were performed in rheometers having walls separated by distances slightly larger than the diameter of the larger colloids, hence wall effects could be playing

a role in the alignment and segregation process. Our simulations suggest that segregation is likely to also occurs in the bulk of the fluid, since the simulations have periodic boundary conditions in all three spatial directions. We also investigated the force between pairs of colloids, for pairs with different diameters and pairs of identical size. The results indicate that segregation is mainly caused by stronger attraction between a pair of large colloids, when compared to a pair of small colloids or a pair of unequal colloids. Following the mechanism arrived at in Chapter 3, this stronger attraction can be explained by the larger wakes created by the larger colloids.

In *Chapter 5* the effect of confining walls on the distribution of colloids is investigated. Colloids are observed to migrate towards the walls of the rheometer in shear experiments. It has also been observed that walls can promote alignment close to the walls in fluids where no alignment is observed in the bulk region. To study these effects, we extended the RaPiD method to simulate moving walls that generates a linear flow profile in the confined fluid. In this study we used the fluid with the rheological properties of a polymer solution, as described in Chapter 2, i.e., the fluid that did not give rise to alignment in the bulk. The simulations show that colloids migrate toward the closest wall, in agreement with experiments. Despite the migration to and accumulation at the walls, no alignment could be observed. We expect that further investigations, modeling different fluids, may capture alignment promoted by walls.

In *Chapter 6* we investigate in more detail the effects of the various RaPiD parameters on the fluid's rheology. Analyzing the linear rheology of a model fluid by varying the simulation parameters, we suggest a systematic way of fitting experimental curves using RaPiD simulations. We exemplify the method by fitting the experimental data of a viscoelastic polymer solution. Having defined simulation parameters that reproduce the fluid's linear rheology sufficiently well, the capability of the simulations to predict physical quantities is tested by calculating the non-linear rheology of the fluid. We obtained a relatively good agreement with the experimental variation of shear viscosity and Weissenberg number with shear rate. Suggestions are made on how to improve the agreement. The procedure described in Chapter 6 can be used as a reference to model a large variety of complex fluids, in which the effect of entanglements between the particles constituting the fluid becomes important in the description of the system dynamics.

Samenvatting

In dit proefschrift presenteren we simulaties van colloïdale orderingsfenomenen in vloeistoffen waarvan de viscositeit afneemt onder afschuifstromingen. Afhankelijk van de karakteristieken van de vloeistof kunnen de colloïden in een rijtje gaan liggen in de stroomrichting. Deze colloïdale parelsnoeren blijven stabiel zolang de afschuifstroomsnelheid boven een kritische waarde wordt gehouden. Dit fenomeen wordt al 30 jaar bestudeerd, zowel theoretisch als experimenteel, vanwege de relavantie ervan voor veel technische processen, zoals bijvoorbeeld in de voedsel- en cosmetica-industrie. Desondanks is het mechanisme dat de colloïden naar een opgelijnde toestand drijft nog steeds niet verklaard. Het doel van dit onderzoek is het simuleren van het oplijnen van colloïden onder een afschuifstroming, in oplossingen van keten-achtige moleculen die visco-elastisch gedrag vertonen. Hiervoor wordt een op Brownse dynamica gebaseerde grof-korrelige simulatiemethode gebruikt, waarin elke keten als één deeltje wordt gemodelleerd. Met deze simulaties hebben we nieuwe inzichten verkregen en daarmee een beter begrip van dit orderingsgedrag.

De deeltjessimulaties zijn uitgevoerd met de *Responsive Particle Dynamics* (RaPiD) methode. In *Hoofdstuk 2* worden de interacties tussen de RaPiD deeltjes besproken. Een Flory-Huggins potentiaal is ontwikkeld voor de beschrijving van de conservatieve interacties tussen de polymere ketens en met het impliciete oplosmiddel. Kortstondige niet-conservatieve krachten worden gebruikt om dynamische effecten ten gevolge van verknopingen van de ketens kwalitatief in rekening te brengen. De waardes van de simulatieparameters van de verknopingsdynamica zijn vervolgens gekozen om het reologische gedrag van twee verschillende shear-thinning vloeistoffen te beschrijven: een oplossing van polymeren en een oplossing van worm-vormige micellen. De simulatieresultaten voor de lineaire en niet-lineaire reologie van beide vloeistoffen zijn in redelijke overeenstemming met de experimentele data. Na deze succesvolle simulatie van de vloeistoffen zijn colloïden homogeen verdeeld over de vloeistoffen, om hun distributies in de tijd te volgen. In stationaire vloeistoffen blijken de colloïden zich homogeen te verdelen over het volume van de simulatiedoos. In de vloeistof met het reologisch gedrag van een polymeeroplossing blijven de colloïden willekeurig verdeeld voor de hele serie van gebruikte afschuifstroomsnelheden. In

de vloeistof met het stromingsgedrag van een oplossing van worm-achtige micellen, daarentegen, beginnen de colloïden rijtjes te vormen in de stromingsrichting zodra de afschuifstroomsnelheid een kritische waarde overschrijdt. Als de stroming wordt onderbroken verspreiden de colloïden zich weer over de hele doos. Deze observaties zijn in overeenstemming met de experimenten in deze twee vloeistoffen, waaruit volgt dat ons model geschikt is voor simulaties van de reologie van visco-elastische vloeistoffen en van het colloïdale orderingsfenomeen.

De potentialen en parameters waarmee RaPiD het experimentele oplijnen van colloïden reproduceert worden in *Hoofdstuk 3* gebruikt om het oplijningsgedrag te onderzoeken en een dieper inzicht te verkrijgen. Door de simulatiesparameters te variëren vinden we een uitdrukking voor de kritische afschuifstroomsnelheid waarboven de colloïden beginnen op te lijnen. Dit resultaat maakt het, in principe, mogelijk om te voorspellen of colloïden in rijtjes zullen gaan liggen in een speficieke vloeistof onder experimenteel haalbare afschuifstroomsnelheden. Om hier zekerheid over te krijgen vereist aanvullende experimenten en simulaties van meerdere vloeistoffen. De effectieve interacties tussen twee gefixeerde colloïden, en de omringende verdelingen van vloeistofdeeltjes, worden ook bestudeerd in dit hoofdstuk. Voor lage afschuifstroomsnelheden is de deeltjesdichtheid hoger nabij de colloïden; wanneer twee colloïden naar elkaar worden gebracht zullen ze elkaar afstoten door de resulterende hoge deeltjesconcentratie tussen de twee colloïden. Met toenemede afschuifstroomsnelheid wordt een 'kielzog' waargenomen aan beide zijdes van de colloïden, parallel aan de stroomrichting. Voor twee colloïden die dicht naast elkaar liggen in de stroomrichting leidt de combinatie van kielzoggen tot een gereduceerde deeltjesdichtheid tussen de colloïden, met als gevolg een effectieve aantrekkingskracht tussen de colloïden. In de gesimuleerde vloeistoffen waarin geen oplijning plaatsvond blijkt dat, zelfs voor de hoogste afschuifstroomsnelheden, de stroming niet sterk genoeg is om de verdeling van vloeistofdeeltjes rond de colloïden te verstoren. De sterkte van de kortstondige niet-conservatieve krachten is van doorslaggevend belang voor dit gedrag, omdat sterke terugdrijvende krachten leiden tot minder deformatie van de vloeistof onder een afschuifstroming.

Gemotiveerd door experimenten met colloïdale deeltjes van twee verschillende groottes opgelost in visco-elastische vloeistoffen, die onder afschuifstroming snoeren blijken te vormen van colloïden met dezelfde grootte, worden in *Hoofdstuk 4* simulaties beschreven van

colloïdale mengsels in de vloeistof met het reologische gedrag van de oplossing van wormachtige micellen. In de stationaire vloeistof en onder lage afschuifstroomsnelheden verdelen de colloïden zich homogeen over de simulatiedoos. Boven een kritische afschuifstroomsnelheid, die identiek blijkt te zijn aan die voor mono-disperse colloïden in Hoofdstukken 2 en 3, vormen de colloïden wederom snoeren in de stroomrichting. Maar dit keer vertonen de colloïden een neiging om naar grootte te scheiden, tot ketens met voornamelijk colloïden van dezelfde grootte. De weinige experimenten aan vergelijkbare systemen in de literatuur werden uitgevoerd in reometers met spleetbreedtes nauwelijks groter dan de diameter van de grootste colloïden, waardoor wandeffecten een rol kunnen hebben gespeeld in de oplijnings- en scheidingsprocessen. Onze simulaties suggereren dat scheiding waarschijnlijk ook in de bulk van een vloeistof plaats kan vinden, omdat de simulaties gebruik maken van periodieke randvoorwaarden in alle drie ruimtelijke richtingen. We hebben ook de kracht tussen colloïdparen onderzocht, voor paren met verschillende diameters en voor paren met gelijke afmetingen. De resultaten geven aan dat segregatie voornamelijk veroorzaakt wordt door de sterkere attractie tussen een paar grote colloïden, in vergelijking met een paar kleine colloïden en een paar van ongelijke colloïden. In lijn met het mechanisme beschreven in Hoofdstuk 3 kan deze sterkere attractie verklaard worden door de grotere kielzoggen van de grote deeltjes.

In *Hoofdstuk 5* wordt het effect van insluitende wanden op de verdeling van colloïden bestudeerd. Colloïden blijken in experimentele afschuifstromingen naar de wanden van de reometer te migreren. Ook is waargenomen dat colloïden nabij wanden snoeren kunnen vormen in vloeistoffen die geen snoervorming vertonen in de bulk. Om deze effecten te bestuderen hebben we de RaPiD methode uitgebreid om bewegende wanden te kunnen simuleren, die een lineair stromingsveld genereren in de ingesloten vloeistof. Voor deze studie gebruiken we de vloeistof met het reologisch gedrag van een polymeeroplossing, zie Hoofdstuk 2, d.w.z. een vloeistof waarin de colloïden niet ordenen in de bulk. In de simulaties blijken de colloïden naar de dichtsbijzijnde wand te migreren, in overeenstemming met de experimenten. Ondanks de migratie naar en verzameling bij de wanden was er geen oplijning waarneembaar. We verwachten dat vervolgsimulaties, met andere vloeistoffen, wel aanleiding zullen geven tot snoervorming aan de wand.

In *Hoofdstuk 6* onderzoeken we in meer detail de effecten van de verschillende RaPiD

parameters op de reologie van de vloeistof. Door te analyseren hoe de lineaire reologie van de simulatievloeistof afhangt van de simulatieparameters komen we tot een systematische methode om de experimentele curves te vertalen naar RaPiD parameters. Als voorbeeld hebben we de experimentele data van een visco-elastische polymeeroplossing gebruikt. Na het vaststellen van simulatieparameters die de lineaire reologie van de vloeistof voldoende nauwkeurig beschrijven, is onderzocht of dit model accurate voorspellingen geeft voor de niet-lineaire reologie van deze vloeistof. We vinden een relatief goede overeenstemming met de experimentele viscositeit en Weissenberg getal als functies van de afschuifstroomsnelheid. Suggesties voor verbeteringen worden gegeven. De procedure beschreven in Hoofdstuk 6 kan gebruikt worden als een leidraad bij het modelleren van een scala van complexe vloeistoffen, waarin de effecten van verknopingen tussen de vloeistofdeeltjes belangrijk zijn voor een correcte beschrijving van de dynamica.

Acknowledgment

I am greatly indebted and very grateful to Prof. Wim Briels, my supervisor, for his expert guidance, patience, support and friendly encouragement throughout my Ph.D. studies.

I would like to thank Dr. Johan Padding for introducing me to the simulation method used in this work. I also want to give many thanks to Dr. Wouter den Otter, for his daily help in finding solutions for the most diverse problems, always pointing to new directions for my project and for his carefully revision of the manuscripts. And I want to thank Prof. Jan Vermant for providing experimental data, which were essential for the development of this work.

I also would like to acknowledge all the Ph.D. students and pos-docs with whom I had contact during these years. Alessandra, Barry, Gabriel, Ioana, Li and Tom, thank you for listening to my presentations, reading my manuscripts and always making good suggestions. And also by the dinners and beers together in our spare time, including there also the BES members, Csaba, Riccardo and Omar.

I wish to thank my parents for their never-ending support, even being far away from here.

Finally, and most importantly, I would like to give special thanks to my wife Heloisa, for being with me all the time and giving me constant support.

About the author

Igor Santos de Oliveira was born on the 5^{th} of January in 1983 in Monte Alegre de Minas - MG, Brazil. In 2002 he was admitted to the Federal University of Uberlândia, where four years later he earned his degree in Physics. On the same year he started his Master study on the subject of *ab initio* calculations of impurities in SiC nanowires, supervised by Prof. Roberto Hiroki Miwa, at the same University. Then, he was accepted to the Erasmus Mundus AtoSiM (Atomic Scale Modelling of Physical, Chemical, and Biomolecular Systems) master, at the École Normale Supérieure de Lyon, France. His research project was carried out in the Università di Roma, Italy, about the crystal stability of diblock copolymer micelles in solution, under supervision of Prof. Carlo Pierleoni. In 2008 he joined the Computational Biophysics group at the University of Twente, the Netherlands, and started his Ph.D. research on the investigation of colloidal alignment in sheared viscoelastic fluids, under supervision of Prof. Wim Briels.

List of publications

- **Chapter 2:** I. S. Santos de Oliveira, A. van den Noort, J. T. Padding, W. K. den Otter and W. J. Briels,
  Alignment of particles in sheared viscoelastic fluids,
  J. Chem. Phys., **135**, 104902, 2011.

- **Chapter 3:** I. S. Santos de Oliveira, W. K. den Otter and W. J. Briels,
  The origin of flow-induced alignment of spherical colloids in shear-thinning viscoelastic fluids,
  accepted for publication in the Journal of Chemical Physics, 2012.

- **Chapter 4:** I. S. Santos de Oliveira, W. K. den Otter and W. J. Briels,
  Alignment and segregation of bidispersed colloids in a shear-thinning viscoelastic fluid under shear flow,
  submitted to the Europhysics Letters, 2012.

- **Chapter 5:** I. S. Santos de Oliveira, W. K. den Otter and W. J. Briels,
  Shear-induced colloids migration in a confined shear-thinning viscoelastic fluid,
  in preparation.

- **Chapter 6:** I. S. Santos de Oliveira, W. K. den Otter and W. J. Briels,
  Exploring RaPiD simulation parameters in the modeling of complex fluids,
  in preparation.

- I. S. Santos de Oliveira and R. H. Miwa,
  Boron and nitrogen impurities in SiC nanowires,
  Phys. Rev. B, **79**, 85427, 2009.

- J. J. Molina, C. Pierleoni, B. Capone, I. S. Santos de Oliveira and J. P. Hansen,
  Crystal stability of diblock copolymer micelles in solution,
  Mol. Phys., **107**, 535, 2009.

Bibliography

[1] R. L. C. Akkermans and W. J. Briels. Coarse-grained interactions in polymer melts: a variational approach. *J. Chem. Phys.*, 115:6210–6219, 2001.

[2] B. J. Alder and T. E. Wainwright. Studies in molecular dynamics. i. general method. *J. Chem. Phys.*, 31:459, 1959.

[3] M. P. Allen and D. J. Tildesley. *Computer Simulations of Liquids*. Oxford University Press, Oxford, U. K., 1987.

[4] A. M. Ardekani, R. H. Rangel, and D. D. Joseph. Two spheres in a free stream of a second-order fluid. *Physics of Fluids*, 20:063101, 2008.

[5] M. M. H. D. Arntz, W. K. den Otter, H. H. Beeftink, R. M. Boom, and W. J. Briels. Repeated segregation and energy dissipation in an axially segregated granular bed. *Europhys. Lett.*, 92:54004, 2010.

[6] E. S. Asmolov. The inertial lift on a spherical particle in a plane poiseuille flow at large channel reynolds number. *J. Fluid Mech.*, 381:63, 1999.

[7] E. S. Asmolov and A. A. Osiptsov. The inertial lift on a spherical particle settling in a horizontal viscous flow through a vertical slot. *Phys. Fluids*, 21:063301, 2009.

[8] A. A. S. Bhagat, S. S. Kuntaegowdanahalli, and I. Papautsky. Enhanced particle filtration in straight microchannels using shear-modulated inertial migration. *Phys. Fluids*, 20:101702, 2008.

[9] H. Binous and R. J. Phillips. Dynamic simulation of one and two particles sedimenting in viscoelastic suspensions of FENE dumbbells. *J. Non-Newtonian Fluid Mech.*, 83:93–130, 1999.

[10] A. Böker, J. He, T. Emrick, and T. P. Russel. Self-assembly of nanoparticles at interfaces. *Soft Matter*, 3:1231–1248, 2007.

[11] P. G. Bolhuis and A. A. Louis. How to derive and parameterize effective potentials in colloid-polymer mixtures. *Macromolecules*, 35:1860–1869, 2002.

[12] P. G. Bolhuis, A. A. Louis, and J. P. Hansen. Accurate effective pair potentials for polymer-solutions. *J. Chem. Phys.*, 114:4296, 2001.

[13] W. J. Briels. *Theory of Polymer Dynamics, lecture notes*. It can be downloaded from: http://cbp.tnw.utwente.nl/PolymeerDictaat, Enschede, The Netherlands, 1998.

[14] W. J. Briels. Transient forces in flowing soft matter. *Soft Matter*, 5:4401–4411, 2009.

[15] A. Bymaster, S. Jain, and W. G. Chapman. Microstructure and depletion forces in polymer-colloid mixtures from an interfacial statistical associating fluid theory. *J. Chem. Phys.*, 128:164910, 2008.

[16] D. D. Carlo, J. F. Edd, K. J. Humphry, H. A. Stone, and M. Toner. Particle segregation and dynamics in confined flows. *Phys. Rev. Lett.*, 102:094503, 2009.

[17] S. Caserta, G. D'Avino, F. Greco, S. Guido, and P. L. Maffettone. Migration of a sphere in a viscoelastic fluid under planar shear flow: Experiments and numerical predictions. *Soft Matter*, 7:1100–1106, 2011.

[18] M. E. Cates and S. J. Candau. Statics and dynamics of worm-like surfactant micelles. *J. Phys.: Condens. Matter*, 2:6869–6892, 1990.

[19] M. M. Cross. Rheology of non-newtonian fluids: a new flow equation for pseudoplastic systems. *J. Colloid Sci.*, 20:417–437, 1965.

[20] G. D'Avino, G. Cicale, M. A. Hulsen, F. Greco, and P. L. Maffetone. Effects of confinement on the motion of a single sphere in a sheared viscoelastic liquid. *J. Non-Newtonian Fluid Mech.*, 157:101–107, 2009.

[21] G. D'Avino, M. A. Hulsen, F. Snijkers, J. Vermant, F. Greco, and P. L. Maffetone. Rotation of a sphere in a viscoelastic liquid subjected to shear flow. Part I: Simulation results. *J. Rheol.*, 52:1331–1346, 2008.

[22] G. D'Avino, P. L. Maffetone, F. Greco, and M. A. Hulsen. Viscoelasticity-induced migration of a rigid sphere in confined shear flow. *J. Non-Newtonian Fluid Mech.*, 165:466–474, 2010.

[23] G. D'Avino, F. Snijkers, R. Pasquino, M. A. Hulsen, F. Greco, P. L. Maffettone, and J. Vermant. Migration of a sphere suspended in viscoelastic liquids in couette flow: experiments and simulations. *Rheol. Acta*, 51:215–234, 2012.

[24] G. D'Avino, T Tuccillo, P. L. Maffetone, F. Greco, and M. A. Hulsen. Numerical simulations of particle migration in a viscoelastic fluid subjected to shear flow. *Comput. Fluids*, 39:709–721, 2010.

[25] J. M. Deutch and I. Oppenheim. Molecular theory of Brownian motion for several particles. *J. Chem. Phys.*, 54:3547–3555, 1971.

[26] M. Doi and S. F. Edwards. *The Theory of Polymers Dynamics*. Oxford Science Publications, Oxford, U. K., 1986.

[27] M. Doxastakis, Y-L. Chen, and J. J. de Pablo. Potential of mean force between two nanometer-scale particles in a polymer solution. *J. Chem. Phys.*, 123:034901, 2005.

[28] M. Doxastakis, Y-L. Chen, O. Guzmán, and J. J. de Pablo. Polymer-particle mixtures: Depletion and packing effects. *J. Chem. Phys.*, 120:9335, 2004.

[29] C. A. Dreiss. Womlike micelles: where do we stand? Recent developments, linear rheology and scattering techniques. *Soft Matter*, 3:956–970, 2007.

[30] B. Dünweg and A. J. C. Ladd. Lattice boltzmann simulations of soft matter systems. *Adv. Polym. Sci.*, 221:89, 2009.

[31] P. Español and P. B. Warren. Statistical mechanics of dissipative particle dynamics. *Europhys. Lett.*, 30:191, 1995.

[32] S. Ezrahi, E. Tuval, and A. Aserin. Properties, main applications and perspectives of worm micelles. *Adv. Colloid Interface Sci.*, 128:77–102, 2007.

[33] J. Feng, H. H. Hu, and D. D. Joseph. Direct simulation of initial values problems for the motion of solid bodies in a newtonian fluid, part ii: Couette and poiseuille flows. *J. Fluid Mech.*, 277:271, 1974.

[34] J. Feng, P. Y. Huang, and D. D. Joseph. Dynamic simulation of sedimentation of solid particles in an Oldroyd-B fluid. *J. Non-Newtonian Fluid Mech.*, 63:63–88, 1996.

[35] M. Fialkowski, K. J. M. Bishop, R. Klajn, S. K. Smoukov, C. J. Campbell, and B. A. Grzybowski. Self-assembly at all scales. *J. Phys. Chem. B*, 110:2482–2496, 2006.

[36] P. J. Flory. Thermodynamics of high polymer solutions. *J. Chem. Phys.*, 10:51–61, 1942.

[37] F. Gauthier, H. L. Goldsmith, and S. G. Mason. Particle motions in non-newtonian media. ii. poiseuille flow. *Rheol. Acta*, 10:344, 1971.

[38] H. Giesekus. Die bewegung von teilchen in strömungen nicht-newtonscher flußsigkeiten. *Z. Angew. Math. Mech.*, 58:T26–T37, 1978.

[39] G. Gompper, T. Ihle, K. Kroll, and Winkler. R. G. Multi-particle collision dynamics: A particle-based mesoscale simulation approach to the hydrodynamics of complex fluids. *Adv. Polym. Sci.*, 221:1, 2009.

[40] M. Grzelczak, J. Vermant, E. M. Furst, and L. M. Liz-Marzán. Directed self-assembly of nanoparticles. *Acs Nano*, 4:3591–3605, 2010.

[41] I. W. Hamley. *Introduction to Soft Matter - Synthetic and Biological Self-Assembling Materials*. Jonh Wiley & Sons, England, 2007.

[42] M. Han, C. Kim, M. Kim, and S. Lee. Particle migration in tube flow of suspensions. *J. Rheol.*, 43:1157, 1999.

[43] O. G. Harlen. The negative wake behind a sphere sedimenting through a viscoelastic fluid. *J. Non-Newtonian Fluid Mech.*, 108:411–430, 2002.

[44] D. J. Highgate and R. W. Whorlow. End effects and particle migration effects in concentric cylinder rheometry. *Rheol. Acta*, 8:142–151, 1969.

[45] D. J. Highgate and R. W. Whorlow. Rheological properties of suspensions of spheres in non-newtonian media. *Rheol. Acta*, 9:569–576, 1970.

[46] B. Ho and L. Leal. Inertial migration of rigid spheres in 2-dimensional unidirectional flows. *J. Fluid Mech.*, 65:365–400, 1974.

[47] B. P. Ho and L. G. Leal. Migration of rigid spheres in a 2-dimensional unidirectional shear-flow of a 2nd-order fluid. *J. Fluid Mech.*, 76:783–799, 1976.

[48] P. J. Hoogerbrugge and J. M. V. A. Koelman. Simulating microscopic hydrodynamic phenomena with dissipative particle dynamics. *Europhys. Lett.*, 19:155, 1992.

[49] P. Y. Huang, J. Feng, H. H. Hu, and D. D. Joseph. Direct simulation of the motion of solid particles in couette and poiseuille flows of viscoelastic fluids. *J. Fluid Mech.*, 343:73–94, 1997.

[50] P. Y. Huang and D. D. Joseph. Effects of shear thinning on migration of neutrally buoyant particles in pressure driven flow of newtonian and viscoelastic fluids. *J. Non-Newtonian Fluid Mech.*, 90:159, 2000.

[51] M. L. Huggins. Solutions of long chain compounds. *J. Chem. Phys.*, 9:440, 1941.

[52] W. Humphrey, A. Dalke, and K. Schulten. Vmd - visual molecular dynamics. *J. Molec. Graphics*, 14:33–38, 1996.

[53] W. R. Hwang and M. A. Hulsen. Structure formation of non-colloidal particles in viscoelastic fluids subjected to simple shear flow. *Macromol. Mater. Eng.*, 296:321–330, 2011.

[54] W. R. Hwang, M. A. Hulsen, and E. H. Meijer. Direct simulations of particle suspensions in a viscoelastic fluid in sliding bi-periodic frames. *J. Non-Newtonian Fluid Mech.*, 121:15–33, 2004.

[55] A. Hynninen and M. Dijkstra. Phase diagram of dipolar hard and soft spheres: Manipulation of colloidal crystal structures by an external field. *Phys. Rev. Lett.*, 94:138303, 2005.

[56] M. A. Jefri and A. H. Zahed. Elastic and viscous effects on particle migration in plane-poiseuille flow. *J. Rheol.*, 33:691, 1989.

[57] D. Joseph, T. Funada, and J. Wang. *Potential flows of viscous and viscoelastic fluids*. Cambridge University Press, New York, U.S.A., 2008.

[58] D. D. Joseph, Y. J. Liu, M. Poletto, and J. Feng. Aggregation and dispersion of spheres falling in viscoelastic liquids. *J. Non-Newtonian Fluid Mech.*, 54:45, 1994.

[59] A. Kamis and S. G. Mason. Particle motions in sheared suspensions. xix. viscoelastic media. *Transactions of the Society of Rheology*, 10:571–592, 1966.

[60] C. Kim. Migration in concentrated suspensions of spherical particles dispersed in polymer solution. *Korea-Australia Rheol. J.*, 12:19, 2001.

[61] J. M. Kim, S. G. Lee, and C. Kim. Numerical simulations of particle migration in suspension flows: Frameinvariant formulation of curvature-induced migration. *J. Non-Newtonian Fluid Mech.*, 150:162, 2008.

[62] Y. W. Kim and J. Y. Yoo. The lateral migration of neutrally-buoyant spheres transported through square microchannels. *J. Micromech. Microeng.*, 18:065015, 2008.

[63] P. Kindt and W. J. Briels. A single particle model to simulate the dynamics of entangled polymer melts. *J. Chem. Phys.*, 127:134901, 2007.

[64] P. Kindt and W. J. Briels. The role of entanglements on the stability of microphase separated diblock copolymers in shear flow. *J. Chem. Phys.*, 128:124901, 2008.

[65] J. M. V. A. Koelman and P. J. Hoogerbrugge. Dynamic simulation of hard sphere suspensions under steady shear. *Europhys. Lett.*, 21:363, 1993.

[66] R. G. Larson. *The Structure and Rheology of Complex Fluids*. Oxford University Press, Oxford, U. K., 1999.

[67] Z. Li and J. Wu. Potential distribution theorem for the polymer-induced depletion between colloidal particles. *J. Chem. Phys.*, 126:144904, 2007.

[68] C. N. Likos. Effective interactions in soft condensed matter physics. *Physics Reports*, 348:267–439, 2001.

[69] C. N. Likos, H. Löwen, M. Watzlawek, B. Abbas, O. Jucknischke, J. Allgaier, and Richter D. Star polymers viewed as ultrasoft colloidal particles. *Phys. Rev. Lett.*, 80:4450, 1998.

[70] Y. J. Liu, J. Nelson, J. Feng, and D. D. Joseph. Anomalous rolling of spheres down an inclined plane. *J. Non-Newtonian Fluid Mech.*, 50:305, 1993.

[71] B. M. Lormand and R. J. Phillips. Sphere migration in oscillatory couette flow of a viscoelastic fluid. *J. Rheol.*, 48:551, 2004.

[72] M. K. Lyon, D. W. Mead, R. E. Elliott, and L. G. Leal. Structure formation in moderately concentrated viscoelastic suspensions in simple shear flow. *J. Rheol.*, 45:881–890, 2001.

[73] A. Malevanets and R. Kapral. Mesoscopic model for solvent dynamics. *J. Chem. Phys.*, 110:8605, 1999.

[74] A. Malevanets and R. Kapral. Solute dynamics in mesoscale solvent. *J. Chem. Phys.*, 112:7260, 2000.

[75] A. Ya. Malkin, A. V. Semakov, and V. G. Kulichikhin. Self-organization in the flow of complex fluids (colloid and polymer systems). Part 1: Experimental evidence. *Adv. Colloid Interface Sci.*, 157:75–90, 2010.

[76] J. M. Manski, A. J. van der Goot, and R. M. Boom. Advances in structure formation of anisotropic protein-rich foods through novel processing concepts. *Trends Food Sci. Technol.*, 18:546–557, 2007.

[77] L. M. Martyushev and V. D. Seleznev. Maximum entropy production principles in physics, chemistry and biology. *Phys. Rep.*, 426:1, 2006.

[78] J. P. Matas, J. F. Morris, and E. Guazzelli. Inertial migration of rigid spherical particles in poiseuille flow. *J. Fluid Mech.*, 515:171, 2004.

[79] V. G. Mavrantzas, T. D. Boone, E. Zervopoulou, and D. N. Theodorou. End-bridging Monte Carlo: a fast algorithm for atomistic simulation of condensed phases of long polymer chains. *Macromolecules*, 32:5072–5096, 1999.

[80] P. Mazur and I.7 Oppenheim. Molecular theory of Brownian motion. *Physica*, 50:241–258, 1970.

[81] N. Metropolis, A. W. Rosenbluth, M. N. Rosenbluth, Teller A. H., and E. Teller. Equation of state calculations by fast computing machines. *J. Chem. Phys.*, 21:1087, 1953.

[82] J. Michele, R. Patzold, and R. Donis. Alignment and aggregation effects in suspensions of spheres in non-newtonian media. *Rheol. Acta*, 16:317–321, 1977.

[83] Nanodirect. http://nanodirect.eu/nanodirect.html.

[84] H. C. Öttinger. *Stochastic Processes in Polymeric Fluids - Tools and Examples for Developing Simulation Algorithms*. Springer, Berlin, Germany, 1996.

[85] H. C. Öttinger. *Beyond Equilibrium Thermodynamics*. Wiley-Interscience, Hoboken, N.J., 2005.

[86] J. T. Padding, E. S. Boek, and W. J. Briels. Dynamics and rheology of wormlike micelles emerging from particulate computer simulations. *J. Chem. Phys.*, 129:074903, 2008.

[87] J. T. Padding and W. J. Briels. Systematic coarse-graining of the dynamics of entangled polymer melts: the road from chemistry to rheology. *J. Phys.: Condens. Matter*, 23:233101, 2011.

[88] J. T. Padding, L. V. Mohite, D. Auhl, W. J. Briels, and C. Bailly. Mesoscale modeling of the rheology of pressure sensitive adhesives through inclusion of transient forces. *Soft Matter*, 7:5036–5046, 2011.

[89] J. T. Padding, L. V. Mohite, D. Auhl, T. Schweizer, W. J. Briels, and C. Bailly. Quantitative mesoscale modeling of the oscillatory and transient shear rheology and the extensional rheology of pressure sensitive adhesives. *Soft Matter*, 8:7967–7981, 2012.

[90] J. T. Padding, E. van Ruymbeke, D. Vlassopoulos, and W. J. Briels. Computer simulation of the rheology of concentrated star polymer suspensions. *Rheol. Acta*, 49:473–484, 2010.

[91] I. Pagonabarraga and D. Frenkel. Dissipative particle dynamics for interacting systems. *J. Chem. Phys.*, 115:5015–5026, 2001.

[92] R. Pasquino, F. Snijkers, N. Grizzutti, and J. Vermant. Directed self-assembly of spheres into a two-dimensional colloidal crystal by viscoelastic stresses. *Langmuir*, 26:3016–3019, 2010.

[93] R. Pasquino, F. Snijkers, N. Grizzutti, and J. Vermant. The effect of particle size and migration on the formation of flow-induced structures in viscoelastic suspensions. *Rheol. Acta*, 49:993–1001, 2010.

[94] N. A. Patankar and H. H. Hu. Rheology of a suspension of particles in viscoelastic fluids. *J. Non-Newtonian Fluid Mech.*, 96:427–443, 2000.

[95] N. A. Patankar and H. H. Hu. Rheology of a suspension of particles in viscoelastic fluids. *J. Non-Newtonian Fluid Mech.*, 96:427–443, 2001.

[96] L. Petit and B. Noetinger. Shear-induced structures in macroscopic dispersions. *Rheol. Acta*, 27:437–441, 1988.

[97] R. J. Phillips and L. Talini. Chaining of weakly interacting particles suspended in viscoelastic fluids. *J. Non-Newtonian Fluid Mech.*, 147:175–188, 2007.

[98] M. Reiner. The deborah number. *Physics Today*, January:62, 1964.

[99] W. B. Russel, D. A. Saville, and W. R. Schowalter. *Colloidal Dispersions*. Cambridge University Press, England, 1989.

[100] P. G. Saffman. Lift on a small sphere in a slow shear flow. *J. Fluid Mech.*, 22:385, 1965.

[101] I. S. Santos de Oliveira, W. K. den Otter, and W. J. Briels. The origin of flow-induced alignment of spherical particles in shear-thinning viscoelastic fluids. *accepted for publication on the J. Chem. Phys.*, 2012.

[102] I. S. Santos de Oliveira, A. van den Noort, J. T. Padding, W. K. den Otter, and W. J. Briels. Alignment of particles in sheared viscoelastic fluids. *J. Chem. Phys.*, 135:104902, 2011.

[103] R. Scirocco, J. Vermant, and J. Mewis. Effect of the viscoelasticity of the suspending fluid on structure formation in suspensions. *J. Non-Newtonian Fluid Mech.*, 117:183–192, 2004.

[104] G. Segré and A. Silberberg. Radial particle displacements in poiseuille flow of suspensions. *Nature*, 189:209–210, 1961.

[105] G. Segré and A. Silberberg. Behaviour of macroscopic rigid spheres in poiseuille flow. 2. experimental results and interpretation. *J. Fluid Mech*, 14:136, 1962.

[106] X. Shao, Z. Yu, and B. Sun. Inertial migration of spherical particles in circular poiseuille flow at moderately high reynolds numbers. *Phys. Fluids*, 20:103307, 2008.

[107] F. Snijkers, G. D'Avino, P. L. Maffetone, F. Greco, M. Hulsen, and J. Vermant. Rotation of a sphere in a viscoelastic liquid subjected to shear flow. Part II. Experimental results. *J. Rheol.*, 53:459–480, 2009.

[108] J. Sprakel, J. T. Padding, and W. J. Briels. Transient forces and non-equilibrium states in sheared polymer networks. *Europhys. Lett.*, 93:58003, 2011.

[109] J. Sprakel, E. Spruijt, J. van der Gucht, J. T. Padding, and W. J. Briels. Failure-mode transition in transient polymer networks with particle-based simulations. *Soft Matter*, 5:4748–4756, 2009.

[110] S. Succi. *The Lattice Boltzmann equation for fluid dynamics and beyond*. Oxford University Press, USA, 2001.

[111] B. Sun, Z. S. Yu, and X. M. Shao. Inertial migration of a circular particle in nonoscillatory and oscillatory pressure-driven flows at moderately high reynolds numbers. *Fluid Dyn. Res.*, 41:055501, 2009.

[112] M. A. Tehrani. An experimental study of particle migration in pipe flow of viscoelastic fluids. *J. Rheol.*, 40:1057, 1996.

[113] S. Y. Trofimov, E. L. F. Nies, and M. A. J. Michels. Dissipative particle dynamics for interacting systems. *J. Chem. Phys.*, 117:9383, 2002.

[114] R. Tuinier, G. A. Vliegenthart, and H. N. W. Lekkerkerker. Depletion interaction between spheres immersed in a solution of ideal polymer chains. *J. Chem. Phys.*, 113:10768, 2000.

[115] A. van den Noort and W. J. Briels. Coarse-grained simulations of elongational viscosities, superposition rheology and shear banding in model core-shell systems. *Macromol. Theory Simul.*, 16:742–754, 2007.

[116] A. van den Noort and W. J. Briels. Brownian dynamics simulations of concentration coupled shear banding. *J. Non-Newtonian Fluid Mech.*, 152:148–155, 2008.

[117] A. van den Noort, W. K. den Otter, and W. J. Briels. Coarse graining of slow variables in dynamic simulations of soft matter. *Europhys. Lett.*, 80:28003, 2007.

[118] J. Vermant, 2011. private communication.

[119] J. Vermant and M. J. Solomon. Flow-induced structure in colloidal suspensions. *J. Phys.: Condens. Matter*, 17:R187–R216, 2005.

[120] L. M. Walker. Rheology and structure of worm-like micelles. *Curr. Opin. Colloid Interface Sci.*, 6:451–456, 2001.

[121] G. M. Whitesides and Grzybowski. Self-assembly at all scales. *Science*, 295:2418, 2002.

[122] D. Won and C. Kim. Alignment and aggregation of spherical particles in viscoelastic fluid under shear flow. *J. Non-Newtonian Fluid Mech.*, 117:141–146, 2004.

[123] J. M. Yeomans. Mesoscopic simulations: Lattice boltzmann and particle algorithms. *Physica A*, 369:159, 2006.

[124] Y. Yin, Y. Lu, B. Gates, and Y. Xia. Template-assisted self-assembly: A practical route to complex aggregates of monodispersed colloids with well-defined sizes, shapes, and structures. *J. Am. Chem. Soc.*, 123:8718–8729, 2001.

[125] Z. Yu, A. Wachs, and Y. Peysson. Numerical simulation of particle sedimentation in shear-thinning fluids with a fictitious domain method. *J. Non-Newtonian Fluid Mech.*, 136:126–139, 2006.